OFFSHORE WIND TURBINES IN THE NATURAL ENVIRONMENT:

STATISTICAL PREDICTION OF POWER AND FATIGUE

A Dissertation

by

SHU DAI

Submitted to the Office of Graduate and Professional Studies of
Texas A&M University
in partial fulfillment of the requirements for the degree of

DOCTOR OF PHILOSOPHY

Chair of Committee,	Bert Sweetman
Committee Members,	Jens Figlus
	Robert Randall
	Michael Pilant
Head of Department,	Sharath Girimaji

December 2020

Major Subject: Ocean Engineering

ABSTRACT

The purpose of this research is to understand the statistical characters of natural wind and further apply this statistical model to improve the power forecast and blade fatigue estimation for Floating Offshore Wind Turbines (FOWTs).

A new methodology is developed for recalibration of cup anemometers and demonstrated by computation of higher order statistics of coastal sea breezes. The development is based on representing the dynamic response of a cup rotor by an equation of motion (EOM) relating rotational motion of the cup rotor to aerodynamic forcing. The overall methodology is then applied to recover the time history and mean of the true wind speed from field-measured cup data. A practical application of the method is demonstrated by recalibrating a larger set of cup data measured during a 2-month field campaign on the Texas coast to assess the higher statistical moments of the wind process. Measured coastal sea breezes in this area are found to be non-Gaussian.

With the deeper understanding of wind process, a new methodology is derived to transform between an ideal zero-turbulence power curve and practical power curves representing wind turbine performance in irregular winds. The derivation is based on substituting a theoretical distribution of the wind process in place of a single mean wind speed in the power computation, and then applying random process theory to derive analytical expressions for the expected power and standard deviation of power. The resulting expressions explicitly include the effects of varying turbulence intensity and higher statistical moments, and enable the performance of an operating

wind turbine to be parameterized using a limited number of coefficients. The accuracy of the new method is demonstrated by benchmarking expected power and standard deviation of power against direct simulation in irregular winds, including winds with various turbulence intensities and non-Gaussian statistics.

The non-Gaussian wind model is used to estimate the fatigue damage of composite wind turbine blades and the impact of non-Gaussian winds on fatigue life is also discussed. The Weibull distribution, widely acknowledged to fit the long-term wind speeds, is applied on local buoy data to calculate the probability density function (PDF) of local winds. Numerical simulations based on OC3-Hywind model with local winds PDF are used to identify the fatigue hot-spot on the blades. Blade fatigue life based on hot-spot are calculated using Gaussian random wind conditions which are simulated through the entire operation wind speed range. Corresponding non-Gaussian random wind conditions using field measured data are simulated as well. The impact of non-Gaussian wind on blade fatigue is analyzed based on the comparison of these results.

ACKNOWLEDGEMENTS

This dissertation is composed of the major results of my research as a doctoral student enrolled in Texas A&M University. I would like to express my sincere gratitude to my advisor, Professor Bert Sweetman, for his insightful guidance and consistent encouragement along the way. This dissertation and other journal paper manuscripts are impossible to be finished without his kindly support. I greatly appreciate Professor Jens Figlus, Professor Robert Randall and Professor Michael Pilant for their review and comments for my research topics and serving as committee members

I would like to thank my classmates, Yanbin Bai, Hao Wang, Yuanzhe Zhi, and Han Huang who attend Texas A&M University together with me for their continuous support. I would also thank my friends in both College Station and Galveston, Fan Xia, Haifeng Yang, Fangyuan Qu, Yan Zhao, Xiao Yu, Ju Gao, Dapeng Li, Shanran Tang, Jiangnan Lu for their help on my study and research.

Lastly, and most importantly, I would like to thank my parents Dr. Jinfu Dai and Ping Wu for their continuous support and trust.

CONTRIBUTORS AND FUNDING SOURCES

Contributors

This work was supervised by a dissertation committee consisting of Professor Bert Sweetman, Professor Jens Figlus and Professor Robert Randall of the Department of Ocean Engineering and Professor Michael Pilant of the Department of Mathematica.

The weather station used for the field wind measurement campaigns of Chapter 2 is offered by Professor Jens Figlus. Texas A&M University Galveston campus arranged the observation site for the experiment.

All other work conducted for the dissertation is completed by the student independently.

Funding Sources

This research has been partially funded by the National Science Foundation, Energy for Sustainability, within the Division of Chemical, Bioengineering, Environmental and Transport Systems, agreement number CBET-1133682 (Dr. Sweetman, Principle Investigator).

This research has been partially funded by the Texas Institute of Oceanography, with TIO summer research fellowship.

NOMENCLATURE

AEP	Annual Energy Production
DLC	Design Load Case
DOF	Degree of Freedom
EOM	Equation of Motion
FAST	Fatigue, Aerodynamics, Structures, and Turbulence
FOWT	Floating Offshore Wind Turbine
EWEA	European Wind Energy Association
JONSWAP	Joint North Sea Wave Project
NOAA	National Oceanic and Atmospheric Administration
NREL	National Renewable Energy Laboratory
STD	Standard Deviation

TABLE OF CONTENTS

Page

Page

LIST OF FIGURES

FIGURE Page

LIST OF TABLES

TABLE Page

1. INTRODUCTION

1.1 Background

Wind-energy is increasingly accepted as an economically viable and environmentally friendly method of energy harvest. Local permitting and environmental issues associated with considerations such as noise emissions and interruption of the view-scape are becoming critical problems as desirable space for on-shore wind turbines becomes increasingly scarce.

European countries, which are relatively densely populated compared with the United States, began siting offshore wind turbines in shallow waters near shore, most notably in Denmark and Germany in the 1990's. The growth of offshore wind energy in European countries is significant, with projected growth rates of 1700 to 3000 MW per year (Snyder and Kaiser, 2009). China, in the far east is beginning installation of offshore wind farms, including the first offshore wind farm in East China Sea, which will produce 267 GWh per year for the energy market in Shanghai (Chen, 2011).

The bottom-founded support towers may prove cost-prohibitive in very deep waters, but the cost of floating offshore systems is relatively insensitive to water depth and may prove to offer a viable way to develop wind energy beyond the sight of land. The floating offshore wind turbines are becoming a popular option for offshore wind industry. Hywind Scotland, the world's first commercial floating wind farm in Unite Kingdom, including six spar type floating wind turbines

had been successfully installed in 2017. The turbines integrated a 6 MW Nacelle on a 83 meter height tower, supported by a spar cylinder with around 78 meter draft.

This project is focused on energy forecasting and fatigue assessment of wind farms using spar-type floaters, including floaters that offer less vertical stiffness than typical for the industry. These highly compliant structures are less expensive and may offer other operational benefits, but also have complicated nonlinear system dynamics that are difficult to simulate numerically. An in-house software package is available to simulate highly compliant floating support structures with large angular displacements in deep water ("Loose", Wang and Sweetman, 2011).

1.2 Research Hypothesis

This research is driven by two major hypotheses. The first hypothesis is that random process theory could be used to replace the time domain analysis of structure dynamics. The new method with random theory could be applied to predict the performance of FOWTs and estimate the AEP. The second hypothesis is that the non-linear dynamic system of structure could be correctly represented by external force caused by non-Gaussian wind process.

The time domain analysis of structure dynamics is replaced by new method of random process theory with same accuracy and significant less computer time. Non-Gaussian wind process transferred by Hermit moment transformation are used for the numerical simulation of non-linear dynamic system of structure, and proved to be significant different with Gaussian wind process.

Additionally, non-Gaussian natural wind process is verified through field measurements via calibrated cup anemometer.

1.3 Research Objective

The research objective of this dissertation is to assess the impact of higher statistical moments of natural wind processes on offshore wind turbines, including the energy production and blade fatigue.

Important steps to reach this research objective include:

1. Conducting two field wind speed measurement campaigns using cup anemometers at two coastal locations in Texas.
2. Development of a new recalibration method to recover the time history of the true wind speed from data captured by a cup anemometer; this development is based on the dynamic equation of motion (EOM) of the rotor.
3. Development of a new recalibration method to recover the mean of the true wind speed from the mean wind speed reported by a cup anemometer; this development is based on random process theory.
4. Determining the higher statistical moments of stationary segments of the measured wind speed for use in design of coastal structures.
5. Derivation of a power curve transformation methodology to predict the mean and standard deviation of power harvested by a floating offshore wind turbine (FOWT) from the first four

statistical moments of the wind process; this development is based on applying a Taylor series expansion to derive statistical expressions for the mean and variance of the power.

6. Development of a methodology to generate non-Gaussian wind field time-histories from Gaussian wind-fields predicted by existing simulation tools.
7. Evaluation of the impact of Non-Gaussian winds on blade fatigue using direct simulation including non-Gaussian wind effects.
8. Quantify the statistical differences between land and sea breezes.

1.4 Literature Review

1.4.1 Power Curve and AEP Estimation

The International Electrotechnical Commission (IEC) (IEC, 2005) recommends computing annual energy production using a practical power curve measured from an operating wind turbine. A practical power curve is generally constructed from measured 10-minute means of power and wind speed, such that the resulting curve implicitly includes all effects of irregularities in the wind as well as the turbine control-system dynamic response.

Practical power curves can be significantly different from ideal turbulence-free power curves and can be useful in project planning and design, but these curves cannot be accurately constructed from field measurements prior to siting a wind turbine in the actual wind conditions for the proposed location. The importance of practical power curves is heightened because the practical curve always predicts less power than the ideal curve, and the largest differences are near the rated

speed of the turbine. These differences result mainly from the system being unable to shift instantaneously between control strategies when subject to short-term variations in the wind speed.

researchers have applied statistical methods to develop estimate power generation. Carrillo, et al. (2013) shows that the cubic and exponential functions are each an excellent fit for the torque-controlled region of practical power curves for commercial FOWTs. Shokrzadeh et al (2014) introduce a locally weighted polynomial regression method to define a power curve using both simulated datasets and measured data from a wind farm. Advanced statistical methods have also been investigated as an alternative to power curves.

Multiple researchers, (e.g., Li et al., 2001, Mabel and Fernandez, 2008 and Kusiak, et al., 2009) each develop and verify the effectiveness of artificial neural network models using field-data measured on various wind farms. Kusiak goes on to suggest his model could also be applied to wind farm management, individual turbine control and energy generation optimization.

Long-term wind speed data represents the local wind energy protentional. Shu and Chan (2014) analyze 6-year wind data recorded at five meteorological stations, each with a different ground terrain in Hong Kong. They present a statistical analysis of the wind characteristics and wind energy potential using Weibull distribution. Feng and Shen (2015) propose a method to construct joint distributions of wind speed and wind direction via parameters of direction wise Weibull distributions using interpolations between sectors. The best fit of joint distributions is used to optimize the layout of a wind farm. Another interesting approach of long-term prediction is finding a power curve fitting the actually performance of offshore wind turbine. Zhang, et al. (2014)

develop a local outlier factor (LOF) algorithm applying on active power and wind speed time history to achieve actuate power curve.

1.4.2 Natural Wind Process and Field Measurement

High turbulence flow causes difficulty in short-term wind speed measurement in the field. Cup anemometers are used almost universally in long-term deployments because they have been proven to be robust against the natural environment. They are also low maintenance, require low power to operate, and are relatively inexpensive. The Unites States National Oceanic and Atmospheric Administration (NOAA) manages 1,300 meteorological-oceanographic buoys worldwide, each of which measures winds using a cup anemometer.

Accurate quantification of wind speeds is important for planning and design of many civil structures. Maximum loading on structures requires quantification of the extreme fractiles of the wind process in storm conditions, which can be meaningfully different depending on the higher order statistics of the wind. Planning new wind farms requires quantification of typical wind conditions at the proposed site for safety and economy reasons. The International Electrotechnical Commission (IEC, 2006) gives guidance for wind velocity and standard deviation of velocity for both onshore and offshore locations, but does not explicitly address coastal conditions.

Various researchers have compared wind measurement from cup anemometers versus hotwire anemometers and found that wind speeds observed by hot wire anemometers show greater variability than winds observed by cup anemometers (e.g., Kaganov and Yaglom, 1975).

Measurement differences may be caused by differing operational mechanics of the two devices. Pedersen (2004) does extensive field testing of numerous cup anemometers; he observes some anemometers generally overpredict, while others underpredict.

Several other observers have found specific cup anemometers to consistently underpredict the true speed (e.g., Kristensen, 2002, Ziter, 2010), while others have found specific cup anemometers to overpredict (e.g., Busch & Kristensen, 1976, Wieringa, 1980, Hölling, et al., 2007). MacCready (1966) describes the main sources of cup measurement errors as being due to vertical components in the wind, data post-processing (mismatching mean wind speed and mean wind direction), and dynamic response of the cup. Another source of error is wind turbulence. Kondo, et al. (1971) observes measurement errors are caused by the inertial mass of the rotor, with overestimation by 0.4-1% for sea breeze and 4-7% for daytime land breezes. His field data suggests there are larger errors in higher turbulence conditions.

Cup anemometers are calibrated in ideal steady wind conditions. Natural variations in wind speed impose nonlinear aerodynamics forces on the anemometer cups, and also require the rotor to accelerate. Numerous investigators attempt to find theoretical representations of the complicated EOM of the cup rotor. Brevoort and Joyner (1934) do extensive wind tunnel testing to find coefficients of lift and drag for anemometer cups. Ramachandran (1969) develops an equation of motion (EOM) for the rotor, and presents a numerical simulation of the anemometer in different wind conditions. Zhou (2007) performs wind tunnel tests to successfully verify the model developed by Ramachandran. Fortin, et al. (2005) quantifies the importance of rotor dynamics, observing that cup speed is decreased 10 -- 30% due increased mass caused by icing.

1.4.3 Blade Fatigue Analysis and Non-Gaussian Impact

Floating offshore wind turbines (FOWT), which are deployed in the nature ocean environment, are working under huge number of cyclic external loads. A typical wind turbine, during its 20 years life time, may experience more than 10^8 cycles loads with an approximately 30 rpm rotation speed and 4000 hours operation time per year (Manwell, et al., 2010). It is great challenge to predict the fatigue life of a wind turbine blade because other manufactured equipment is unlikely to experience more than 10^6 cycles over their lifetime.

Rapid prediction of expected energy harvest would be useful in comparing alternatives in the process of planning offshore wind farms. Design alternatives could include competing locations, turbine size, and vendor products. Wind energy forecasting is an important part of computing overall project economics; project economics are even more important for offshore developments. Capital expenditures for offshore wind developments are typically one and a half to two times more than for onshore developments (Watson, et al., 2005), and maintenance costs are likely to be 5–10 times higher than onshore (Van Bussel, & Zaaijer, 2001, March).

Fatigue damage of FOWTs is the process in which an accumulation of damages is caused by a repeating environmental load of variable magnitude applied on their structures. Once sufficient damage is accumulated, fatigue fracture will initiate and propagate through the plasticized regions. Fatigue damage calculations and fatigue life predictions of offshore wind turbines are quite complicated.

Fatigue life of a medium scale horizontal axis wind turbine system was estimated by using the well-known S–N damage equation with load spectrum confirmed with at least 20-30 years' operating life (Kong, et al, 2006). Reliability-based calibration of a design code for wind-turbine rotor blades is developed considering the fatigue failure in flapwise bending (Ronold, et al, 2001). Hu use 10-min mean wind speed and 10-min turbulence intensity based on long-term wind speed distribution to simulate the random wind field and analyze the fatigue reliability of a composite wind turbine blades considering wind load uncertainty (Hu, et al., 2012). A stochastic approach is employed to develop a computer code in order to simulate wind flow with randomness in its nature on the blade and subsequently each load case is weighted by its rate of occurrence using a Weibull wind speed distribution (Shokrieh and Rafiee, 2006).

Several researches apply widely used statistical distribution models, such as Weibull and Rayleigh distribution, to describe the annual wind speed data. A research based on 6-year wind data recorded at five meteorological stations use Weibull distribution model to analyze the statistical characteristics of wind in Hong Kong (Shu, et al., 2014). Shuang and Song choose Rayleigh distribution to identify the probability density function of long-term wind speed data, and then determine the long-term extreme response distribution by integrating the short-term extreme response distribution of each mean wind speed bar (Shuang and Song, 2017).

Wind time-histories are commonly simulated from wind power spectra using techniques that conform to the central limit theorem such that the simulated wind speeds conform to a Gaussian distribution. Unfortunately, the analyze of field measurement data of wind speed find different

conclusion that natural short-term wind is not Gaussian distribution (Dai and Sweetman, 2019). Non-Gaussian wind inflow velocities to offshore wind turbines could potentially affect the predicted power, load, torque, and blade fatigue life. Some experimental and numerical work has been done to assess the effects of extreme events in atmospheric wind fields (Mücke, et al., 2011). This increased quantity of extreme events will cause alternating loads on the airfoil and on the main shaft in the form of torque fluctuations, which may cause additional fatigue damage.

Schottler and Reinke (2017) make an experimental approach by simulating non-Gaussian and Gaussian wind inflow conditions on a wind turbine model in a wind tunnel. They then analyze the power and torque data recorded by the wind turbine model. Berg and Natarajan (2016) simulate two types of wind speed time series in 3D space on offshore wind turbine via the HAWC2 software package.

Schottler and Reinke (2017) develop an experimental approach which simulate non-Gaussian and Gaussian wind inflow conditions to a wind turbine model in a wind tunnel. Power and torque results indicate that extreme loads in non-Gaussian wind inflow conditions occur much more frequently than predicted by a typical Gaussian wind model. Gong and Chen (2017) investigate the extreme response of operational and parked wind turbines in non-Gaussian wind conditions. Obviously larger extremes response of blade root edgewise and tower base fore-aft bending moments are found for operational wind turbine in the non-Gaussian wind inflows. Similar results of blade root flap wise bending moment are found for parked wind turbine.

2. A METHODOLOGY TO RECALIBRATE CUP ANEMOMETERS WITH APPLICATION TO STATISTICAL ANALYSIS OF SEA BREEZES

2.1 Introduction

Cup anemometers are used almost universally in long-term deployments because they have been proven to be robust against the natural environment. They are also low maintenance, require low power to operate, and are relatively inexpensive. The Unites States National Oceanic and Atmospheric Administration (NOAA) manages 1,300 meteorological-oceanographic buoys worldwide, each of which measures winds using a cup anemometer.

Accurate quantification of wind speeds is important for planning and design of many civil structures. Maximum loading on structures requires quantification of the extreme fractiles of the wind process in storm conditions, which can be meaningfully different depending on the higher order statistics of the wind. Planning new wind farms requires quantification of typical wind conditions at the proposed site for safety and economy reasons. The International Electrotechnical Commission (IEC, 2006) gives guidance for wind velocity and standard deviation of velocity for both onshore and offshore locations, but does not explicitly address coastal conditions.

Various researchers have compared wind measurement from cup anemometers versus hotwire anemometers and found that wind speeds observed by hot wire anemometers show greater variability than winds observed by cup anemometers (e.g., Kaganov and Yaglom, 1975). Figure 2.1 shows typical results of a side-by-side deployment of hot-wire and cup anemometers at a

coastal Texas location in March of 2018. Comparison of the two time-histories shows that the cup anemometer used for this field campaign underpredicts both the peak wind speed and mean wind speed compared with the hot wire. The hot wire data also appears unsymmetrical about its mean, suggesting the true wind speed may be a non-Gaussian process. The difference between the mean and variance of cup versus hot wire data typically increases with increasing wind speed and turbulence, as shown in Figures 2.1 (a) and (b).

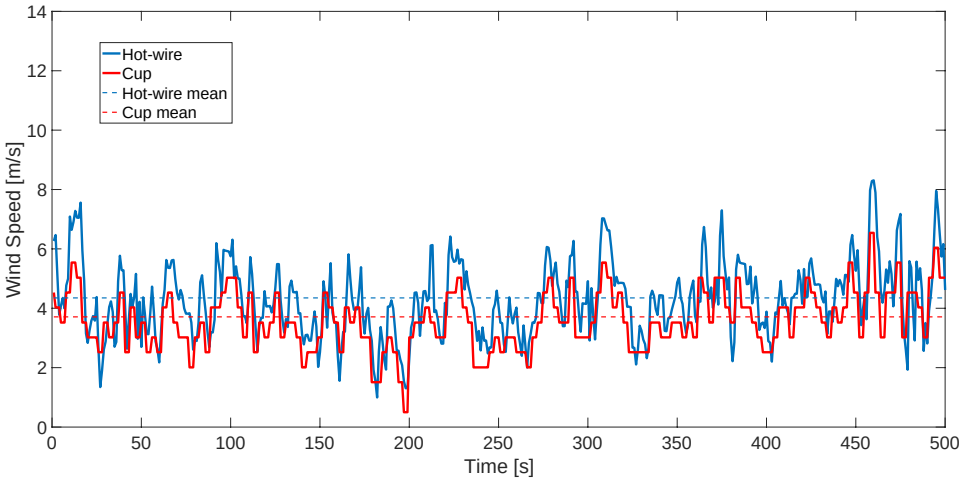

(a) Low wind speed range (Sample 5)

Figure 2.1: Wind speed measured by hot-wire and cup anemometers

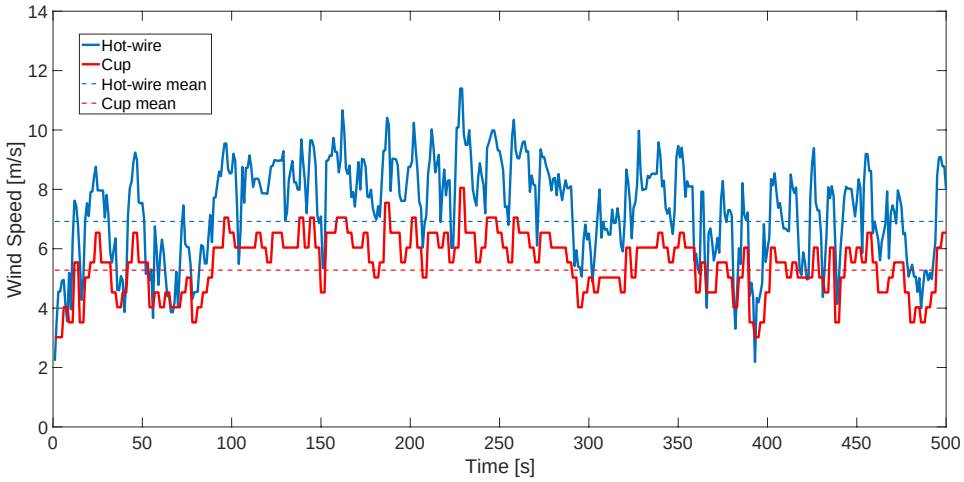

(b) High wind speed range (Sample 10)

Figure 2.1 continued.

Measurement differences may be caused by differing operational mechanics of the two devices. Pedersen (Pedersen, 2004) does extensive field testing of numerous cup anemometers; he observes some anemometers generally overpredict, while others underpredict. Several other observers have found specific cup anemometers to consistently underpredict the true speed (e.g., Kristensen, 2002, Ziter, 2010), while others have found specific cup anemometers to overpredict (e.g., Busch & Kristensen, 1976, Wieringa, 1980, Hölling, et al., 2007). MacCready (MacCready, 1966) describes the main sources of cup measurement errors as being due to vertical components in the wind, data post-processing (mismatching mean wind speed and mean wind direction), and dynamic response of the cup. Another source of error is wind turbulence. Kondo (Kondo, et al., 1971) observes measurement errors are caused by the inertial mass of the rotor, with overestimation by 0.4-1% for sea breeze and 4-7% for daytime land breezes. His field data suggests there are larger errors in higher turbulence conditions.

Cup anemometers are calibrated in ideal steady wind conditions. Natural variations in wind speed impose nonlinear aerodynamics forces on the anemometer cups, and also require the rotor to accelerate. Numerous investigators attempt to find theoretical representations of the complicated EOM of the cup rotor. Brevoort (Brevoort and Joyner, 1934) do extensive wind tunnel testing to find coefficients of lift and drag for anemometer cups. Ramachandran (Ramachandran, 1969) develops an equation of motion (EOM) for the rotor, and presents a numerical simulation of the anemometer in different wind conditions. Zhou (Zhou, 2007) performs wind tunnel tests to successfully verify the model developed by Ramachandran. Fortin (Fortin, et al., 2005) quantifies the importance of rotor dynamics, observing that cup speed is decreased 10 -- 30% due increased mass caused by icing.

Prior work on recalibration of cup anemometers has focused on theoretical developments related to the aerodynamic forcing on the rotor. The work presented here builds on that prior theoretical work in that it begins with a dynamic equation of motion, but differs in that a computer-based central difference method is employed to directly extract the aerodynamic and mechanical characteristics of the cup anemometer from side by side measurements from a cup and hotwire. Second-order regression is shown to be an effective way to estimate the unknown coefficients in the EOM from these side-by-side measurements. The resulting calibrated EOM represents a single cup-anemometer type, which can subsequently be used to reconstruct a complete time history of the true wind from the wind as estimated by a cup anemometer. A methodology is also developed from random process theory by which the calibrated EOM can be used to directly estimate the true mean wind speed from the mean observed using the cup.

Section 2 gives the theoretical derivation of the dynamic EOM of a cup anemometer and associated coefficients. Section 3 gives a detailed example: laboratory measurements and measurements form a field data campaign are used to determine the unknown coefficients in the EOM; the resulting EOM is then applied to recalibrate data from a second field campaign, and the resulting time-history is used to compute the statistical moments of the wind.

2.2 Theory

2.2.1 Dynamic Response of Cup Anemometer

The dynamic response of a cup anemometer can be treated as a spring-mass-damper system with zero stiffness.

$$I\frac{d\omega}{dt} + C\omega = M(t) \tag{2.1}$$

where I is the moment of inertia of the cup anemometer, ω and $d\omega/dt$ are the rotational speed and acceleration, C is the damping coefficient, and $M(t)$ is the total moment applied about the spin axis.

Various researchers have investigated computation of the applied rotation moment. Ramachandran (Ramachandran, 1966) summarizes work by Brevoort (Brevoort and Joyner, 1934) and Corcoran (Corcoran and Esau, 1964). He gives expressions for applied rotational moment $M(t)$ which include two terms: $c_d v^2$ and $c_1 v\omega$, explicitly showing the importance of both wind speed v and

rotational speed ω. Ramachandran (Ramachandran, 1969), suggests an EOM of a cup anemometer and supplies constant values $of\ c_0, \tau, c_d$ representing a specific anemometer type;

$$I\frac{d\omega}{dt} + (c_0 + c_1 v)\omega = c_d v^2 - \tau \tag{2.2}$$

in which I is the mass moment of inertia of the rotor plus entrained wind, $(c_0 + c_1 v)$ is the rotational resistance, and $(c_d v^2 - \tau)$ is the applied torque. Parameters c_0 and c_1 represent rotational resistance and cup aerodynamic friction, respectively; parameter c_d calibrates aerodynamic moments and τ represents device rotational friction. The EOM of the rotor can be simplified for steady winds setting rotational acceleration $d\omega/dt$ = 0 and reorganizing:

$$\omega = \frac{c_d v^2 - \tau}{c_0 + c_1 v} = \frac{c_d}{c_0/v + c_1} v - \frac{\tau}{c_0 + c_1 v} \tag{2.3}$$

This expression for rotational speed can be further simplified by neglecting rotational resistance terms τ and c_0. Substituting $k = c_d/c_1$, $b = \tau/c_0$ into Equation 2.3:

$$\omega = k v_c - b \tag{2.4}$$

In which k and b are recalibration constants relating a steady wind speed to a constant cup rotation speed.

The inertial term in Equation 2.2 remains important in unsteady winds. Collecting all unknown quantities in Equation 2.2 into two terms: inertial parameter $\widetilde{I} = \frac{I}{c_d}$ and resistance parameter $\widetilde{C} = \frac{c_0 + c_1 v + \tau/\omega}{c_d}$:

$$\widetilde{I}\,\frac{d\omega}{dt} + \widetilde{C}\,\omega = v^2 \tag{2.5}$$

in which $\widetilde{I}$ and $\widetilde{C}$ are parameters relating the speed of the true wind speed to the rotational speed and acceleration of the cup rotor.

2.2.2 Numerical Approach of the Dynamic Solution

Parameters $\widetilde{I}$ and $\widetilde{C}$ can be estimated for any cup anemometer design by combining a time history of the true wind speed with that of the wind speed predicted by the cup anemometer. A discrete numerical representation of Equation 2.5 can be developed using the central difference method (CDM).

$$\widetilde{I}_i\,\frac{\omega_{i+1} - \omega_{i-1}}{2\Delta t} + \widetilde{C}_i\omega_i = v_i^2 \tag{2.6}$$

in which the differential slope $d\omega_i/dt$ can be reasonably replaced by the finite slope $(\omega_{i+1} - \omega_{i-1})/2\Delta t$ for small Δt (Figure 2.2).

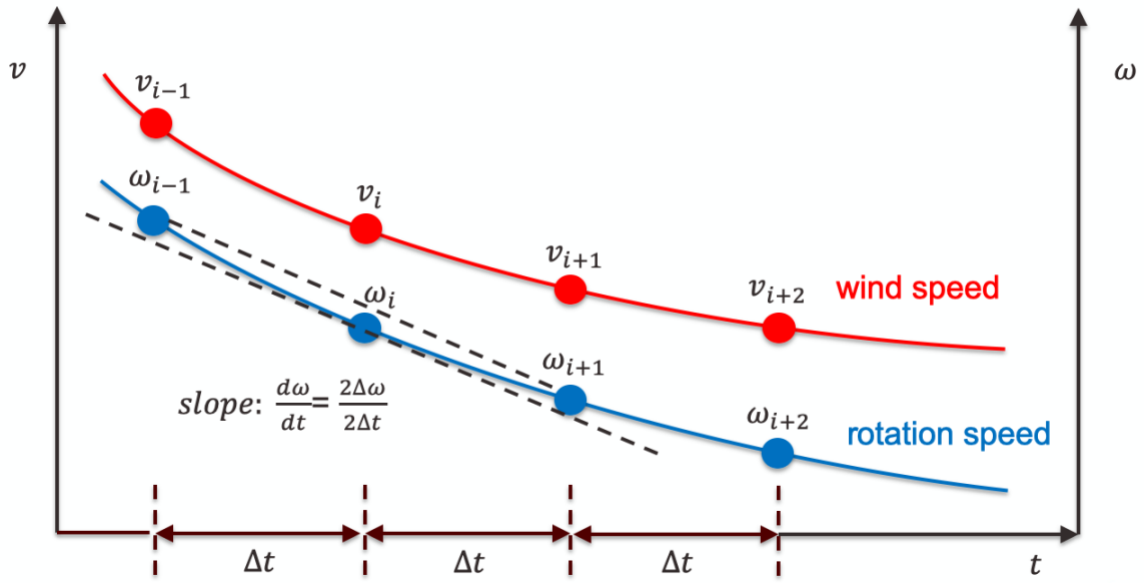

Figure 2.2: CDM applied to EOM of cup anemometer

Applying Equation 2.6 simultaneously at v_i and v_{i+1}, and assuming $\widetilde{C}_i = \widetilde{C}_{i+1}$ and $\widetilde{I}_i = \widetilde{I}_{i+1}$ yields a system of two equations in $\widetilde{C}_i$ and $\widetilde{I}_i$ the solution of which is:

$$\begin{cases} \widetilde{I}_i = \left(\frac{v_{i+1}^2}{\omega_{i+1}} - \frac{v_i^2}{\omega_i}\right) / \left(\frac{\omega_{i+2} - \omega_i}{2\Delta t \omega_{i+1}} - \frac{\omega_{i+1} - \omega_{i-1}}{2\Delta t \omega_i}\right) \\ \widetilde{C}_i = \left(\frac{2\Delta t\, v_{i+1}^2}{\omega_{i+2} - \omega_i} - \frac{2\Delta t\, v_i^2}{\omega_{i+1} - \omega_{i-1}}\right) / \left(\frac{2\Delta t\, \omega_{i+1}}{\omega_{i+2} - \omega_i} - \frac{2\Delta t\, \omega_i}{\omega_{i+1} - \omega_{i-1}}\right) \end{cases} \quad (2.7)$$

Equations 2.7 can be applied sequentially at every time step to develop a time-history of inertia and resistance parameters $\widetilde{I}_i$ and $\widetilde{C}_i$.

Aerodynamic damping is commonly assumed to be quadratic (e.g., Kareem, et al., 1998). Here the resistance parameter $\widetilde{C} = \frac{c_0 + c_1 v + \tau/\omega}{c_d}$ is assumed to be a quadratic function of wind speed:

$$\widetilde{C} = r_1 v^2 + r_2 v + r_3 \tag{2.8}$$

in which coefficients r_1, r_2 and r_3 can be estimated by fitting a polynomial through the cloud of $\widetilde{C_i}$'s resulting from repeated applications of Equation 2.7 to a pair of contemporaneous time histories. The validity of using a least-squares polynomial fit is examined as part of Example 3.2.1. Substituting Equation 2.8 into Equation 2.6 yields an expression relating the true wind speed to the rotational speed of the cup anemometer:

$$(1 - r_1\omega_i)v_i^2 - r_2\omega_i v_i - r_3\omega_i - \widetilde{I}_i\,(\omega_i - \omega_{i-1})/dt = 0 \tag{2.9}$$

The root of this quadratic equation can be directly applied to recover a time history of the true wind speed:

$$v_i = \frac{r_2\omega_i + \sqrt{{r_2}^2\omega_i^2 + 4(1 - r_1\omega_i)\left[r_3\omega_i + \widetilde{I}_i\,(\omega_i - \omega_{i-1})/dt\right]}}{2 - 2r_1\omega_i} \tag{2.10}$$

in which ω_i can be estimated from high-frequency wind time-history measured using a cup anemometer using Equation 2.4, $\omega_i = kv_{ci} - b$.

2.2.3 Recalibration of Mean Wind Speed

Meteorological data is commonly provided as a mean wind speed, without providing a high-frequency time history. Random process theory can be applied to develop a direct relationship

between the true mean wind speed and the wind speed estimated by a cup anemometer. The wind speed, rotational speed, and rotational acceleration can be represented by random variables, V, Ω, and $\dot{\Omega}$, respectively, as can be parameters $\widetilde{I}$ and $\widetilde{C}$. The complete wind and rotation temporal processes related by Equation 2.5 can be represented as a function of random variables:

$$\widetilde{I}\,\dot{\Omega} + \widetilde{C}\,\Omega = V^2 \tag{2.11}$$

The mean of the rotational acceleration can be found by taking the expectation of every term and further assuming that random variable $\widetilde{I}$ is independent of V^2 and that $\widetilde{C}$, $\tilde{I}$ and Ω are independent within any statistically stationary time segment, such that expected values of products and quotients equal equivalent functions of expected values:

$$E(\dot{\Omega}) = \frac{1}{E(\widetilde{I})}E(V^2) - \frac{E(\widetilde{C})}{E(\widetilde{I})}E(\Omega) \tag{2.12}$$

in which the mean of the rotational acceleration $E(\dot{\Omega})$ is zero for a stationary process. The definition of the variance can be used to substitute for the unknown $E(V^2)$:

$$[E(V)]^2 + Var(V) - E(\widetilde{C})E(\Omega) = 0 \tag{2.13}$$

where $\widetilde{C}^{\,*} = E(\widetilde{C})$ is the expected value of $\widetilde{C}$ for a stationary segment of the process, to which the definition of the variance can also be applied:

$$\widetilde{C}^{*} = r_1(\mu^2 + \sigma^2) + r_2\mu + r_3 \tag{2.14}$$

Reformatting Equation 2.13 into common statistical parameters by performing a series of substitutions: $\mu = EV$, $\sigma^2 = Var(V)$, and $\mu_\omega = E[\omega] \cong E[\Omega]$, then substituting $\mu_\omega = k\mu_c - b$ (from Equation 2.4):

$$(\mu^2 + \sigma^2) - \widetilde{C}^{*}(k\mu_c - b) = 0 \tag{2.15}$$

which can be solved for an analytical expression for the true mean wind speed:

$$\mu = \sqrt{\widetilde{C}^{*}(k\mu_c - b) - \sigma^2} \tag{2.16}$$

Where σ is the standard deviation of the true wind speed. Application of Equation 2.16 requires coefficients k and b, which can be identified using a constant speed wind tunnel test, and average resistance coefficient $\widetilde{C}^{*}$, which can be determined using Equation 2.14 if point-by-point time-histories are available, or by Equation 2.16 if only mean and variance data are available.

2.3 Example

An example is presented in which the numerical model of a cup anemometer is recalibrated and applied to a field data campaign. The device first is subject to steady wind flow in the lab to determine coefficients *k* and *b*. The device is then subject to natural winds on a rooftop, side-by-

side with a hotwire anemometer to determine inertia parameter $\widetilde{I}$ and resistance parameter $\widetilde{C}$ or $\widetilde{C}^*$. The final part of the example to application of the calibrated model to wind speed data captured by the cup anemometer during a long-term field campaign. The flow of the entire example is shown in Figure 2.3.

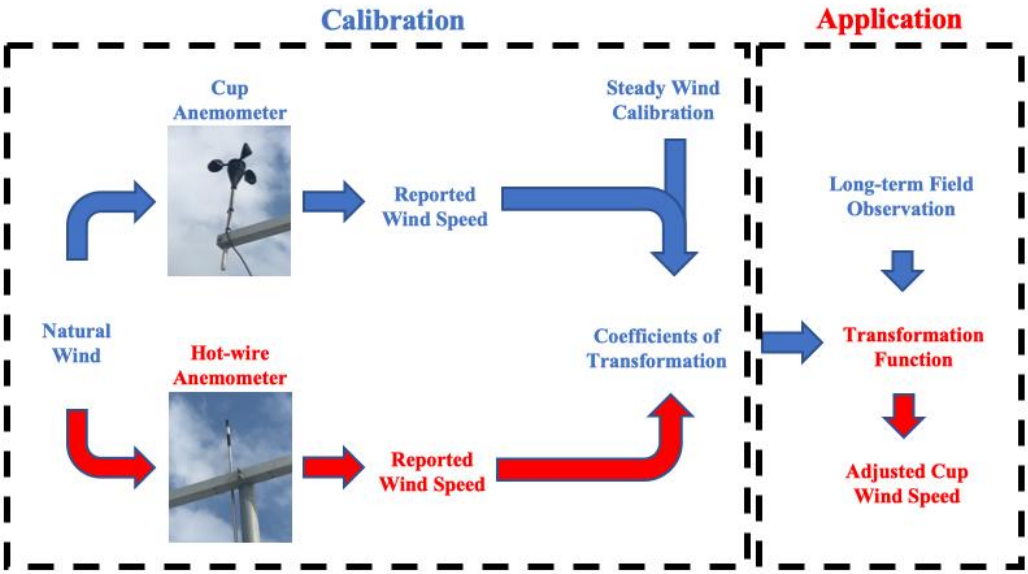

Figure 2.3: Flowchart of numerical recalibration method

2.3.1 Calibration of HOBO U30 Cup Anemometer

2.3.1.1 Lab Calibration in Steady Winds

A commercially packaged wind anemometer kit is used throughout this example, the Onset HOBO U30. This weather station kit includes a cup wind speed anemometer, a wind direction anemometer, and a compact data logger. Technical specifications are shown in Table 2.1.

General features	Specifications
Measurement range	0–76 m/s
Accuracy	± 1.1 m/s
Resolution	0.5 m/s
Dimensions	41 × 16 cm
Weight	300 g

Table 2.1: Technical specifications of wind speed sensor

Coefficients *k* and *b* of the cup anemometer were determined experimentally in the laboratory. Wind was mechanically driven at each of five different constant wind speeds. The rotor was optically recorded at 60 frames per second, from which rotational velocity was digitized by measured change in angle per time step (Figure 2.4).

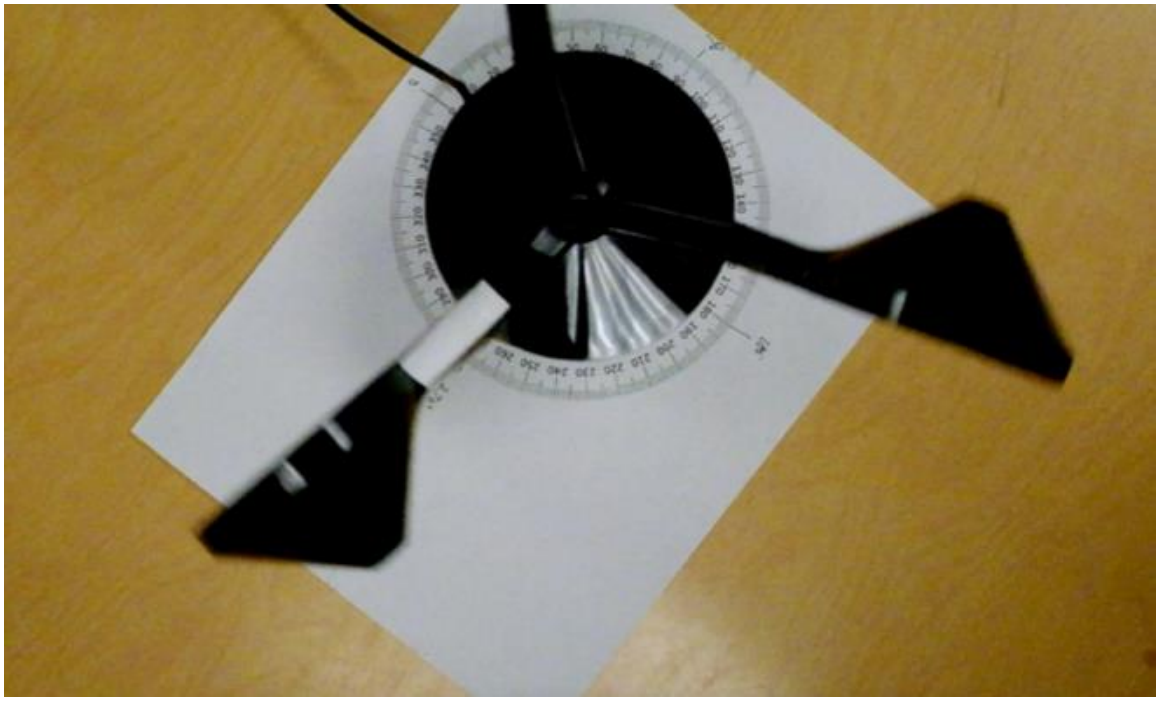

Figure 2.4: Experiment of cup anemometer's motion

The experimental results for the HOBO U30 cup anemometer indicate a linear relationship between constant wind speed and cup rotational speed, with coefficients $k = 0.6639$ and $b = 0.07797$.

2.3.1.2 Field Calibration in Natural Winds

The Hobo cup anemometer was placed side-by-side with a Ruby Electronics DT-8880 hot-wire anemometer. The anemometers were installed on a T-bar approximately 2 m above a rooftop, which is approximately 25 m above the ground. The measurement site is shown in Figure 2.5. The hotwire anemometer is used as the best approximation of the true wind speed: small inaccuracies

are introduced by the thermal mass of the wire, but this effect is assumed to be significantly smaller than that caused by the inertial moment and frictional resistance of the cup anemometer.

Figure 2.5: Comparison field measurement campaign

Fifteen side-by-side samples were recorded by cup and hot-wire anemometers, of which 10 successfully captured a full 20 minutes with a steady wind direction. The time-histories and statistical moments of these samples form the bases of the dynamic calibration example.

2.3.2 Mean Speeds of Natural Winds

Two mean wind speed prediction methods are critically compared in this section. Coefficients *k* and *b* identified in the lab are used for both methods. The first method is to apply the CDM on side-by-side time histories to compute the resistance parameter $\widetilde{C}$ and then computes $\widetilde{C}^*$ from the resulting values of $\widetilde{C}$. The second method is to directly apply Equation 2.16 to the mean wind

speeds measured by each of the two anemometers plus the standard deviation measured by the hotwire to find the mean resistance parameter $\widetilde{C}^*$.

2.3.2.1 Identification of Resistance Parameter $\widetilde{C}^*$

2.3.2.1.1 Identification from Side-by-side Time Histories

The ten 20-minute side-by-side datasets resulting from Section 3.1.2 are used to determine the inertia and resistance parameters. A large number of inertia coefficients $\widetilde{I}_i$ and inertia parameters $\widetilde{C_i}$ are computed using repeated applications of Equation 2.7 to all ten available side-by-side time histories. The average of the $\widetilde{I}_i$ is 4.5598. Individual values of the resistance parameter $\widetilde{C_i}$ are shown in Figure 2.6 as black circles, after removal of obvious outliers, such as negative or large $\widetilde{C_i}$ value at low wind speed range. A least-squares quadratic regression for $\widetilde{C}^*$ yields coefficients r_1, r_2 and r_3 as 0.1165, 1.02, and 1.55, respectively. The plot of $\widetilde{C}^*$ is shown as the blue line on Fig 2.6. A time history of the true wind speed can then be reconstructed from the cup data using Equation 2.10.

The validity of using a least-squares quadratic fit to find values of r_1, r_2 and r_3 is tested by using an exhaustive search to find the set of r_1, r_2 and r_3 that minimize the Euclidean distance between the recalibrated cup data and the contemporaneous hotwire data.

Euclidean distance is commonly used to quantify the similarities between two time series (Agrawal, et al, 1994). In this case, competing sets of r_1, r_2 and r_3 are exhaustively searched to

minimize the square root of the sum of squares differences, calculated as $ED(\vec{x},\vec{y}) = \sqrt{\sum_{i=1}^{n}(x_i - y_i)^2}$. The resulting optimal set of coefficients r_1, r_2 and r_3 are 0.1065, 1.06, and 1.52, respectively, with the resulting "Best Estimate" of $\widetilde{C}^*$ shown as the red dashed line in Figure 2.6. It is important to note that these coefficients are published to demonstrate the method, and should not be used in an actual recalibration application. These coefficients were generated exclusively from low wind speeds: the measured side-by-side data used to generate these coefficients had a maximum mean wind speed of 5.3m/s. The resistance parameter is a quadratic function of wind speed, so extrapolating the resistance parameter to higher wind speeds introduces a potential for very large recalibration errors. A recalibrated time history resulting from use of these resistance coefficients combined with a much higher wind speed was found to be unrealistic; a different set of resistance coefficients has been identified that gives realistic recalibration of higher speed winds, but at present there is insufficient experimental data to support the new set of coefficients.

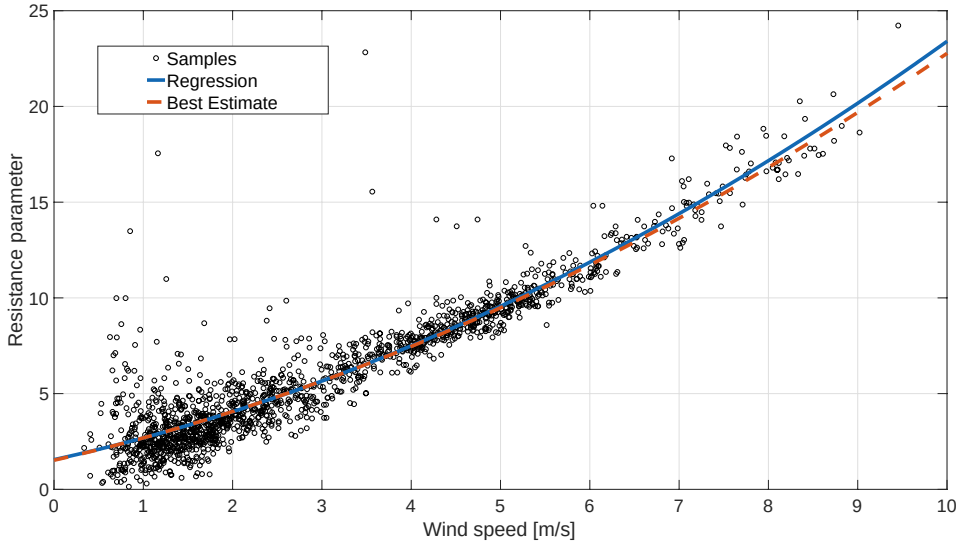

Figure 2.6: Resistance parameters $\widetilde{C}$ and $\widetilde{C}^*$

2.3.2.1.2 Identification from Side-by-side Means and Standard Deviation

Equivalent resistance coefficients r_1, r_2 and r_3 can be computed directly from side-by-side means as measured by the two anemometers combined with the standard deviation of the true wind. Individual values of $\widetilde{C}^*$ computed directly from Equation 2.16 are plotted as a function of mean wind speed in Figure 2.7, with the numerical value of the standard deviation shown near each point. Sample 9 was deleted from this dataset as an obvious outlier. A three-dimensional least-squares fit though the remaining data yields coefficients r_1, r_2 and r_3 to be 0.1047, 1.059, and 2.158. The colored lines on Figure 2.7 show the result of Equation 2.16 using these coefficients and selected constant values of standard deviation. These coefficients are based on low speed measurements only and use of them for high wind speed conditions would not be appropriate, as mentioned in Example 3.2.1.1.

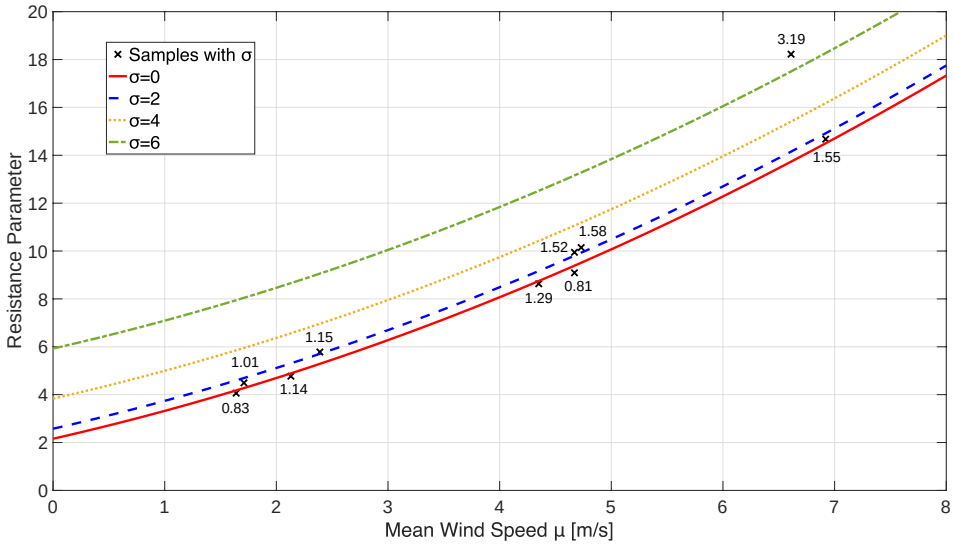

Figure 2.7: Resistance parameter $\widetilde{C}^*$ from mean and standard deviation

2.3.2.2 Recalibration of Measured Cup Data

Three recalibration methods are available. The optimal method would be application-specific, depending on the data needs and availability. Recalibration of a complete wind time-history is based on Equation 2.10. Recalibration of the mean wind speed only is based on Equation 2.16 if the standard deviation of the wind is known; recalibration of the mean only is also possible using an IEC recommended turbulence if the true turbulence is not known.

Figure 2.8 shows time histories of hot-wire, adjusted cup, and original cup. The recalibration brings both the mean wind speed reported by the cup much closer to the hotwire, and also provides a much better fit near the peaks than the raw cup data.

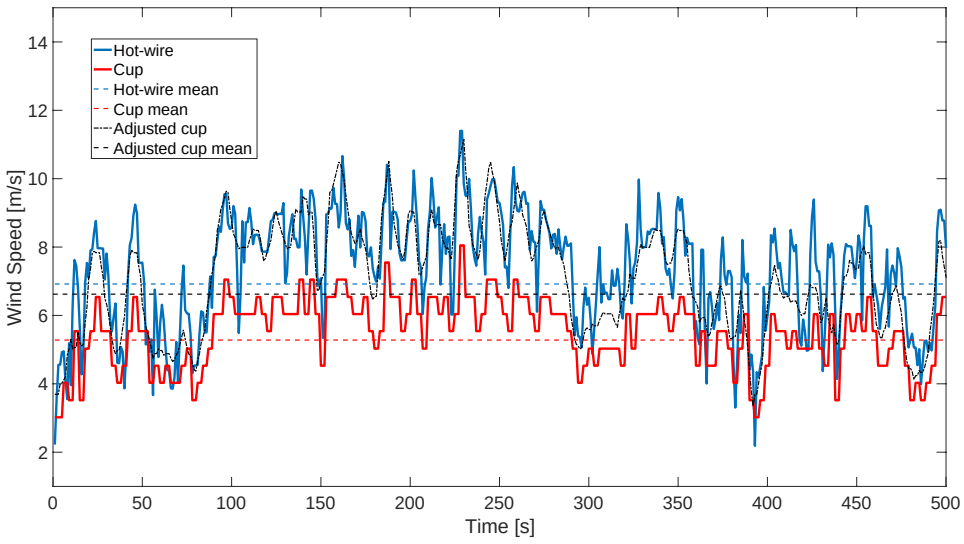

Figure 2.8: Wind speed time histories

2.3.2.2.1 Recalibration of Wind Speed Time Histories and Mean Wind Speeds If Turbulence Is Known

Each of the ten statistically stationary time histories is recalibrated point-by-point using Equation 2.10 with r_1, r_2 and r_3 as 0.1165, 1.02, and 1.55. The mean of each of these 10 time-histories is shown in Table 2.2 as μ_t. The recalibrated mean shows generally good agreement with the hotwire data, and much better agreement than the unadjusted cup data. The next two columns of Table 2.2, $\dagger\mu$ and $\ddagger\mu$, show results computed using Equation 2.16, but using different values of the calibration coefficients. Results in column $\dagger\mu$ use the value of $\widetilde{C}^*$ computed in 3.2.1.1; results in column $\ddagger\mu$ use the value of $\widetilde{C}^*$ computed in 3.2.1.2. The overall results suggest that the mean of a recalibrated time history approximately equals the mean resulting from direct recalibration, and the recalibration is not highly sensitive to which method is used to determine $\widetilde{C}^*$

Sample	μ_c	μ_h	σ_h	μ_t	$\dagger\mu$	$\ddagger\mu$
1	1.37	1.64	0.83	1.74	1.52	1.69
2	1.44	1.71	1.01	1.80	1.51	1.68
3	1.96	2.13	1.14	2.40	2.02	2.20
4	1.95	2.40	1.15	2.37	2.13	2.30
5	3.71	4.35	1.29	4.56	4.28	4.43
6	3.78	4.68	1.52	4.70	4.45	4.59
7	3.84	4.67	0.81	4.74	4.63	4.77
8	3.81	4.73	1.58	4.77	4.50	4.63
9	4.57	6.62	3.19	6.12	5.73	5.79
10	5.28	6.92	1.55	7.23	6.87	6.94

μ_t: computed from adjusted cup speed time-history, m/s
$\dagger\mu$, $\dagger\sigma$: $\widetilde{C}^*$ computed from $\widetilde{C}$, m/s
$\ddagger\mu$, $\ddagger\sigma$: $\widetilde{C}^*$ computed from μ_c, μ_h, and σ_h, m/s

Table 2.2: Comparison of recalibration methods

2.3.2.2.2 Recalibration of Mean Wind If Measured Turbulence Is Not Available

If the standard deviation of wind speed σ is unknow, it can be estimated by IEC normal turbulence model. The definitions of various turbulence models can be found at IEC regulations (IEC, 2006), including the Normal Turbulence Model (NTM). The NTM model gives an expression for the mean value of the turbulence:

$$\sigma = I_{ref}(0.75\mu + 3.8) \tag{2.18}$$

Where μ is the mean of the true wind speed, I_{ref} is the expected value of hub-height turbulence intensity at a 10 min average wind speed of 15 m/s. IEC gives values of I_{ref} of 0.16, 0.14, and 0.12 for NTM Class A, B, and C respectively. The true wind speed is not generally known directly from cup data, such that the recalibration to find the true mean wind speed requires simultaneous solution of Equations 2.14, 2.16.

Table 2.3 shows two pairs of μ and σ computed using each of the two sets of coefficients r_1, r_2 and r_3 developed in Example 3.2.1 and the value of $I_{ref} = 0.16$ representing IEC NTM Model A. The result based on fitting the cloud consistently under predicts the results based on fitting means. Each set of results relies a different equation for $\widetilde{C}^*$, each of which is based on a single data-fit (Figures 2.6 and 2.7). Results in columns †μ and †σ use the value of $\widetilde{C}^*$ computed in 3.2.1.1; results in columns ‡μ and ‡σ use the value of $\widetilde{C}^*$ computed in 3.2.1.2. The systematic differences

between these two sets of predictions of the mean are believed to be caused by the imprecise algebraic representation of $\widetilde{C}^*$computed from each of the two the data fits.

Sample	μ_c	μ_h	σ_h	†μ	†σ	‡μ	‡σ
1	1.37	1.64	0.83	1.48	0.79	1.72	0.82
2	1.44	1.71	1.01	1.56	0.80	1.80	0.82
3	1.96	2.13	1.14	2.14	0.87	2.41	0.90
4	1.95	2.40	1.15	2.13	0.86	2.40	0.90
5	3.71	4.35	1.29	4.27	1.12	4.57	1.16
6	3.78	4.68	1.52	4.37	1.13	4.67	1.17
7	3.84	4.67	0.81	4.45	1.14	4.75	1.18
8	3.81	4.73	1.58	4.41	1.14	4.71	1.17
9	4.57	6.62	3.19	5.56	1.28	5.83	1.31
10	5.28	6.92	1.55	6.82	1.43	7.01	1.45

†μ, †σ: $\widetilde{C}^*$ computed from $\widetilde{C}$, m/s
‡μ, ‡σ: $\widetilde{C}^*$ computed from μ_c, μ_h, and σ_h, m/s

Table 2.3: Predicted mean wind speed based on IEC turbulence model

2.3.3 Higher Statistical Moments of a Sea Breeze

The skewness and kurtosis are estimated from field data measured using a cup anemometer considering only those winds from the Gulf of Mexico near-perpendicular to the coast, which was taken here to be all winds from a heading of 145°± 30°.

2.3.3.1 Seasonal Field Measurement Campaign

A longer-term field measurement campaign was completed as part of this work to quantify the higher statistical moments of the natural winds blowing directly ashore from the Gulf of Mexico. The measurement campaigns represent a two-month deployment of a HOBO U30 weather station kit which includes a cup anemometer. Measurements began March 2017 with a continuous sampling rate of 1 Hz. The anemometer was positioned 10 m above the ground at 29°16'38.0"N, 94°48'40.4"W, which is on Galveston Island approximately 250 m from the Gulf of Mexico, as shown in Figure 2.9.

Figure 2.9: Field campaign locations

Figure 2.10 presents the raw field data as two monthly wind roses. The dominant wind direction is from the Gulf of Mexico towards land with a secondary peak from land towards the Gulf. Monthly wind roses of March 2017 and April 2017.

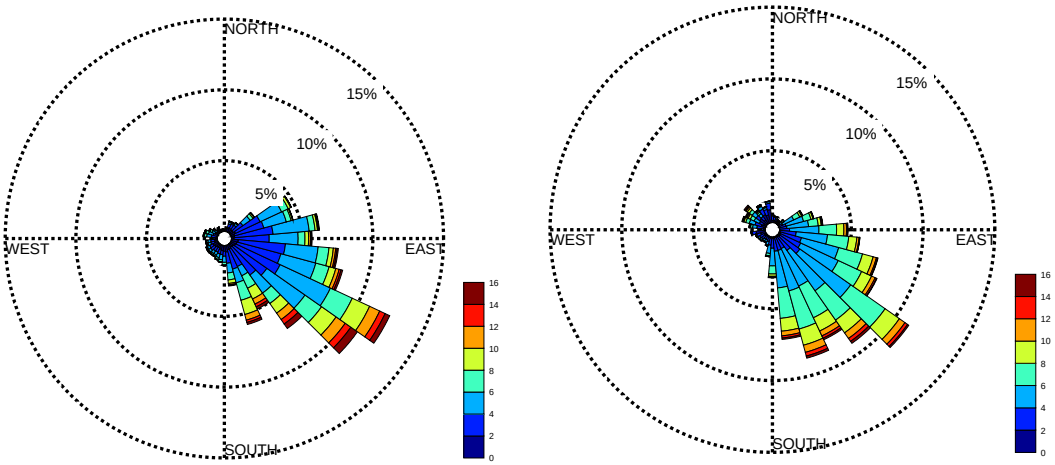

(a) March 2017 (b) April 2017

Figure 2.10: Monthly wind roses of raw data as measured at a coastal location

Winds from a heading of 145° plus or minus 30° are considered sea breezes for the purposes of computing statistical moments in this example. An analysis of winds from (direction) 160° +/-30° are considered land breezes in this analysis; an analysis of land breezes collected in the present data campaign plus an additional measurement set is offered as Appendix 1. Comparing statistics of the land vs sea breezes shows land breeze to have meaningfully higher turbulence, and that the turbulence is most affected by very local conditions because the winds off of Galveston Bay were statistically comparable to winds off the ocean.

2.3.3.2 Recalibration and Analysis of Measured Wind Data

The complete two-month time-history is recalibrated and then divided into 10-minute segments. Each segment is tested for statistical stationarity. Stationary segments with wind blowing from the Gulf are then binned by mean recalibrated wind speed. The statistical moments are then computed for all segments within each bin. The computed moments are averaged to represent the standard deviation, skewness and kurtosis as a function of wind speed.

The coefficients used in the recalibration are based on all available data from the fifteen sets of data originally collected as part of Example 3.2. Those parts of the five time-histories excluded from Example 3.2 that are believed to represent steady-state conditions have been included in this analysis such that the parameter $\widetilde{C}$ is estimated based on all available data. A best estimate of the resistance parameter $\widetilde{C}$ is made by an exhaustive search of r_1, r_2 and r_3 to minimize the Euclidean distance between hot-wire and adjusted cup data. The resulting values of coefficients r_1, r_2 and r_3 are 0.1265, 0.8107, and 1.684. The values of coefficients *k* and *b* are taken from section 3.1.1 to be 0.6639 and 0.07797, respectively.

Each 10-minute segment resulting from the recalibration is tested for statistical stationarity using the reverse arrangement test (Kendall, 1938 as improved by Mann, 1945). The test applied a threshold *z*-value of 2.576, corresponding to a 99% confidence interval in which $z = (R - \mu_R)/\sigma_R$ where $\mu_R = \frac{N(N-1)}{4}$ and $\sigma_R^2 = \frac{2N^3+3N^2-5N}{72}$. The first four statistical moments are calculated for each ten-minute stationary segment of the sea breeze process. The segments are

then binned by the recalibrated mean wind speed and the average of each statistical moment is computed for each bin and presented as Table 2.4.

Wind speed	$\bar{\sigma}$	$\overline{\alpha_3}$	$\overline{\alpha_4}$	σ_σ	σ_{α_3}	σ_{α_4}
4	0.77	0.20	2.71	0.14	0.30	0.48
5	1.00	0.35	3.04	0.20	0.35	0.64
6	1.37	0.62	3.48	0.27	0.41	1.25
7	1.71	0.70	3.70	0.34	0.46	1.48
8	2.08	0.87	4.24	0.47	0.46	1.75
9	2.48	0.88	4.18	0.50	0.48	1.83
10	2.99	1.00	4.50	0.58	0.50	2.09
11	3.52	1.10	4.71	0.68	0.49	1.93
12	3.82	1.08	4.81	0.76	0.44	1.65
13	4.49	1.16	4.77	0.93	0.47	1.68

Table 2.4: Statistical parameters of sea breeze (145°± 30°)

A small number of outliers are found at high wind speed bars according to their Normal plot figures. These outliers are neglected during the computation to avoid its influence to the accuracy of statistical parameters of sea breeze.

Figure 2.11 shows the higher statistical moments of the observed coastal sea breezes. The process is observed to have higher statistical moments that also vary with mean wind speed and differ significantly from the Gaussian values of zero and three.

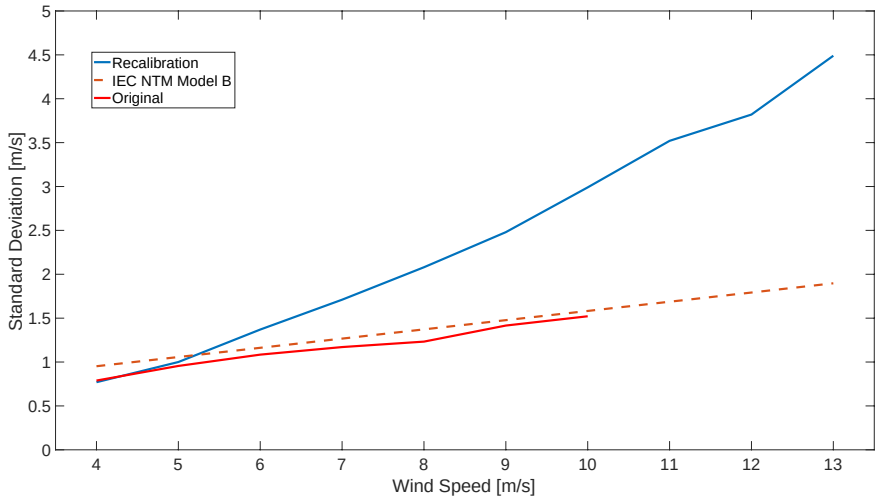

(a) Standard deviation

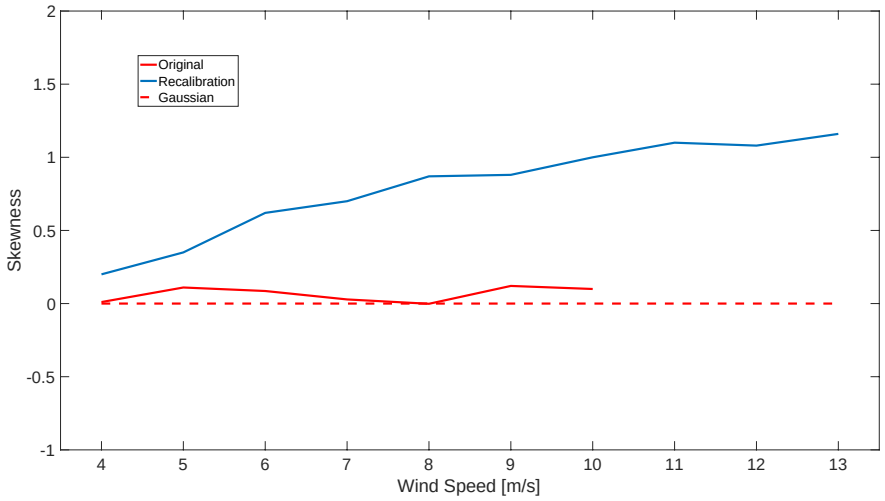

(b) Skewness

Figure 2.11: Higher statistical moments

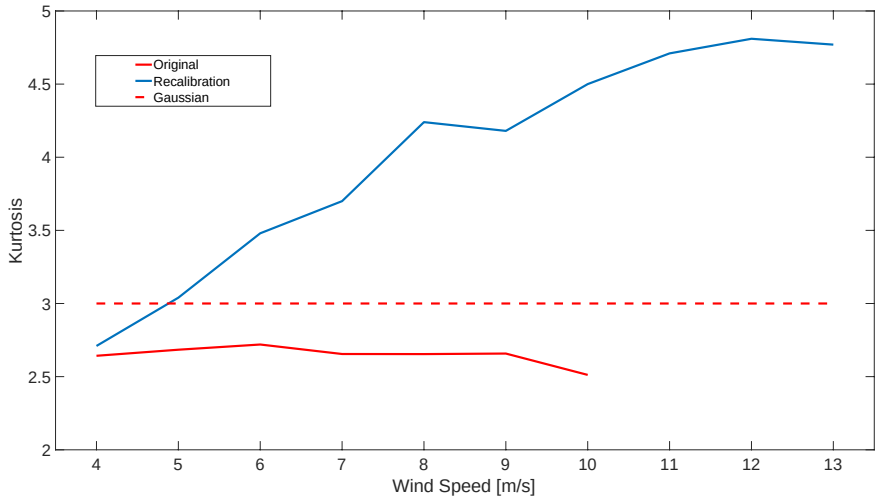

(c) Kurtosis

Figure 2.11continued.

Figure 2.12 shows a normal plot for the measured data for mean wind speeds of 8 and 10 m/s. The large deviations from the straight line representing a Gaussian process show that the observed process deviates significantly from the Gaussian, and that extremes of the 8 m/s winds would be significantly underpredicted using a Gaussian process assumption. Comparing the recalibrated cup data with the raw cup data shows that use of the raw cup data could lead to a sever underprediction of the expected maximum 10-min gust wind. The mean max of 55 segments in the 8m/s bin is 10.95 m/s before recalibration and 16.21 m/s after recalibration; the mean max in the 10m/s bin is 22.22 after recalibration. These extreme results are for the binned data only, and would be considered in addition to the recalibration of the mean. A cut-off line at 32 m/s are applied to 10 m/s winds according to the obviously gap in Normal plot. Data points above the cut-off line are not including in the computation of higher statistical moments. Similar cut-off lines are selected

for other higher wind speed bars as well. The skewness of 11 m/s, 12m/s, and 13 m/s would be 1.17, 1.10, and 1.17 without cut-off lines. The kurtosis of 11 m/s, 12m/s, and 13 m/s would be 5.30, 5.02, and 4.99 without cut-off lines.

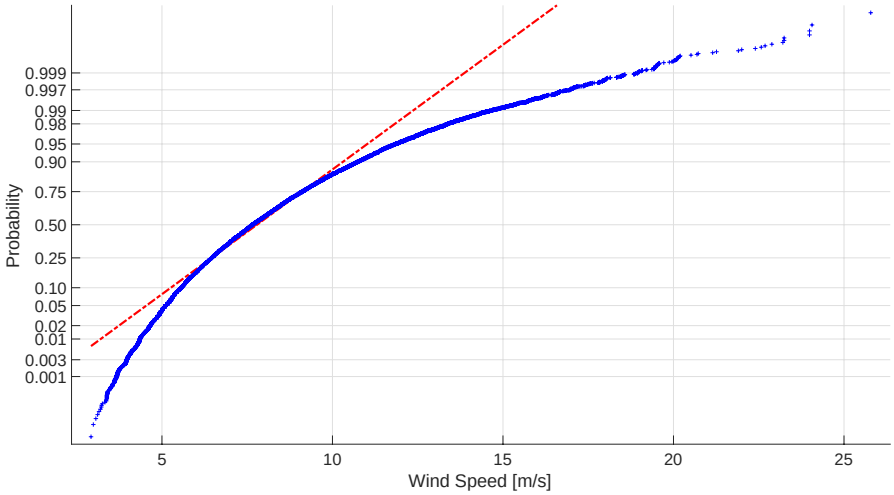

(a) 8m/s, $\alpha_3 > 0, \alpha_4 > 3$

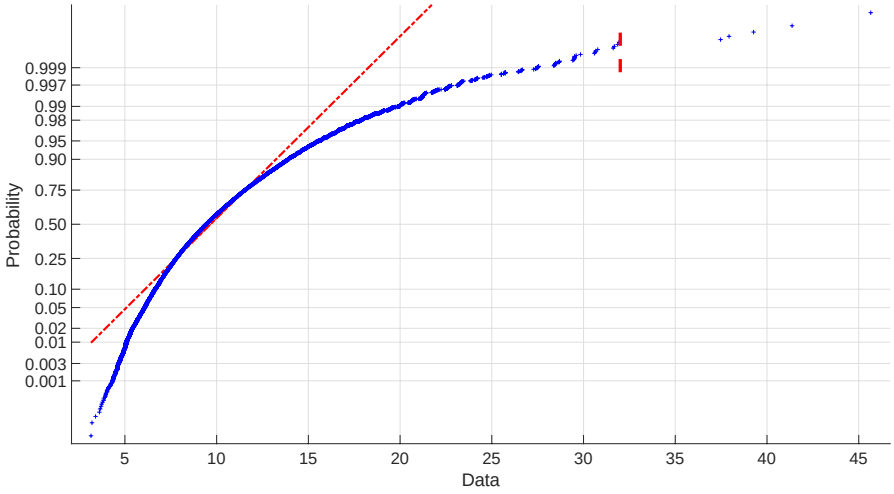

(b) 10m/s, $\alpha_3 > 0, \alpha_4 > 3$

Figure 2.12: Normal Plot for wind speed data in different bars

Figure 2.13 shows a plot of number of segments within each wind speed bin. The plot shows the general recalibration shift toward higher wind speeds. Very little raw data was collected having mean wind speeds of 8m/s and above and virtually none for 10m/s and above. Further, the resistance coefficients used in the recalibration are based on side-by-side data having a maximum mean wind speed of 5.28 m/s (cup) and 6.92 m/s (hot-wire). Use of the higher statistical moments computed using the recalibration method on wind speeds higher than the basis of the calibration coefficients may not be appropriate.

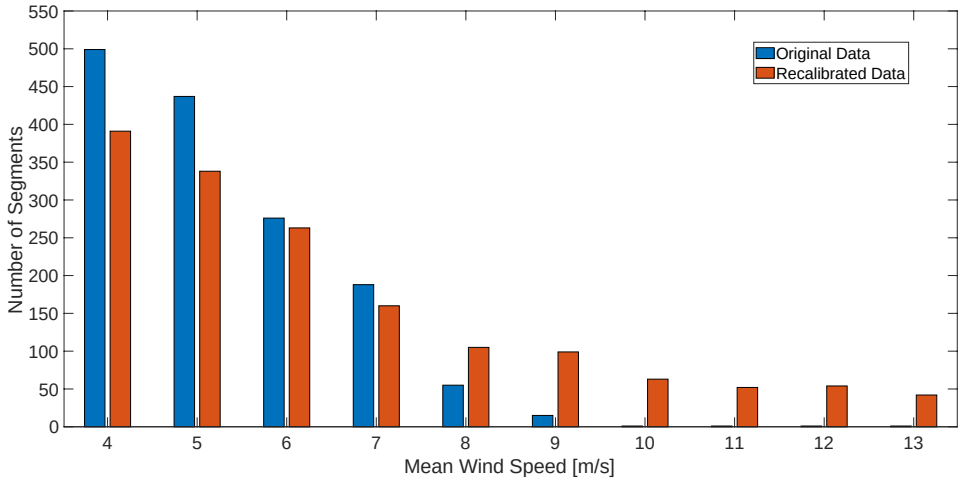

Figure 2.13: Number of segments in each wind speed bar

2.4 Conclusion

Instantaneous and mean wind speeds measured by a cup anemometer are observed to differ meaningfully from measurements measured using a hotwire anemometer in natural turbulent wind conditions. A new recalibration method is developed to increase the accuracy of instantaneous wind speeds as measured by cup anemometers. Derivation of the new method is based on the

dynamic equation of motion of the rotor, including the rotational mass moment of inertia and varying aerodynamic force coefficients on the cups. Results of the derivation show that the instantaneous and mean wind speeds depend on the mass-moment of the rotor and on changing aerodynamic force coefficients. These dynamic effects are explicitly included in a new recalibration method that increases the prediction accuracy of cup anemometers in turbulent winds. The new method is demonstrated by application to side-by-side wind speed data to develop instantaneous and mean wind speed corrections, and used to compute the short-term higher-order statistics of coastal winds.

The new method requires experimental recalibration of the cup anemometer. Measurements in steady wind conditions are used to establish coefficients relating steady wind speeds to cup rotation speeds. Differences between time-histories of the true wind speed in natural turbulent conditions and corresponding time histories recorded by a cup anemometer are used to establish parameters relating acceleration of the cup rotor to rotational moments applied by the wind. The resulting parameters can be used to recalibrate instantaneous wind speed time-histories, or used in conjunction with turbulence intensity to recalibrate mean wind speeds.

The new methodology is expected to be useful in practical applications and can be applied to any type of cup anemometer. Each cup anemometer can be recalibrated in a limited number of wind conditions spanning the target wind speed range, and the resulting recalibration equations can be applied in a much broader range of wind velocities and turbulence levels. Mean velocities of existing or historical data measured using cup anemometers can also be recalibrated as long as a calibration coefficient can be developed for the anemometer used. Complete wind time histories

can be recalibrated point-by-point, and subsequently used to compute statistical moments of the wind, including standard deviation, skewness and kurtosis.

Two months of high-fidelity cup data was recalibrated and used to estimate the higher statistical moments of coastal sea breezes. The resulting higher-order statistical moments of short-term winds do not conform to the commonly used Gaussian assumption. The computed values of standard deviation, skewness and kurtosis of the measured sea breeze are listed in Table 2.4.

3. TRANSFORMATION OF WIND TURBINES POWER CURVE USING THE STATISTICS OF THE WIND PROCESS

3.1 Introduction and Background

3.1.1 Introduction

The International Electrotechnical Commission (IEC) (IEC, 2005) recommends computing annual energy production using a practical power curve measured from an operating wind turbine. A practical power curve is generally constructed from measured 10-minute means of power and wind speed, such that the resulting curve implicitly includes all effects of irregularities in the wind as well as the turbine control-system dynamic response. Practical power curves can be significantly different from ideal turbulence-free power curves and can be useful in project planning and design, but these curves cannot be accurately constructed from field measurements prior to siting a wind turbine in the actual wind conditions for the proposed location. The importance of practical power curves is heightened because the practical curve always predicts less power than the ideal curve, and the largest differences are near the rated speed of the turbine. These differences result mainly from the system being unable to shift instantaneously between control strategies when subject to short-term variations in the wind speed. Torque-control is applied to the wind speeds that are only briefly above the rated, and pitch control is applied to winds that are only briefly below the rated. In this work, the wind speed is treated as a random variable and expressions are derived to quantify the instantaneous power produced by wind speeds above and below the rated speed. The

development begins with an assumption of a Gaussian wind process, and is subsequently extended to include non-Gaussian effects.

The methodology developed here enables transformation between the manufacturer's power curve and a practical power curve using the statistical moments of the wind process. This new methodology can be used to predict actual turbine output based on the idealized power curves, or the inverse of the new transformation can be used to develop zero-turbulence performance curves using field data measured in actual turbulent conditions.

Other researchers have applied statistical methods to develop estimate power generation. Carrillo (Carrillo, et al, 2013) shows that the cubic and exponential functions are each an excellent fit for the torque-controlled region of practical power curves for commercial FOWTs. Shokrzadeh et al (Shokrzadeh, et al, 2014) introduce a locally weighted polynomial regression method to define a power curve using both simulated datasets and measured data from a wind farm. Advanced statistical methods have also been investigated as an alternative to power curves. Multiple researchers, (e.g., Li et al., 2001, Mabel and Fernandez, 2008 and Kusiak, et al., 2009) each develop and verify the effectiveness of artificial neural network models using field-data measured on various wind farms. Kusiak goes on to suggest his model could also be applied to wind farm management, individual turbine control and energy generation optimization.

The work presented here differs from that prior statistical work in that this work is based on treating the wind process and output power as random processes, and recognizing two distinct operational control modes. The resulting transformation between ideal and practical power curves can be

directly applied to applied to any wind turbine design by determining a limited number of parameters from either field measurements or numerical simulations.

The remainder of Section 1 gives necessary technical background and common nomenclature for the theoretical developments; Section 2 gives the theoretical developments for winds that are initially assumed to be a Gaussian process, then these developments are extended to non-Gaussian winds; Section 3 includes a series of examples demonstrating the importance of turbulence intensity, the relative importance of non-Gaussian effects, and application of the method to compute annual energy production.

3.1.2 Background

3.1.2.1 Manufacturer's Power Curve

The manufacturer's power curve (Figure 3.1) represents the performance of a wind turbine in steady wind, which systematically overestimates the power production (e.g., Böttcher, F., et al, 2007). The control system operates the turbine in one of two fixed modes depending on the mean wind speed: a torque-controlled mode and a pitch-controlled mode. No power is generated when the mean wind speed is below or above the cut-in or cut-out speeds (u_{cut-in}, and $u_{cut-out}$) because the turbine is not operated in very high or low wind speeds (Jonkman, et al., 2009).

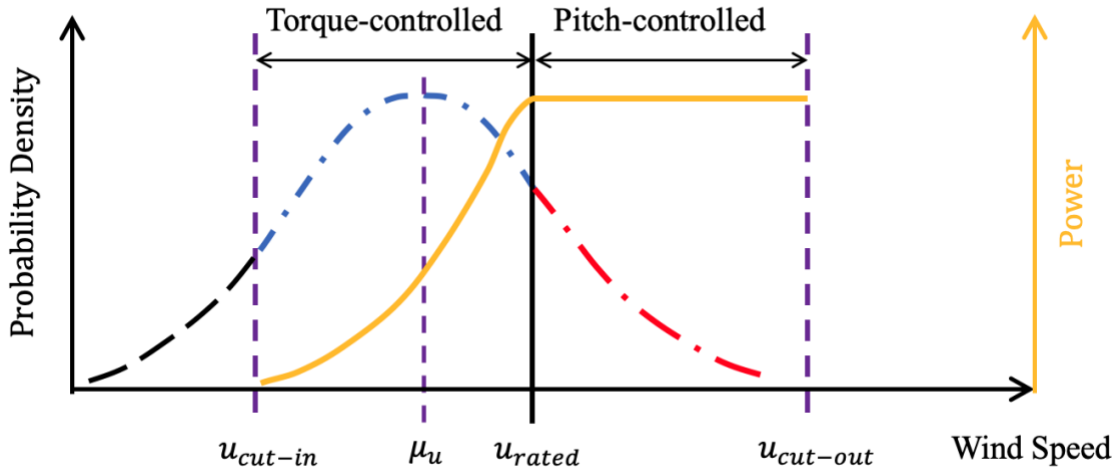

Figure 3.1: Truncated distribution model of wind speed

The rising section of the power curve between the cut-in and cut-out speeds is the torque-controlled region, in which the rotor torque is adjusted by the control system to optimize the spin rate and energy output. The instantaneous Power, P_i, is commonly estimated as $P_i = P(u_i) = ku_i^3$ (e.g., Pardalos, et al., 2013), in which k is a power coefficient and P_i and u_i are the instantaneous values of the power and wind speed.

The flat section of the power curve, between the rated and cut-out speeds, is the pitch-controlled region, in which the control system feathers the blades to limit the torque and spin rate to prevent damage to the turbine operating in high winds. The power output for instantaneous wind speeds in the pitch-controlled region can realistically be estimated as the rated power of turbine: $P_i = P_r$.

3.1.2.2 Truncated Gaussian Wind Process

Wind speeds around a fixed mean are observed to be a weakly non-Gaussian process (e.g., Dai and Sweetman, 2020). Approximating winds as a Gaussian process enables computation of the mean and standard deviation of the wind speeds bounded between u_a and u_b using a truncated normal distribution (e.g., Kotz, et. al, 2004):

$$\mu_r = \mu + \sigma \frac{\phi(\alpha) - \phi(\beta)}{\Phi(\beta) - \Phi(\alpha)} \tag{3.1}$$

$$\sigma_r = \sigma \sqrt{1 + \frac{\alpha\phi(\alpha) - \beta\phi(\beta)}{\Phi(\beta) - \Phi(\alpha)} - \left[\frac{\phi(\alpha) - \phi(\beta)}{\Phi(\beta) - \Phi(\alpha)}\right]^2} \tag{3.2}$$

Where, μ and σ are the mean and standard deviation of the wind process, and ϕ and Φ are the PDF and CDF of the normal distribution, such that $\Phi(\beta) - \Phi(\alpha)$ is the fraction of total probability within the truncated region. Coefficients α and β are standard normal representations of the boundaries of domain: $\alpha = (u_a - \mu)/\sigma$ and $\beta = (u_b - \mu)/\sigma$.

3.1.2.3 The Hermite Transformation

The Hermite moment model (e.g., Winterstein, 1988; Sweetman and Choi, 2010) is a transformation that enables a one-to-one mapping between any Gaussian process and an equivalent mildly non-Gaussian process. The transformation maintains the fractile of every point in the process, while tuning the entire process to specified skewness and kurtosis.

3.2 Theoretical Development

There are four distinct operational modes shown by the blue line in Figure 3.1. Winds can be represented more realistically as a mean and a distribution about that mean, as shown on the black line. The distribution about the mean wind speed causes a wind turbine to have some probability of operating in each of the two operational modes for any specified mean wind speed. The power available at a constant mean wind speed can be computed by combining the distribution of wind speeds with the power curve and summing the contributions from each of the two regions.

The distribution of wind speeds is truncated by the three wind speeds separating the power curve into two operating regions. The area under each operating region of the truncated distribution is used to quantify the fraction of time in which the wind turbine is operating in that region; multiplying the power by the total duration over which the wind can be represented as having constant mean and standard deviation yields the energy produced.

3.2.1 Power Curve Transformation Using a Truncated Gaussian Model

The expected power for any operating condition can be computed as the sum of the power generated by the instantaneous winds in each of the two regions. The generator control strategy applied in the torque-controlled region is intended to extract the maximum instantaneous power from the available wind, such that instantaneous power in the torque-controlled region can be expressed as a function of the cube of the instantaneous wind speed, $P_1 = k_1 u_i^3$. The control strategy in the pitch control region should ideally extract the rated power continuously, regardless

of increasing wind speed, $P_3 = P_r u_i^0 = P_r$. However, practical limitations preclude output power remaining constant in the presence of turbulent winds, such that the output power can be approximated as a function of some unknown power of the wind speed, $P_2 = k_2 u_i^x$, with x generally expected to be between 0 and 3.

3.2.1.1 Estimation of Power Generated in the Torque-Controlled Region

The total expected power in the torque-controlled region for that region R_1 can be computed as a function of wind speed times the probability of that speed. Representing the instantaneous power in the torque-controlled region as $P_1 = k u_i^3$ and integrating over arbitrary probability density function g_1, which represents wind speeds in region R_1:

$$E(P_1) = \int_{u_{cut-in}}^{u_r} P_1(u) g_1(u) du = \int_{u_{cut-in}}^{u_r} k_1 u^3 g_1(u) du \quad (3.3)$$

Where distribution g_1 generally varies with geographic location and constant k_2 varies with individual wind turbine design. The power function $k_1 {u_i}^3$ can be expanded about the mean μ_1 as a Taylor series. of the wind speeds in region R_1, the mean of the region between the cut-in and rated wind speeds:

$$E(P_1) = \int_{u_{cut-in}}^{u_r} \left[P_1(\mu_1) + (u - \mu_1) {P_1}'(\mu_1) + \frac{1}{2}(u - \mu_1)^2 {P_1}''(\mu_1) \right] g_1(u) du \quad (3.4)$$

In which μ_1 is the centroid of the region of the PDF between the cut-in and rated wind speeds calculated using Equation 3.1. The first and second derivatives of the power $P_1(u)$ are $P_1{}'(u) = 3k_1u^2$ and $P_1{}''(u) = 6k_1u$. Substituting $P_1(u) = k_1u^3$, $\int_{u_{cut-in}}^{u_r} ug_1(u)du = \mu_1$ and $\int_{u_{cut-in}}^{u_r} g_1(u)du = 1$ into Equation 3.4 yields a second-order approximation of the expected power.

$$E(P_1) = P_1(\mu_1) + \frac{1}{2}Var_1(u)P_1{}''(\mu_1) \tag{3.5}$$
$$= k_1{\mu_1}^3 + 3k_1\mu_1{\sigma_1}^2$$

In which $Var_1(u)$ is the variance of the wind speeds between the cut-in and rated speeds, $Var_1(u) = {\sigma_1}^2$, calculated from the standard deviation of the wind process using Equation 3.2.

The variance of the power can also be computed directly from the statistics of the wind. The variance of the power can be represented using the definition of variance:

$$Var(P_1) = \int_{u_{cut-in}}^{u_r} [P_1(u) - E(P_1)]^2 g_1(u)du \tag{3.6}$$

Substituting Equation 3.5 into Equation 3.6 and using the first three terms of the Taylor series expansion of $P_1(u)$ yields the variance of power $Var(P_1)$:

$$Var(P_1) = Var_1(u)P_1{}'(\mu_1)^2 + E(u-\mu_1)^3 P_1{}'(\mu_1)P_1{}''(\mu_1) \tag{3.7}$$

$$+\frac{1}{4}E(u-\mu_1)^4 {P_1}''(\mu_1)^2 - \frac{1}{4}{Var_1}^2(u){P_1}''(\mu_1)^2$$

In which the expectation in the second and third terms can be recognized as the third and fourth raw moments of wind speed within R_1, which are small for a Gaussian process. Neglecting these higher moments yields an expression for the variance of the power resulting from winds within R_1 only:

$$Var(P_1) = Var_1(u){P_1}'(\mu_1)^2 - \frac{1}{4}{Var_1}^2(u){P_1}''(\mu_1)^2 \tag{3.8}$$

Substituting $Var_1(u) = {\sigma_1}^2$, ${P_1}'(u) = 3k_1u^2$ and ${P_1}''(u) = 6k_1u$ into Equation 3.8 yields the standard deviation of the power in the torque-controlled region R_2:

$$Std(P_1) = 3k_1\mu_1\sigma_1\sqrt{{\mu_1}^2 - {\sigma_1}^2} \tag{3.9}$$

The likelihood, L_{R1}, of instantaneous winds being in torque-controlled region R_1 during any statistically stationary period is:

$$L_{R1} = \Phi(\beta) - \Phi(\alpha) \tag{3.10}$$

Where, α and β is the standard normal representation of the cut-in and rated speed: $\alpha = (u_{cut-in} - \mu)/\sigma$ and $\beta = (u_{rated} - \mu)/\sigma$. Likelihood L_{R1} is assumed to also represent the

number of discrete time points u_i during which the turbine is operating in the torque-controlled region within any statistically stationary period.

3.2.1.2 Estimation of Power Generated in the Pitch-Controlled Region

A typical manufacturer's power curve shows constant power output for all wind speeds beyond the rated, which represents the pitch-controlled region, R_2. The mean power output for instantaneous winds speeds above the rated is set by the control system to the rated power:

$$E(P_2) = P_r \tag{3.11}$$

Imperfections in the instantaneous control in turbulent winds lead to variations in instantaneous power, in which the exponent of the wind speed is an unknown constant depending on overall wind turbine and controller characteristics including the angle between the incoming wind and the rotor:

$$P_2(u) = k_2 {u_i}^x \tag{3.12}$$

Where the power coefficient k_2 remains constant for any fixed set of values representing the mean wind speed, turbulence and exponent x.

Repeating the derivation of Equations 3.4 and 3.6 for application to P_2 and substituting the derivatives $P_2{}'(u) = xk_3u^{x-1}$ and $P_2{}''(u) = x(x-1)k_3u^{x-2}$ yields a second-order approximation of the expected power and variance of power.

$$E(P_2) = P_2(\mu_2) + \frac{1}{2}Var_2(u)P_2{}''(\mu_2) \tag{3.13}$$

$$= k_2{\mu_2}^x + \frac{1}{2}x(x-1)k_2{\sigma_2}^2{\mu_2}^{x-2}$$

$$Var(P_2) = Std^2(P_2) = Var_2(u)P_2{}'(\mu_2)^2 - \frac{1}{4}{Var_2}^2(u)P_2{}''(\mu_2)^2 \tag{3.14}$$

$$= x^2{k_2}^2{\mu_2}^{2x-2}{\sigma_2}^2 - \frac{1}{4}x^2(x-1)^2{k_2}^2{\mu_2}^{2x-4}{\sigma_2}^4$$

In which μ_2 is the centroid of the region of the PDF between the rated and cut-out wind speeds calculated using Equation 3.1, $Var_2(u)$ is the variance of the wind speeds between the rated and cut-out speeds, $Var_2(u) = {\sigma_2}^2$, calculated from the standard deviation of the wind process using Equation 3.2.

Setting $E(P_2)$ equal to the rated power yields an expression for the power coefficient:

$$k_2 = \frac{P_r}{[1 + \frac{1}{2}x(x-1)(\frac{\sigma_2}{\mu_2})^2]\mu_2^x} \tag{3.15}$$

Substituting Equation 3.15 into Equation 3.14 yields the variance of the power.

$$Var(P_2) = \frac{{P_r}^2 x^2 (\frac{\sigma_2}{\mu_2})^2 - \frac{1}{4}{P_r}^2 x^2 (x-1)^2 (\frac{\sigma_2}{\mu_2})^4}{[1 + \frac{1}{2}x(x-1)(\frac{\sigma_2}{\mu_2})^2]^2} \quad (3.16)$$

Equation 3.16 can be reformatted into a quartic equation of *x*:

$${P_r}^2 x^2 (\frac{\sigma_2}{\mu_2})^2 - \frac{1}{4}{P_r}^2 x^2 (x-1)^2 \left(\frac{\sigma_2}{\mu_2}\right)^4 - Var(P_2)\left[1 + \frac{1}{2}x(x-1)\left(\frac{\sigma_2}{\mu_2}\right)^2\right]^2 = 0 \quad (3.17)$$

There can be only one solution of Equation 3.17 that satisfies Equation 3.13 because Equation 3.12 is monotonic for power vs wind speed.

The portion, L_{R2}, of the statistically stationary period in which the turbine is operating in the pitch-controlled Region, R_2, is computed from the normal distribution:

$$L_{R2} = \Phi(\gamma) - \Phi(\beta) \quad (3.18)$$

Where γ and β are the standard normal representation of the cut-out and cut-in speeds: $\gamma = (u_{cut-out} - \mu)/\sigma$; $\beta = (u_{rated} - \mu)/\sigma$.

3.2.1.3 Estimation of Power Generated in All Regions

The energy output for any steady wind condition is the sum of the expected power multiplied by time for each of the two regions, and the expected power for any one segment is the total energy output divided by the total duration of the segment:

$$E(P) = \sum_{j=1}^{4} E(P_j)\, L_{Rj} = E(P_1)L_{R1} + E(P_2)L_{R2} \tag{3.19}$$

$$= (k_1{\mu_1}^3 + 3k_1\mu_1{\sigma_1}^2)L_{R1} + P_r L_{R2}$$

The standard deviation of power output can be computed as a weighted average (e.g., Headrick, T. C., 2009):

$$Std(P) = \sqrt{\sum_{j=1}^{2} \{\, Std(P_j)^2 \;\; L_{Rj} + [E(P_j) - E(P)]^2 \; L_{Rj}\}} \tag{3.20}$$

$$= \sqrt{Std(P_1)^2 \; L_{R1} + Std(P_2)^2 \; L_{R2} + [E(P_1) - E(P)]^2 \; L_{R1} + [P_r - E(P)]^2 \; L_{R2}}$$

Equation 3.21 can be directly inverted to predict a zero-turbulence power curve equivalent to a manufacturer's ideal power curve:

$$P_i(u) = k_1 u^3 = \frac{E(P) - P_r L_{R2}}{({\mu_1}^3 + 3\mu_1{\sigma_1}^2)L_{R1}} u^3 \tag{3.21}$$

Where, mean μ_1 and standard deviation σ_1 , Likelihood L_{R1} and L_{R2} can be obtained from measured field data.

3.2.2 Inclusion of Non-Gaussian Effects

The theoretical developments presented so far rely heavily on Equations 3.2 and 3.3, which are strictly valid only for a Gaussian process. There is little evidence that natural winds are Gaussian, and short-term measurements by the authors have shown the wind process to have skewness and kurtosis values that differ from the Gaussian values of zero and three (Dai and Sweetman, 2020). The methodology developed here can be used on mildly non-Gaussian winds by applying the Hermite transformation to the cut-in, rated, and cut-out speeds. The fractiles associated with these values remain constant through the transformation, such that the areas of regions 1 and 2 are preserved.

The specific steps are to first transform the cut-in, rated, and cut-out speeds of the real non-Gaussian wind process to equivalent values having the same fractile in a Gaussian process, compute the means and standard deviations of regions 1 and 2 using Equations 3.1 and 3.2, and then transform the resulting Gaussian means back to the real non-Gaussian process. Details of the calculation are included in Example 3.

3.3 Examples

Four examples are presented to demonstrate the effectiveness of the new method. Most of the verification cases are based on direct simulation of the OC3-Hywind numerical model, which is commonly used in academic research. The first example demonstrates the efficiency of the forward and inverse transformations in the OC3-Hywind and on field-measured performance of a Vestas V90 3MW turbine; the second example demonstrates the effect of turbulence intensity on the transformation of the power curve; the third example demonstrates the relative importance of including the higher statistical moments of the wind process in the transformation, as well as the forth example shows the cumulative effect of including the statistical moments throughout the estimation of total AEP using historical observations of wind speeds.

3.3.1 Numerical Simulation Methodology

Time domain simulations are used to benchmark transformation results in each of the examples. These simulations are performed by generating numerical representations of the environmental conditions and then computing the dynamic response and instantaneous power output of the OC3Hywind turbine using an in-house time-domain numerical simulation tool Loose (Sweetman and Wang, 2011). The details of the simulation methodology and the OC3 Hywind numerical model are summarized below.

3.3.1.1 Simulations of Environmental Conditions

Wind time-histories are simulated using the NREL software package TurbSim, which uses a Fourier transform and coherence functions to simulate speed time histories. The output of TurbSim is a matrix of 3-dimensional wind speeds representing discrete points on a two-dimensional vertical rectangular grid (Jonkman, 2009). Wind speeds generated by TurbSim as a sum of sinusoids, which conforms to the central limit theorem and results in the simulated winds being a Gaussian process. Example 2 includes a transformation of the Gaussian wind field time-history into a non-Gaussian process using the Hermite transformation.

Wind forces are computed using the NREL subroutine AeroDyn, which uses blade-element theory to compute forces on the moving blades directly from a time-history of the wind. AeroDyn includes a built-in blade pitch controller that automatically transitions between the torque-controlled and pitch-controlled operational modes (Moriarty and Hansen, 2005). Total forces and moments are summed over the length of the blades and applied to the rotor hub.

Wind power is calculated directly as rotor torque times generator rotation speed: $P = \eta T_{Gen} \omega_{Gen}$. Electrical generator efficiency, η, is assumed to be 94.4% OC3-Hywind (Jonkman, et al, 2009).

All simulations used in the examples include motion of the hull through the water; the simulations used in the AEP prediction section of example 3 also include the effects of ocean waves. Ocean waves are represented as a time-history of an irregular sea state, which is simulated by summation of sinusoidal wave components (e.g., Jefferys, E. R., 1987). The water surface elevation is:

$$\zeta = \sum_{j=1}^{N} \sqrt{2S(\omega_j)\Delta\omega}\, sin(\omega_j t + \varphi) \tag{3.22}$$

where $S(\omega_j)$ is the ordinate of the wave spectrum computed at ω_j; $\Delta\omega$ is width of the wave frequency band; φ is a random phase angle drawn from a uniform distribution between zero and 2π, and the total number of frequencies, N, varies with sea state and has a minimum number of 1800 for the 13m/s wind condition.

The JONSWAP wave spectrum (Hasselmann, et al., 1973) is used to compute the spectral offset:

$$S(\omega) = \alpha \frac{g^2}{\omega^5} e^{-\frac{5}{4}\left(\frac{\omega}{\omega_P}\right)^{-4}} \gamma^{e^{-0.5\left(\frac{\omega-\omega_P}{\sigma\omega_P}\right)^2}} \tag{3.23}$$

Where, $\alpha = 5.061\left(\frac{\omega_P}{2\pi}\right)^4 H_s^2(1 - 0.287\, log\, log\, \gamma)$; peak enhancement coefficient γ is set to 3.3; H_s is the significant wave height, and $\omega_P = \frac{1}{T_p}$ is the peak frequency.

The significant wave height H_s and peak period T_p are computed for a fully arisen sea assuming the Pierson-Moskowitz spectrum (e.g., Holthuijsen, 2010).

$$H_s = \frac{0.21 u_{19.5}^2}{g} \tag{3.24}$$

$$T_p = \frac{7.14 u_{19.5}}{g} \tag{3.25}$$

Where, $u_{19.5}$ is the wind speed at the reference height, estimated by applying the power law to a reference height of 19.5 m.

Hydrodynamic forces are computed by using strip theory to apply Morison's equation over the submerged length of the hull. The water particle velocity relative to hull motion is $(u - \dot{x})$ and acceleration is $(\dot{u} - \ddot{x})$, where x is the horizontal offset of an individual strip and u and $\dot{u}$ are computed using first order wave theory. The force on each strip is computed as:

$$F_w = \rho C_a V(\dot{u} - \ddot{x}) + \frac{1}{2}\rho C_d A(u - \dot{x})|u - \dot{x}| \tag{3.26}$$

where, ρ is the mass-density of water; $C_a = 1.0$ is the inertia coefficient, and $C_d = 0.6$ is the drag coefficient.

3.3.1.2 OC3 Hywind 5WM Wind Turbine Model

The OC3-Hywind numerical model developed by the National Renewable Energy Laboratory (Jonkman, et al., 2009) is commonly used in academic research and is used throughout the examples.

Rotor, Hub diameter	126 m, 3 m
Hub height	90 m
Wind speed cut-in, rated, cut-out	3 m/s, 11.4 m/s, 25 m/s
Rotor speed cut-in, rated	6.9 rpm, 12.1 rpm
Generator electrical Efficiency	94.4%
Rotor mass	110,000 kg
Nacelle mass	240,000 kg
Tower mass	347,460 kg
Initial CM	85.6 m
Elevation to tower top	87.6 m
Platform diameter above taper	6.5 m
Platform diameter below taper	9.4 m
Platform draft	120 m

Table 3.1: OC3-Hywind 5MW Wind Turbine Parameters for power estimation

The power coefficient k_1 in the torque-controlled region is approximately 0.0034, which is computed as a least-squares fit of the power curve specified with the OC3 model (Jonkman, et al., 2009), using data points at wind speeds of 5 m/s though 11m/s in 1 m/s intervals. The curve fit is excellent over this range, with coefficient of determination $R^2 = 0.9997$.

3.3.1.3 Determination of Coefficients and Parameters

The transformation method relies on three parameters to estimate the expected power and the standard deviation of the power: k_1, k_2 and x. Coefficient k_1 can be extracted from the rising part of the turbulence-free power curve. A single value of k_1 = 0.0034 Ns^2/m^2

has been extracted from the power curve specified with the OC3 model. This value is estimated from the rising part of the curve using a least-squares fit at wind speeds between 5 m/s and 11m/s in 1 m/s intervals. The curve fit is excellent over this range, with coefficient of determination $R^2 = 0.9997$. This value of k_1 for the $\mathrm{OC3} - \mathrm{Hywind}$ is used throughout the examples. A series of k_1 can be extracted from thrust coefficient curve (Figure 3.3 (b)) specified with the Vestas V90 model using $k_1 = 0.25(C_T + C_T\sqrt{1 - C_T})\rho\pi R^2$. The k_1 values of Vestas V90 models are 0.0019, 0.0023, 0.0023, 0.0023, 0.0023, 0.0022, 0.0020, 0.0019, 0.0017, 0.0014, 0.0014 Ns^2/m^2 according to wind speed bars from 5 m/s to 15 m/s with 1 m/s increasement.

Determination of parameters k_2 and *x* requires results from numerical simulation or field measurements. k_2 and *x* are not available for Vestas V90 model because the wind power standard deviation data is not available. Figure 3.2 shows results from direct simulations of two different wind turbine configurations. Both configurations are for the OC3-Hywind rotor and generator assembly: results shown as "Fixed" neglect all motion of the tower; results shown as "Floating" are for the complete floating OC3-Hywind numerical model. The sloping lines on the figure result from linear regression of numerical simulations of various wind speed (21m/s to 25 m/s) and standard deviation (IEC NTM A, B, and C). The slopes of these lines are the coefficient x . The slope are 0.833 for the fixed configuration and 0.863 for the floating configuration. The average and regression values of parameter *x* are found to be 0.795 for the fixed configuration and 0.864 for the floating configuration.

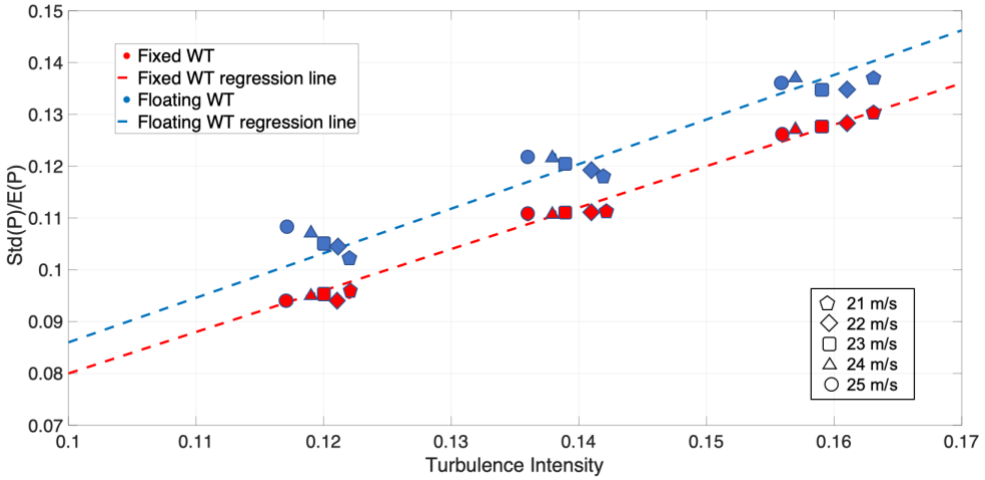

Figure:3.2 Std(P)/E(P) of wind power with Ti of wind speed

3.3.2 Example 1: Forward and Inverse Transformation of Power Curves

The new statistical transformation is shown to be effective at forward transformation from an ideal power curve to a practical power curve, for both the Hywind numerical model and the measured field data for the Vestas field data. The inverse transformation is then used to generate an ideal turbulence-free power curve from realistic simulated wind data. Tower motions are neglected throughout the example.

Realistic wind time-histories are generated using the IEC Class B Turbulence Model, with mean wind speeds varying from 5 to 25 m/s in 1 m/s intervals. Each case shown represents ten 10-minute wind speed samples with turbulence intensities as shown in Table 3.2.

Wind speed (m/s)	5	6	7	8	9	10	11	12	13	14
Turbulence Intensity	0.26	0.24	0.22	0.20	0.19	0.18	0.18	0.17	0.17	0.16
Wind speed (m/s)	15	16	17	18	19	20	21	22	23	24
Turbulence Intensity	0.16	0.15	0.15	0.15	0.15	0.14	0.14	0.14	0.14	0.14

3.2: Comparison of power means for Gaussian model

Figure 3.3 is used to demonstrate the effectiveness of new transformation method. Fig.2a demonstrates application to the OC3-Hywind model subject to IEC NTM turbulence Model B; Fig.2b demonstrates application to the Vestas V90 3MW turbine subject to IEC NTM turbulence Model A. The ideal zero-turbulence power curve on each subfigure is shown as a black dashed line; the practical power curve estimated from the ideal power curve using the new transformation is shown as a red line, and the thrust coefficient is shown as a blue dashed line. The black line on Figure 3.3(a) represents the best estimate of the practical power curve for the OC3-Hywind as computed using direct simulation. The practical power curve computed using the new transformation agrees well with the best estimate of the practical power curve. The black line on Figure 3.3(b) represents the practical power curve computed by direct field measurement. The practical power curve computed using the new transformation agrees well with the practical power curve resulting from direct simulation.

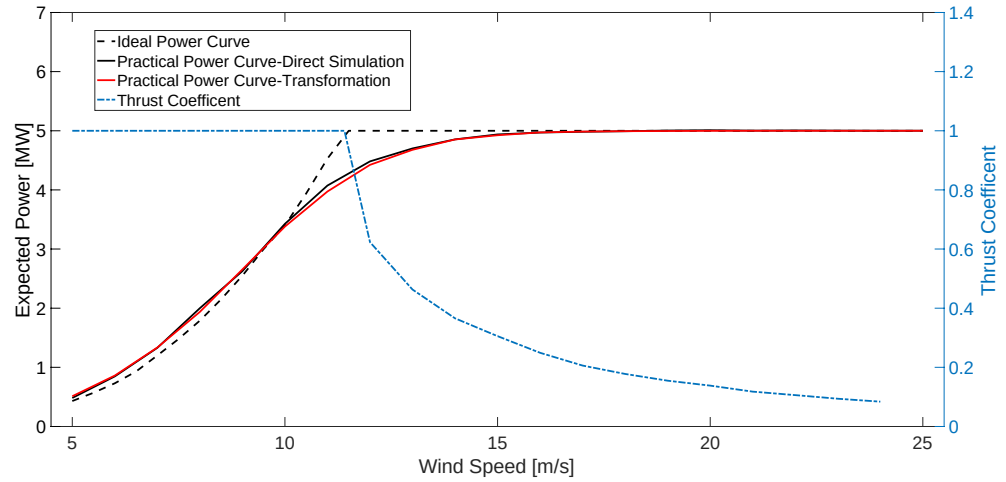

(a) OC3-Hywind 5MW

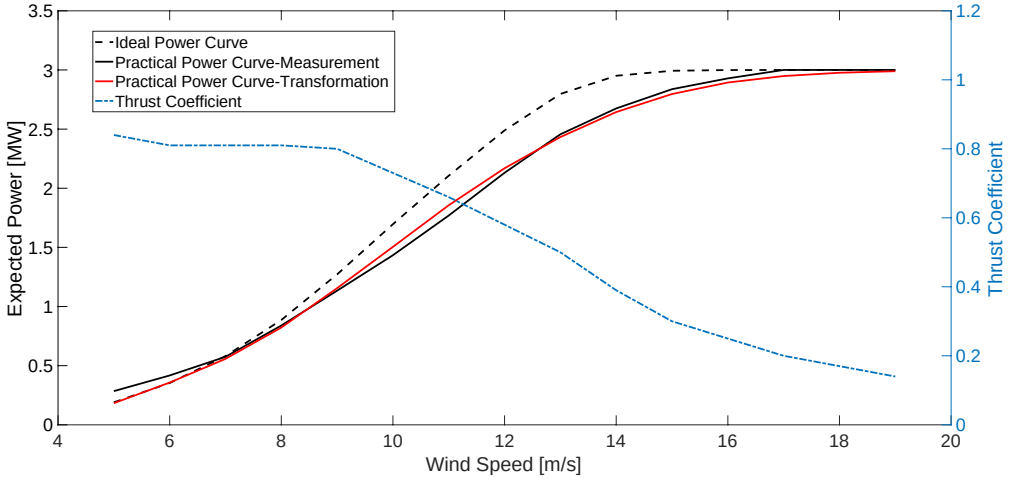

(b) Vestas V90 3MW

Figure 3.3: Effectiveness of the new transformation method

The second part of the example uses the expected power as computed by direct simulation (Figure 3.3(a)) as being equivalent to a measured power output to demonstrate the inverse transformation. Table 3.3 compares values of the $P(u)$resulting from the inverse transformation (Equation 3.22)

using turbulence intensities from Table 3.2 for each bar. The ideal power curve resulting from the inverse transformation is substantially identical to the original power used in the simulations. Small differences are likely to result from the finite duration of simulations, the OC3-Hywind power curve possibly not reflecting the true simulated performance of the OC3 numerical model, and the potential for small errors in scaling the data from the published OC3 figure.

Wind speed [m/s]	5	6	7	8	9	10	11
$E(P)$ [MW]	0.48	0.85	1.33	2.00	2.63	3.43	4.07
Turbulence Intensity	0.26	0.24	0.22	0.20	0.19	0.18	0.18
$P(u)$ [MW] from original power curve	0.39	0.72	1.18	1.77	2.53	3.43	4.55
P(u) [MW] from Transformation	0.34	0.64	1.14	1.80	2.45	3.47	4.77
$k_1{}'$ $[10^{-3}\ Ns^2/m^2]$	2.7	3	3.3	3.5	3.4	3.5	3.6

Table 3.3: Inverse transformation of power curve

Inverting the transformation result has been confirmed to return the average $k_1{}' = 0.0033$ are close to original value of $k_1 = 0.0034$ used in the forward transformation.

3.3.3 Example 2: The Influence of Turbulence Intensity on Power Curves

The new statistical transformation is shown to be effective at predicting the practical power curve and standard deviation of power for three constant values of turbulence intensity by comparing the expected power and the standard deviation of power computed by the new transformation with equivalent values computed by direct simulation. Comparisons are presented for turbulence intensities of 0.1, 0.2, and 0.3, with mean wind speeds varying from 5 to 13 m/s in 1 m/s intervals. Each simulation case represents ten 10-min wind speed realizations.

The transformation method relies on three parameters to estimate the expected power and the standard deviation of the power: k_1, k_2 and x. A single value of k_1 computed directly from the zero-turbulence power curve is used to compute the expected power for all wind speeds and to compute the standard deviation of power for wind speeds below the rated speed. Parameters x and k_2 are needed to compute the standard deviation of power for cases with wind speeds above the rated speed. Determination of x requires results from numerical simulation or field measurements. The single value of x = 1.353 was computed using a single simulation with $\mu = 13$ and $TI = 0.1$, which is then used to represent turbine performance in all conditions. A unique value of k_2 is computed for each wind speed using the specified turbulence intensity and this single value of x.

Figure 3.4 shows that the transformation method effectively predicts the effect of turbulence on the manufacturer's power curve. Expected output power, $E(P)$, is computed by the new transformation (red line) and by direct numerical simulation (black line). The error bars show the

95% confidence interval computed from the standard deviation of the $E(P)$ for each wind condition. The blue dashed line shows the ideal manufacturer's power curve, which represents a zero-turbulence condition.

A formal hypothesis test equivalent to that used in Example 1 is performed to assess the effectiveness of the method. The null hypothesis cannot be rejected for any of the mean wind speeds shown on Figure 3.4, with each passing the Student's *t* test at a significant level of 0.05. The average computed P-value for the Student's *t* test for TI of 0.1, 0.2, and 0.3 are 0.52, 0.77, and 0.79 respectively.

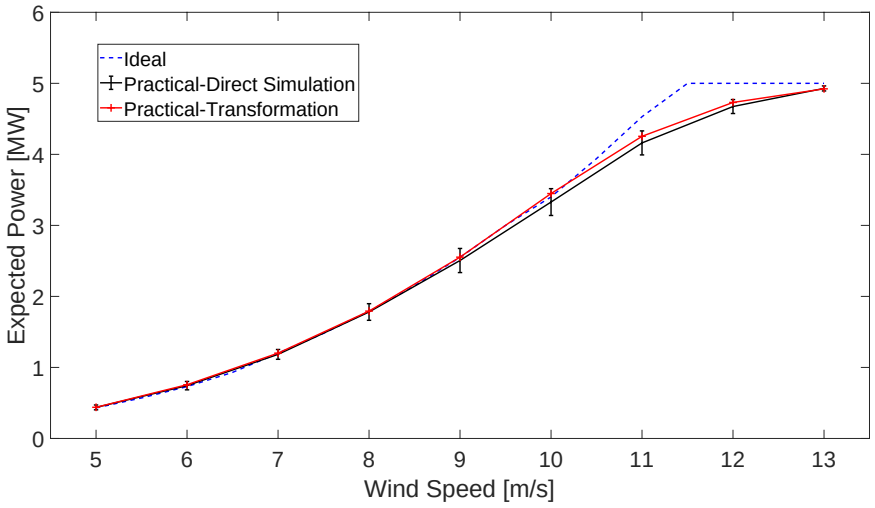

(a) TI=0.1

Figure 3.4: Comparison of expected power for TI of 0.1, 0.2, and 0.3

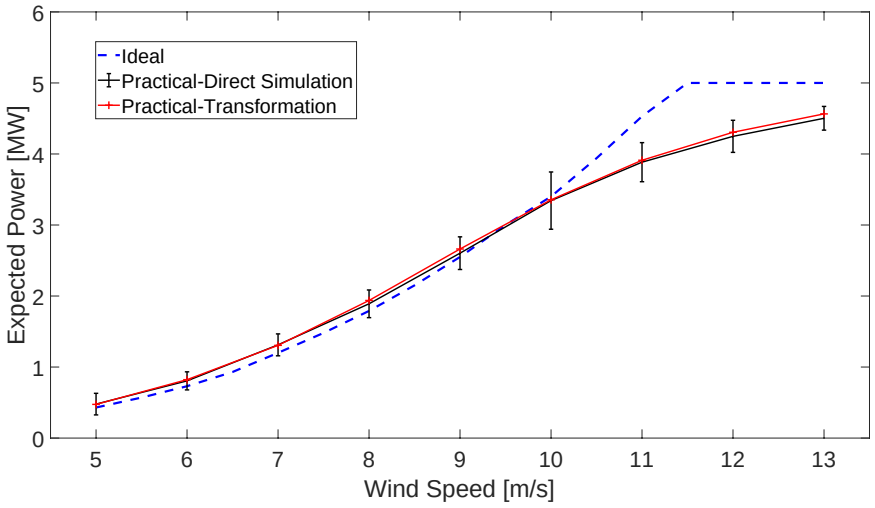

(b) TI=0.2

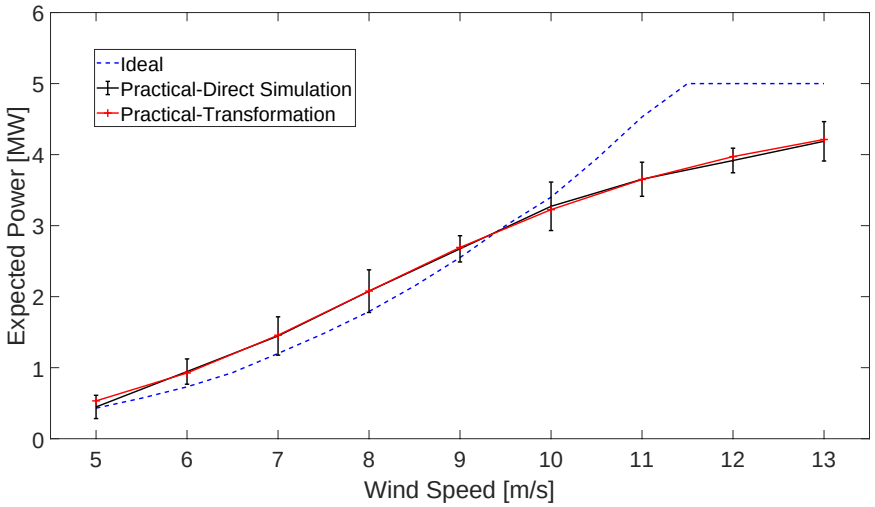

(c) TI=0.3

Figure 3.4 continued.

Figure 3.5 shows that the transformation effectively predicts the effect of turbulence on the standard deviation of power. The red line shows the standard deviation of output power is computed by the new transformation and the black line shows equivalent results computed by

direct numerical simulation. The error bars show the 95% confidence interval computed from the standard deviation of the 10 computed standard deviations of power for each wind condition.

A similar hypothesis test is applied to the standard deviation of the power, $Std(P)$. The mean and standard deviation of $Std(P)$ are represented by the mean and standard deviation of 10 values of $Std(P)$ resulting from direct simulation. The null hypothesis is rejected at the 5% level for only one of the 27 cases shown on Figure 3.4 ($TI = 0.1, \mu = 12$, P-value = 0.04). The average of the 9 P-values computed for each TI are 0.39, 0.79, and 0.54.

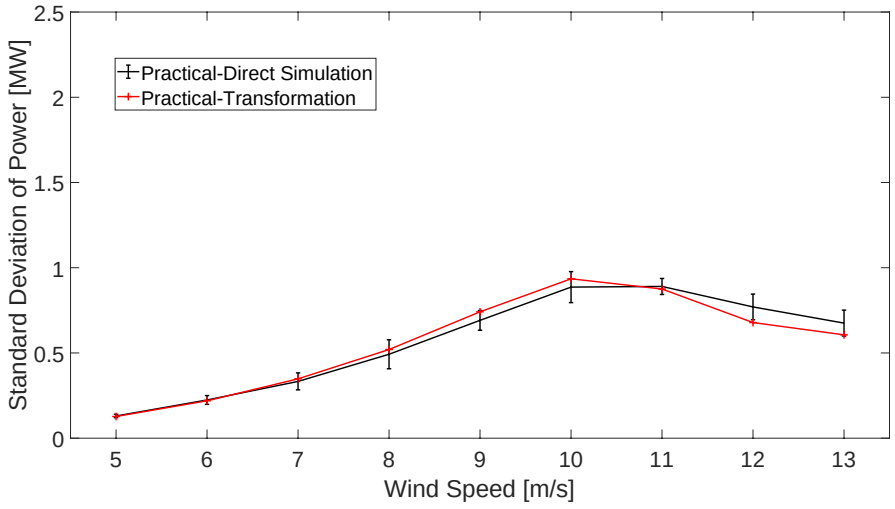

(a) TI=0.1

Figure 3.5: Comparison of standard deviation of power for TI of 0.1, 0.2, and 0.3

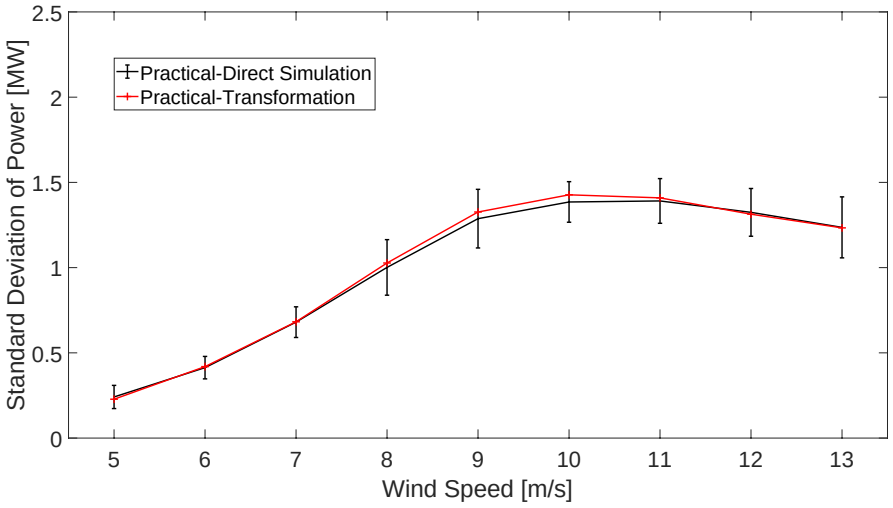

(b) TI=0.2

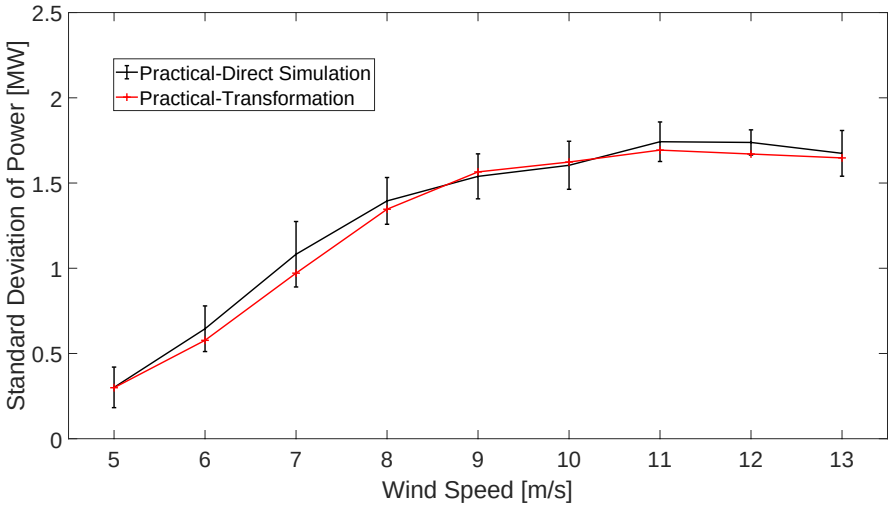

(c) TI=0.3

Figure 3.5 continued.

3.3.4 Example 3: The Influence of Non-Gaussian Winds

Wind processes are commonly assumed to be Gaussian, but field measurements indicate natural winds are a weakly non-Gaussian process. This example first shows the relative importance of non-Gaussian winds on expected power and then goes on to quantify the cumulative annualized effect. The skewness and kurtosis of wind time-histories are not broadly available, so wind data measured at a single near-shore location and shown in Table 3.4 are assumed to be representative (Dai and Sweetman, 2020).

Wind speed (m/s)	4	5	6	7	8	9	10	11	12	13
Skewness α_3	0.33	0.45	0.65	0.81	0.80	0.61	0.33	0.07	-0.24	-0.42
Kurtosis α_4	2.87	3.19	3.59	3.75	3.39	2.77	2.29	2.08	2.11	2.19

Table 3.4: Skewness and kurtosis of measured nearshore winds

The Hermite moment model is used in this example to transform the cut-in, rated, and cut-out speeds of the real non-Gaussian wind process to equivalent values having the same fractile in a Gaussian process. A non-Gaussian softening process having $\alpha_4 \geq \alpha_3^2 + 1$ u' can be computed from a Gaussian process u using the Hermite polynomial (Winterstein,1988):

$$u' = H(u) = \kappa[u + h_3(u^2 - 1) + h_4(u^3 - 3u)] \tag{3.27}$$

The means and standard deviations of regions 1 and 2 of the Gaussian distribution resulting from the transformation are then computed using Equations 3.1 and 3.2. These Gaussian values of mean and standard deviation are then transformed back to the real non-Gaussian process using the inverse Hermite transformation of a hardening response process:

$$u = H^{-1}(u') = u' - h_3\left(u'^2 - 1\right) - h_4\left(u'^3 - 3u'\right) \tag{3.28}$$

where $h_3 = \alpha_3/6$, $h_4 = \frac{\alpha_4 - 3}{24}$ are computed from the values in Table 3.4, and $\kappa = (1 + 2h_3^2 + 6h_4^2)^{-1/2}$ is a scale factor that ensures u' has unit variance.

Figure 3.6 shows the effect of including non-Gaussian effects on each of the wind speeds in Example 2. The Gaussian transformation results shown as the blue bars are the same as in Figure 3.4 with TI = 0.2. The results show that the non-Gaussian model predicts greater power than the Gaussian for positive skewness and kurtosis greater than three, and the Gaussian predicts greater power for negative skewness and kurtosis less than three. Cases with relatively greater gusts have disproportionately higher power because of the nonlinear relationship between wind speed and power, and relatively greater gusts are associated with higher values of skewness and kurtoses.

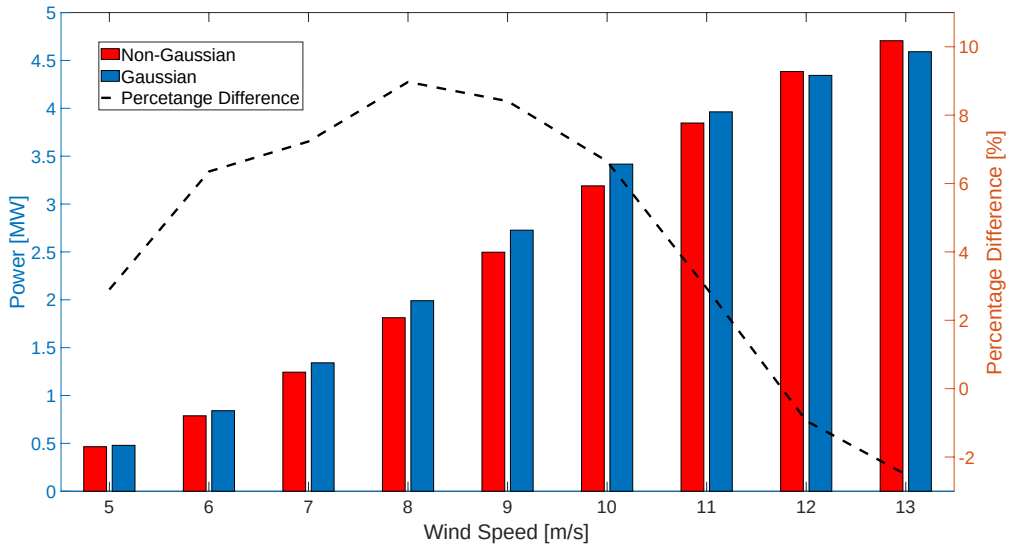

Figure 3.6: Comparison of expected power for Gaussian and non-Gaussian models

Figure 3.6 appears to indicate that the difference between the Gaussian and non-Gaussian models are relatively small and non-systematic, but these results can be important when summed over an entire year.

3.3.5 Example 4: The Estimation of AEP

The annualized effect is demonstrated by computing the expected AEP for a single location 300 miles northeast of Honolulu, Hawaii, which is National Oceanic and Atmospheric Administration (NOAA) buoy Station 51000. Figure 3.7 shows power curve of OC3-Hywind turbine and a histogram of measured 10-minute mean wind speeds for one year beginning January 1, 2018; the annual mean wind speed for 2018 is 9.71 m/s, slightly below the rated speed for OC3 Hywind.

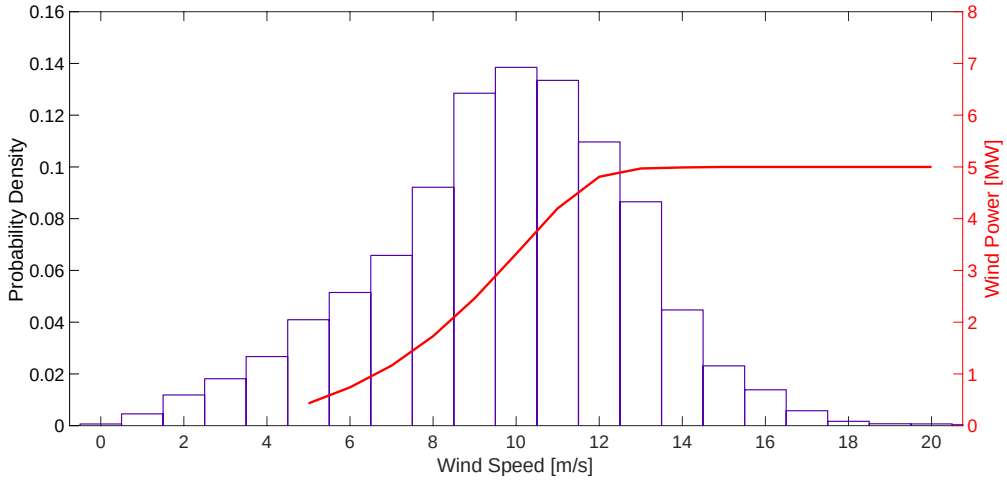

Figure 3.7: Histogram of annual 10-min average wind speeds (NOAA station 51000) and power curve of OC3-Hywind model

Additional wind properties were applied to the measured NOAA buoy data. The incoming wind speed at hub height is computed using the power law with exponent $P = 0.11$ (Hsu, et al, 1994). The turbulence intensity is assigned decimal values of 0.0, 0.1 and 0.2 to compute the standard deviation for three distinct cases, and the higher moments are taken from Table 3.5.

The total AEP is computed as the annual sum of the expected energy for each of the measured 10-minute mean wind speeds, equivalent to the International Electrotechnical Commission (IEC) standard (IEC, 2005),

Table 3.5 shows the annual energy production estimated for assumed turbulence intensities and assuming the wind to be a Gaussian vs a non-Gaussian process. The results show that application of higher moments to compute the AEP shows the Gaussian model consistently over-predicts the non-Gaussian model. The percentage difference between non-Gaussian model and Gaussian model increases with increasing turbulence intensity, with percentage difference around 2% at TI = 0.2.

Turbulence intensity	0	0.1	0.2
Gaussian AEP (GW)	27.40	26.91	25.89
Change AEP due to TI (GW)	N/A	-0.49	-1.51
Percentage Difference (%)	N/A	-1.79	-5.51
Non-Gaussian AEP (GW)	27.40	26.64	25.56
Change in AEP due to α_3 and α_4	N/A	-0.27	-0.33
Percentage Difference (%)	N/A	-1.00	-1.27

Table 3.5: Effect of statistical moments on AEP

The AEP is calculated based on energy output of single OC3-Hwyind wind turbine with different turbulence intensity using $AEP = \sum_{i=1}^{n} P(u_i)\, L(u_i)\, T$ where $P(u_i)$ is the power for wind speed bar u_i, $L(u_i)$ is the probability for wind speed bar u_i , and one-year time T.

Figure 3.8 shows histogram of annual measured 10-minute mean wind speeds and the estimated AEP per each wind speed bar. The APE is calculated based on simulation results and percentage of wind speed bar of raw data.

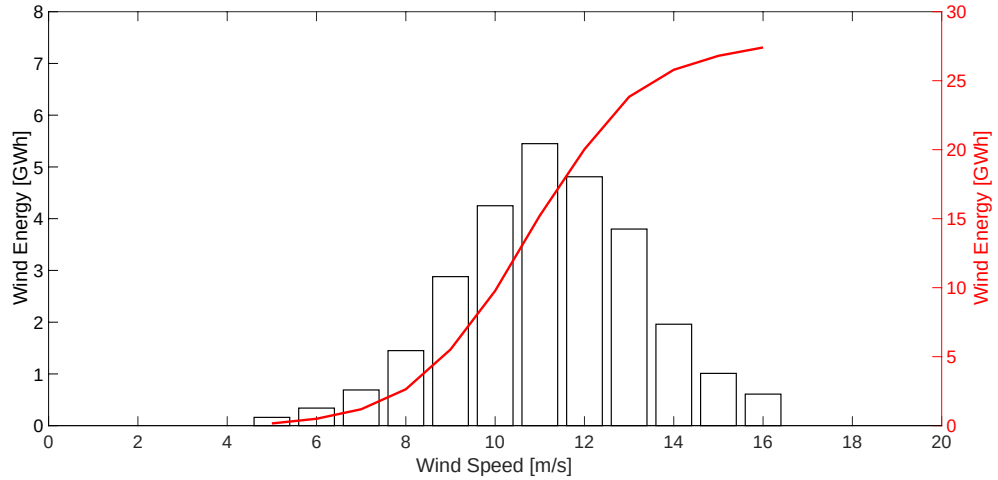

Figure: 3.8 AEP per wind speed bar and cumulative of AEP

Probability $L(u_i)$ can also be calculated using Eqaution3.29 according to the three parameters Weibull distribution.

$$L(u_i) = L(u_i, \lambda, k, c) = F_w(u_i, \lambda, k, c) - F_w(u_{i-1}, \lambda, k, c) \tag{3.29}$$

where λ is the scale parameter, k is the shape parameter, and c is location parameter.

Table 3.6 shows the AEP estimated by four different methods: Transformation Direct, Transformation Weibull, Simulation Direct, and Simulation Weibull. The Transformation Direct method and Transformation Weibull method use proposed method to estimate $P(u_i)$, and use raw data or Weibull distribution to estimate $L(u_i)$. Similarly, the Simulation Direct method and Simulation Weibull method use numerical simulation via Loose to estimate $P(u_i)$, and use raw data or Weibull distribution to estimate $L(u_i)$. Annual 10-min average wind speeds (NOAA station

51000) is fitted by Weibull distribution with scale parameter $\lambda = 6.9022$, shape parameter $k = 2.577$, and location parameter c=4.126.

Turbulence intensity	0	0.1	0.2
Transformation Direct	27.40	26.91	25.89
Transformation Weibull	26.65	25.88	25.04
Simulation Direct	27.46	25.98	25.20
Simulation Weibull	27.13	25.76	25.06

Table 3.6: AEP (GWh) estimation by different method

The results in Table 3.6 shows that the proposed method is same accuracy with numerical simulation for AEP estimation, but more convenience to use. AEP estimated by Weibull distribution is smaller than raw data, but it would be also useful when the long-term wind speed data is not available.

3.4 Conclusion

A new method is developed to transform between a manufacturer's power curve and a practical power curve using both turbulence intensity and higher moments. The transformation is based on replacing a single mean wind speed with a mean and a distribution about that mean. Random process theory is used to derive equations that combine the wind distribution with the manufacturer's power curve. Any mean wind speed generally has some contribution from each

region of the power curve; the total power for each mean wind speed is computed as the sum of the contributions of expected power from each region.

The new method is shown to be effective at predicting the reduction in the power curve associated with high turbulence intensities. Verification is by comparison of energy predicted using direct simulation with equivalent predictions based on the new transformation. Results of an example show that application of a Gaussian-only wind model can overestimate AEP, but the non-Gaussian effects are significantly less than the influence of turbulence intensity. These results show that the statistical moments of the wind process are necessary to accurately predict energy production; these moments generally require high-fidelity wind measurements at the proposed wind farm project location.

The new method can be used to substantially reduce the lengthy direct simulation process that is commonly used to predict AEP as part of early project feasibility studies, and can be used to extract ideal turbulence-free power curves from measured field data from operating wind turbines.

4. IMPACT OF NON-GAUSSIAN WINDS ON BLADE FATIGUE LIFE OF FLOATING OFFSHORE WIND TURBINES

4.1 Introduction and Background

Floating offshore wind turbines (FOWTs), which are deployed in the natural ocean environment, work under a significant number of cyclic external loads. A typical wind turbine, during its 20-yr lifetime, may experience more than 10^8 cyclic loads, with an approximately 30-rpm rotation speed and 4,000-hr operation time per year (Manwell, et al, 2010). Capital expenditures for offshore wind developments are typically 1.5 to 2 times more than those for onshore developments (Watson, et al., 2005), and maintenance costs are likely to be 5 to 10 times higher than those for onshore (Van Bussel, & Zaaijer, 2001, March). Therefore, accurate estimation of fatigue damage is critically important in the offshore wind industry.

Fatigue damage of FOWTs is the process in which an accumulation of damages is caused by a repeating environmental load of variable magnitude applied on FOWT structures. Once sufficient damage is accumulated, fatigue fracture will initiate and propagate through the plasticized regions. Fatigue damage calculations and fatigue life predictions of offshore wind turbines are quite complicated.

Fatigue life of a medium-scale, horizontal-axis wind turbine system has been estimated using the well-known S-N damage equation, with load spectrum confirmed with at least 20 to 30 yr of operating life (Kong, et al, 2006). Reliability-based calibration of a design code for wind-turbine

rotor blades has been developed considering flapwise-bending fatigue failure (Ronold, et al, 2001). Hu used a 10-min mean wind speed and 10-min turbulence intensity based on long-term wind-speed distribution to simulate a random wind field and analyze the fatigue reliability of composite wind-turbine blades considering wind-load uncertainty (Hu, et al, 2012). A stochastic approach has been employed to develop a computer code in order to simulate wind flow with randomness in its nature on the blade, with, subsequently, each load case being weighted by its rate of occurrence using Weibull wind-speed distribution (Shokrieh and Rafiee, 2006).

Analysis of field measurement data of wind speed has found a different conclusion that natural short-term wind is not Gaussian distribution (Dai and Sweetman, 2020). Non-Gaussian wind-inflow velocities to offshore wind turbines could potentially affect predicted power, load, torque, and blade fatigue life. This increased quantity of extreme events will cause alternating loads on the airfoil and on the main shaft in the form of torque fluctuations, which may cause additional fatigue damage (Mücke, et al., 2011). Schottler et al. (2017) simulated non-Gaussian and Gaussian wind inflow conditions in a wind tunnel and indicated that extreme loads in non-Gaussian wind inflow conditions occur much more frequently than those predicted by a typical Gaussian wind model. Gong and Chen (2017) investigated the extreme response of operational and parked wind turbines in non-Gaussian wind conditions. Obviously more extreme blade-root-edgewise responses and tower-fore-aft bending moments have been found for operational wind turbines in non-Gaussian wind inflows. Similar results of blade-root-flapwise-bending moments have been found for parked wind turbines.

This dissertation proposes a detailed methodology to evaluate the fatigue damage of FOWT blades including short-term numerical simulation and long-term wind-speed distribution. This dissertation also compares blade fatigue damage with the wind conditions of both Gaussian and non-Gaussian wind turbulence models. Short-term numerical simulations with different wind conditions were conducted by the in-house numerical simulation code Loose with a nonlinear beam blade solver (Tang and Sweetman, 2019). Non-Gaussian random wind fields were transformed from the corresponding Gaussian random wind fields by an in-house numerical code based on the Hermite moment model (Winterstein, 1988; Sweetman and Choi, 2010).

Long-term wind speed distribution was investigated in order to identify the "hot spot" for fatigue analysis. Several distribution models were examined to fit two groups of long-term wind speed data from the buoy records of the National Oceanic and Atmospheric Administration (NOAA). The best-fitting distribution was then used to determine the probability of duration for FOWT operation at each mean wind-speed bar from cut-in speed to cut-out speed. Numerical simulations within each wind-speed bar calculated the wind load applied on the blades. Corresponding fatigue damage on the nodes distributed on the shell of blades was also identified. Fatigue damage matrices, including the damage values of every single node within each wind-speed bar, were then combined with long-term wind-speed distribution to figure out the annual total fatigue damage expectation on each node. The node of maximum fatigue damage value was identified as the hot spot on the blades where fatigue crack is highly possible to occur. Annual fatigue damage expectation on the hot spot was then used to predict the fatigue life of blades based on the Palmgren-Miner linear damage hypothesis. A flowchart of blade fatigue life estimation is shown in Figure 4.1.

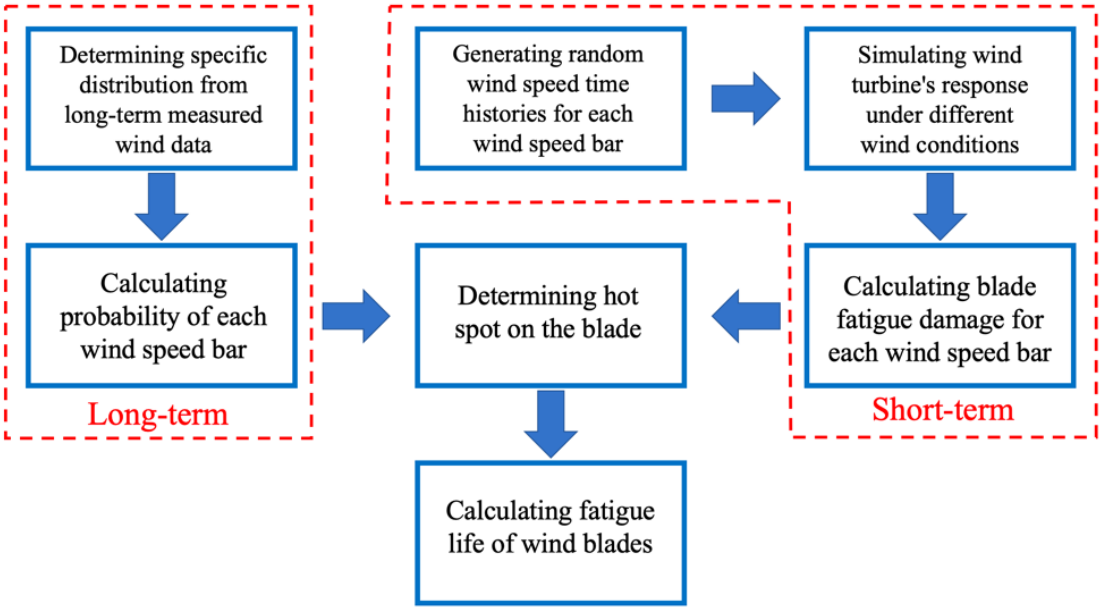

Figure 4.1: Flowchart of blade fatigue life estimation

The remaining portion of this chapter includes three sections. Section 2 explains the theory of random short-term wind simulation and the transformation method between Gaussian and non-Gaussian wind processes. Additionally, long-term wind-speed distribution is discussed using NOAA buoy data. Aerodynamic wind load of blades during the short-term period and fatigue damage hot-spot identification based on the long-term period are also discussed. A case study including various design load cases (DLCs) is presented to demonstrate this new fatigue analysis method using a 5-MW National Renewable Energy Laboratory (NREL) wind turbine blade. The results of root-bending moment and blade fatigue damage are listed in Section 4. Finally, the discussion and conclusion are given in Section 5.

4.2 Theory

4.2.1 Simulation of Random Wind Conditions

Random wind conditions are simulated with a 10-min mean wind speed and turbulence intensity at the hub height of the wind turbine. Wind-speed data are generated by TurbSim, an NREL research software. Opposite from a physics-based model, TurbSim uses a statistical model to create three-dimensional wind-speed time series numerically. Different wind-speed time series are simulated at grid points of a two-dimensional vertical rectangular grid perpendicular to the incoming wind. (Jonkman and Buhl, 2012).

The 10-min mean wind-speed data from the NOAA buoy database were measured by the wind-speed anemometer on the buoy. The anemometer is installed on the top of the buoy, which is approximately 4 m above sea level. The incoming wind speed u_2 at the hub height of the wind turbine is estimated based on wind speed u_1 at anemometer height using the power law: $u_2 = u_1 \left(\frac{z_2}{z_1} \right)^P$ (Hsu, Meindl, and Gilhousen, 1994), where u_2 is the wind speed at the hub height of the wind turbine, and z_2 and u_1 are the wind speed measured at height z_1, which is the height at which the anemometer is installed on the buoy.

Turbulence intensity is defined as the ratio of standard deviation of wind speed to corresponding mean of wind speed, as shown in Equation 4.1:

$$TI = \frac{\sigma_u}{\mu_u} \tag{4.1}$$

Dynamic turbulence intensities of different turbulence models are available in TurbSim. Recommendation of turbulence intensity values are subject to the different DLCs defined in International Electrotechnical Commission (IEC) regulations. The IEC normal turbulence model (NTM) is the most common turbulence model, as shown in Equation 4.2:

$$\sigma = I_{ref}(0.75\mu + 3.8) + I_{ref}(0\mu + 1.4) \ , \tag{4.2}$$

where μ is the mean of the true wind speed, and I_{ref} is the expected value of hub-height turbulence intensity at a 10-min average wind speed of 15 m/s. IEC gives values for I_{ref} of 0.16, 0.14, and 0.12 for NTM classes A, B, and C, respectively.

Wind time histories are commonly simulated from wind-power spectra using techniques that conform to the central limit theorem such that the simulated wind speeds conform to a Gaussian distribution. The corresponding non-Gaussian wind-speed data were transferred using the Hermite moment model, which transfers data between Gaussian and non-Gaussian wind processes (Winterstein, 1988; Sweetman and Choi, 2010).

An original wind-speed field file created by TurbSim recorded the time history of wind-speed data including horizontal wind velocity, u_h , horizontal angle, φ, and vertical wind velocity, u_z. The two velocity components are combined into the total velocity vector, $\vec{u}$, with vertical angle θ using Equations 4.3 and 4.4:

$$| \vec{u} | = \sqrt{u_h^2 + u_z^2} \tag{4.3}$$

$$\theta = \arctan\left(\frac{u_z}{u_h}\right) \tag{4.4}$$

The total velocity, $\vec{u}$, from TurbSim wind-field file satisfied Gaussian distribution. Hermite moment model transformation $\mathcal{H}$ was then used to convert the modulus of total velocity, u, to its non-Gaussian corresponding vector, $\overrightarrow{u'}$:

$$\left| \overrightarrow{u'} \right| = \mathcal{H}(| \vec{u} |) = \kappa \left[| \vec{u} | + h_3(| \vec{u} |^2 - 1) + h_4(| \vec{u} |^3 - 3| \vec{u} |) \right] \quad , \tag{4.5}$$

where κ is a scale factor, and coefficients $h_3 = \alpha_3/6$ and $h_4 = (\alpha_4 - 3)/24$ are directly calculated from the given skewness and kurtosis of the non-Gaussian model.

Non-Gaussian wind-velocity components u_h' and u_z' are calculated using the modulus of non-Gaussian total wind-velocity vector $\overrightarrow{u'}$ and vertical angle θ as $u_h' = \left| \overrightarrow{u'} \right| \sin\theta$ and $u_z' = \left| \overrightarrow{u'} \right| \cos\theta$. The procedure of non-Gaussian random wind simulation is shown in Figure 4.2.

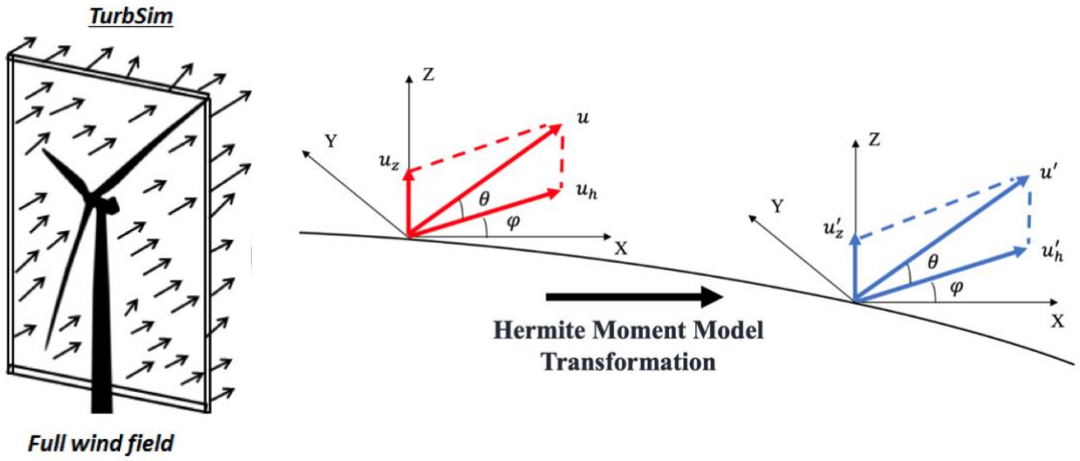

Figure 4.2: Transformation of non-Gaussian wind field

The same procedures are applied on all the speed data in the original input files so that the original Gaussian wind field is transferred to the non-Gaussian wind field. Typical wind-speed time history generated by TurbSim and its corresponding non-Gaussian wind-speed time history are shown in Figure 4.3.

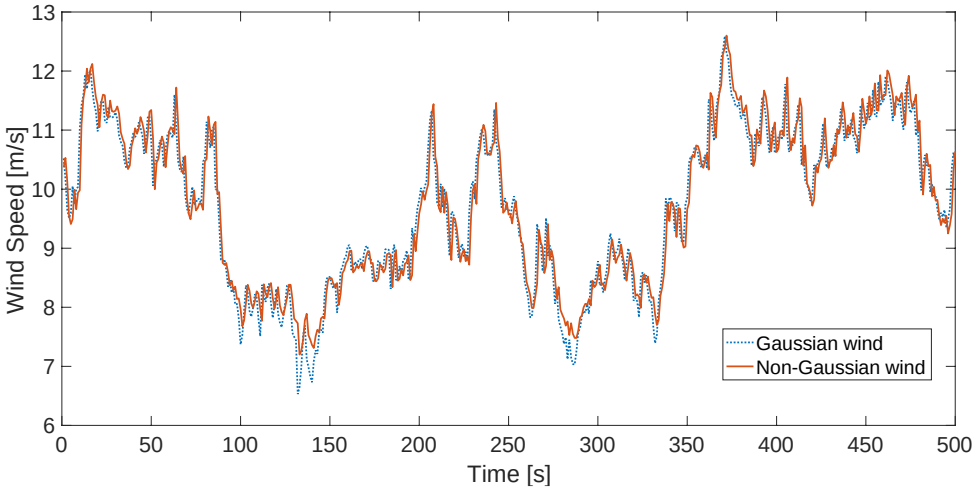

Figure 4.3: Typical wind-speed time history of Gaussian and non-Gaussian wind

4.2.2 Fatigue Damage Estimation of the Blades

Two common assumptions of blade structure are applied in this section. The first one is the isotropic beam assumption, in which deformations only happen in the longitudinal direction. The second assumption is that torsional deflection is neglected because of very high torsional stiffness. Transverse and shear stresses can be ignored under such simplification. The combined stresses can be calculated from normal stresses alone. The influence of transverse and shear stresses in off-axis loading of glass fiber composites can be found in other studies.

The normal strain at a point (y, x) at a cross-sectional area is given by the simple beam theory:

$$\varepsilon_x(y,x) = -\frac{M_1}{EI_1}x + \frac{M_2}{EI_2}y + \frac{N}{EA} \quad , \tag{4.6}$$

where M_1 and M_2 are the bending moments of local principle axes, N is the axial force, E is Young's modulus, and EI_1, EI_2, and EA are the stiffnesses of the axes.

Blade fatigue analysis based on normal strain and principle strain are investigated, and the results indicate that fatigue damage estimated based on principle strain is more accurate (Gao and Sweetman, 2019). For the strain tensor, the eigenvalues represent principal strains ε_P, and eigenvectors represent principal axes $\vec{n}$:

$$E\,\vec{n} = \varepsilon_P\,\vec{n} \quad , \tag{4.7}$$

where strain tensor $E = \begin{bmatrix} \varepsilon_{11} & \varepsilon_{12} & \varepsilon_{13} \\ \varepsilon_{21} & \varepsilon_{22} & \varepsilon_{23} \\ \varepsilon_{31} & \varepsilon_{32} & \varepsilon_{33} \end{bmatrix}$, and $\vec{n}$ is principal axes.

The blade fatigue damage caused by random wind load can be estimated by the rainflow cycle–counting method and the cumulative damage model. Rainflow cycle counting is performed on the time history of principle strain ε_P using a code implemented in MATLAB. This algorithm is based on ASTM International standards (ASTM, 2011).

The number of cycles is solved by rainflow using the strain time histories of a single numerical simulation with time T_s at a given wind speed. These results are arranged with mean strain ε_m and strain amplitude ε_a being stored in matrix $M_{i,j}$. This matrix is then converted to annul cycle matrix $N_{i,j}$ by multiplying the factor corresponding to 1 yr.

$$N_{i,j} = \frac{M_{i,j}}{T_s} \, (60 \cdot 60 \cdot 24 \cdot 365) \tag{4.8}$$

The hypothesis that fatigue damage accumulates linearly and independently for each cycle is widely accepted. The annual total damage of a single node on the shell of a blade can be estimated according to Miner's rule (Nijssen, R. P. L., 2006):

$$d = \sum_{i,j} \frac{N_{i,j}}{N_{f,ij}} \quad , \tag{4.9}$$

where $N_{f,ij}$ is a matrix with a number of cycles when failure occurs of the unique mean strain ε_m and strain amplitude ε_a are appropriate to $N_{i,j}$.

4.2.3 Long-Term Wind Speed Distribution Using Buoy Data

The process of identifying the location of fatigue hot spot for an entire operation period is based on fatigue load estimation. The portion of each fatigue load component is determined by the distribution of wind speed. A virtual 5-MW offshore wind turbine is assumed to be deployed at two potential offshore wind-farm locations.

The first case is based on meteorological wind-speed data from NOAA Station 44065, which is in the New York harbor 30 mi southwest of Manhattan. The second case is based on meteorology wind-speed data from NOAA Station 46006, which is 600 mi west of the California coast. These two locations are selected from a pool of NOAA stations based on the principle of annual mean wind appropriating a 5-MW offshore wind turbine.

Weibull distribution is well-known to be used for the statistical analysis of long-term wind speed data (Shu, et al, 2014) and used on two NOAA buoy locations, are shown in Figure 4.4.

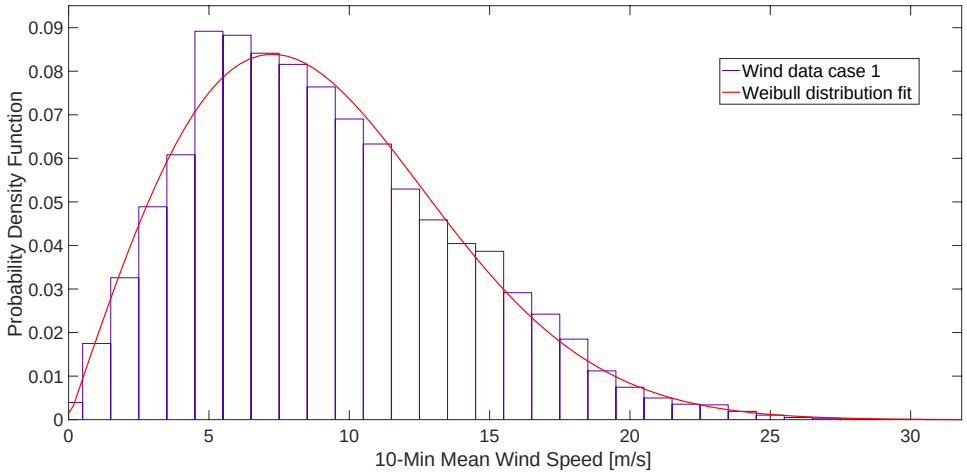

(a) Case 1 at NOAA Station 44065

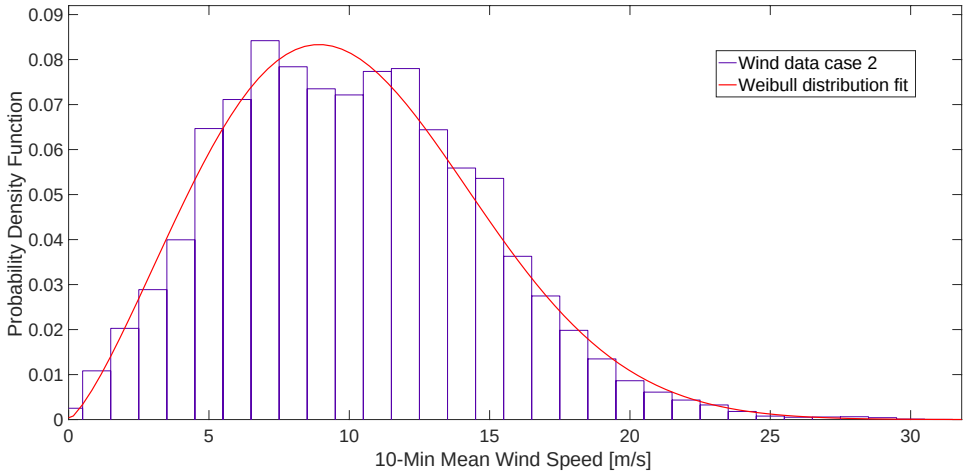

(b) Case 2 at NOAA Station 46006

Figure 4.4: Distribution fitting of 10-min mean wind speed

Figure 4.4 includes one-year wind- speed histograms and their corresponding Weibull distribution plots of two cases. According to the log likehood values given by distribution fitting toolbox, Weibull distribution is the best fit for annual 10-min mean wind-speed data. The probability density function of Weibull distribution is given in Equation 4.10 (Burton, etc., 2001):

$$f_w(u) = \frac{k}{\lambda}\left(\frac{u}{\lambda}\right)^{k-1} e^{-\left(\frac{u}{\lambda}\right)^k} \tag{4.10}$$

The cumulative distribution function of Weibull distribution is given in Equation 4.11:

$$F_w(u) = 1 - e^{-\left(\frac{u}{\lambda}\right)^k} \quad , \tag{4.11}$$

where scale parameter λ and shape parameter k given by the distribution-fitting toolbox of Matlab are shown in Table 4.1.

Parameters	$\boldsymbol{\lambda}$	$\boldsymbol{k}$
Case1	10.24	2.00
Case2	11.40	2.31

Table 4.1: Parameters of Weibull distribution for each case

4.2.4 Fatigue Hot-Spot Identification and Fatigue Life Calculation

Hot spots identified by the material failure theory are different during different wind conditions. Turbine faults, startups, shutdowns, and parked conditions are not considered in this work. According to fatigue DLC1.2 of IEC 61400-3, wind-speed conditions are divided into 11 bins from a 3-m/s cut-in speed to a 25-m/s cut-out speed. The critical wind-speed zone of fatigue damage

was within 11 bins. The probabilities of each wind-speed bin based on historical data from two buoys are listed in Table 4.2.

Wind speed (m/s)		**4-5**	**6-7**	**8-9**	**10-11**	**12-13**	**14-15**
Probability $\boldsymbol{P_i}$	Case1	0.149	0.167	0.158	0.132	0.099	0.067
	Case2	0.118	0.154	0.166	0.153	0.124	0.089
Wind speed (m/s)		**16-17**	**18-19**	**20-21**	**22-23**	**24-25**	
Probability $\boldsymbol{P_i}$	Case1	0.042	0.024	0.012	0.005	0.003	
	Case2	0.055	0.031	0.015	0.007	0.003	

Table 4.2: Probabilities of wind-speed bars

One-year fatigue damages of nodes on blade shells are calculated based on the strain and stress at each node. These results are shown in damage matrix $\boldsymbol{D_i}$, an 80×23 matrix representing 23 cross-sections along the blade and 80 nodes on the boundary of each cross-section, as shown in Figure 4.5.

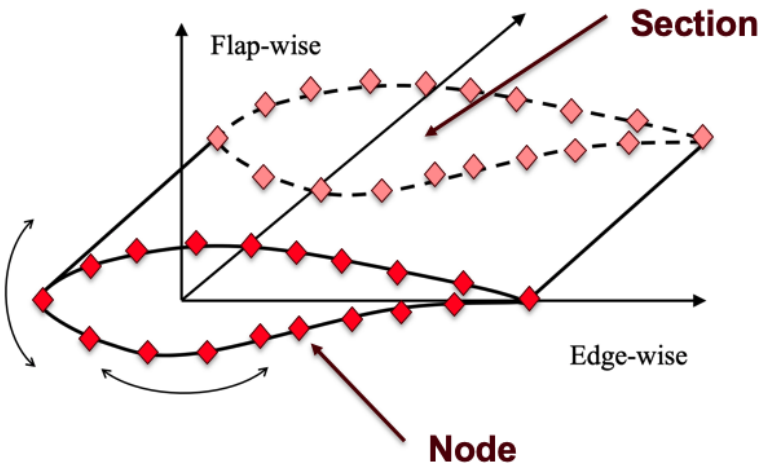

Figure 4.5: Nodes on blade sections

Combining the probabilities and damage matrix of each bin, the expectation matrix of blade fatigue damage during the whole operating period is calculated using Equation 4.12:

$$[\boldsymbol{D_E}]_{80\times23} = \sum_{i=1}^{n} P_i \, [\boldsymbol{D_i}]_{80\times23} \quad , \tag{4.12}$$

where $\boldsymbol{D_E}$ is the damage expectation matrix, P_i is the probability of each wind-speed bar, and $\boldsymbol{D_i}$ is the damage matrix of each wind-speed bar.

The node of maximum value in the expectation matrix of fatigue damage $\boldsymbol{D_E}$ was identified as the hot spot on the blades where fatigue crack is highly possible to occur.

$$d_{hot-spot} = \max \begin{bmatrix} d_{1,1} & \cdots & d_{1,23} \\ \vdots & \ddots & \vdots \\ d_{80,1} & \cdots & d_{80,23} \end{bmatrix}_E \tag{4.13}$$

Fatigue life prediction depends on the fatigue damage of most critical blade locations. The Palmgren-Miner linear damage hypothesis indicates that failure occurs at the location of the hot spot when cumulative fatigue damage D equals 1 (Miner, 1945):

$$D = \sum_{i=1}^{m} d_{hot-spot} = 1 \quad , \tag{4.14}$$

where d_i is the annual fatigue damage at the hot spot, and m is the number of years until blade failure occurs.

The annual fatigue damages of blades are assumed to be the same during the entire FOWT operational life, such that the fatigue life of wind blades is calculated based on the fatigue damages of the hot spots on the blades using Equation 4.15. The fatigue life defined in this chapter is the time when the first crack is generated, not the time at which the whole structure fails.

$$T_Y = \frac{1}{d_{hot-spot}} \tag{4.15}$$

4.3 Case Study

4.3.1 Numerical Modeling

A case study is presented to demonstrate the method proposed using a 5-MW NREL wind-turbine model and its blade. This case study includes two series of DLCs: DLC 1.x with a Gaussian wind process and DLC 2.x with a non-Gaussian wind process. Each DLC series includes 11 wind-speed bars, which represent the whole wind-speed range of the wind turbine. The operational wind speed lasts from 3 to 25 m/s, which are the mean wind speeds of hub-height incoming wind speeds toward the blade swipe area.

NTM is chosen for the wind simulation. This model consists of full-field, three-component stochastic winds and a wind profile with a vertical power law shear exponent of 0.14. Wind time histories used in these simulations are created using TurbSim. Turbulence intensity is set to be constant in each DLC based on field measurement data.

A normal sea-state model is chosen for the wave simulation. Random and irregular sea states are modeled as a summation of sinusoidal wave components based on air wave theory. The amplitudes of wave components are determined by the Joint North Sea Wave Observation Project (JONSWAP) spectrum (Hasselmann, et al., 1973).

$$S(w) = \alpha \frac{g^2}{\omega^5} e^{-\frac{5}{4}\left(\frac{\omega}{\omega_P}\right)^{-4}} \gamma^{e^{-0.5\left(\frac{\omega-\omega_P}{\sigma\omega_P}\right)^2}} \quad , \qquad (4.16)$$

where $\alpha = 5.061\left(\frac{\omega_P}{2\pi}\right)^4 H_s^2(1 - 0.287\log\gamma)$, peak enhance coefficient γ is 3.3, H_s is significant wave height, ω_P is peak frequency, and $\omega_P = \frac{1}{T_p}$.

The significant wave height and peak spectral period for both Gaussian and non-Gaussian model DLCs are calculated using Equation 4.17 and 4.18 based on the assumption of a fully developed sea state (Holthuijsen, 2010):

$$H_s = \frac{0.21u_{19.5}^2}{g} \quad , \tag{4.17}$$

$$T_p = \frac{7.14u_{19.5}}{g} \quad , \tag{4.18}$$

where $u_{19.5}$ is the wind speed at a reference height of 19.5 m and is estimated by the power law based on hub-height wind speed.

Wind forces are computed using the NREL subroutine AeroDyn (Jonkman, 2013), which uses blade-element theory to compute forces on the moving blades directly from a time history of the wind. A built-in blade pitch controller in the time domain simulator responds to the rotor speed and adjusts the pitch angle of each blade in order to maintain steady power output (Blake and Sweetman, 2014).

Wave forces are computed using the well-known Morison equation, modified to include motion of the hull through the water:

$$F_w = \rho C_m V \dot{u} + \frac{1}{2} \rho C_d A u|u| \ , \tag{4.19}$$

where C_m is the inertia coefficient, C_d is the drag coefficient, and water particle velocity u and acceleration $\dot{u}$ are solved using first-order linear wave theory, which is also called air wave theory.

The specifics of Gaussian wind model DLCs are listed in Table 4.3. The standard deviation values of DLC 1.x series are obtained from IEC NTM B.

DLC/ Gaussian	Wind		Wave	
	Mean (m/s)	Std (m/s)	Significant Height (m)	Peak Period (s)
1.1	4	1.20	0.24	2.46
1.2	6	1.41	0.55	3.69
1.3	8	1.62	0.98	4.92
1.4	10	1.83	1.53	6.15
1.5	12	2.04	2.20	7.38
1.6	14	2.25	3.00	8.62
1.7	16	2.46	3.91	9.85
1.8	18	2.67	4.95	11.08
1.9	20	2.88	6.12	12.31
1.10	22	3.09	7.40	13.54
1.11	24	3.30	8.82	14.78

Table 4.3: DLCs for Gaussian cases

The series of DLCs with a non-Gaussian wind model are simulated in order to compare with previous simulation results. DLC 2.x series are designed with a lookup table of field measurements and are supposed to achieve more accurate results. The specifics of field observation data are listed in Table 4.4 (Dai and Sweetman, 2019).

Wind speed	4	5	6	7	8	9	10	11	12	13
Skewness α_3	0.20	0.35	0.62	0.70	0.87	0.88	1.00	1.10	1.08	1.16
Kurtosis α_4	2.71	3.04	3.48	3.70	4.24	4.18	4.50	4.71	4.81	4.77

Table 4.4: Skewness and kurtosis of measured near-shore winds

The specifics of non-Gaussian wind model DLCs are listed in Table 4.5. The skewness and kurtosis values of DLC 2.x series are obtained from field observation data using linear interpolation.

DLC/ Non-Gaussian	Wind				Wave	
	Mean (m/s)	Std (m/s)	Skewness	Kurtosis	Significant Height (m)	Peak Period (s)
2.1	4	1.20	0.2	2.7	0.24	2.46
2.2	6	1.41	0.6	3.4	0.55	3.69
2.3	8	1.62	0.8	4.2	0.98	4.92
2.4	10	1.83	1.0	4.5	1.53	6.15
2.5	12	2.04	1.0	4.8	2.20	7.38
2.6	14	2.25	1.1	4.7	3.00	8.62
2.7	16	2.46	1.1	4.7	3.91	9.85
2.8	18	2.67	1.1	4.7	4.95	11.08
2.9	20	2.88	1.1	4.7	6.12	12.31
2.10	22	3.09	1.1	4.7	7.40	13.54
2.11	24	3.30	1.1	4.7	8.82	14.78

Table 4.5: DLCs for non-Gaussian cases with dynamic coefficients

A 5-MW wind turbine representing the NREL OC3-Hywind model (Jonkman, et. al, 2009) is selected in the example. This model is commonly used in academic research and is used for the example section of this chapter. The properties of the 5-MW OC3-Hywind wind turbine are shown in Table 4.6.

Rotor, hub diameter	126, 3 m
Hub height	90 m
Cut-in, rated, Cut-out wind speed	3, 11.4, 25 m/s
Cut-in, rated rotor speed	6.9, 12.1 rpm
Generator electrical efficiency	94.4%
Rotor mass	110,000 kg
Nacelle mass	240,000 kg
Tower mass	347,460 kg
Initial CM	85.6 m
Elevation to tower top	87.6 m
Platform diameter above taper	6.5 m
Platform diameter below taper	9.4 m
Platform draft	120 m

Table 4.6: OC3-Hywind 5MW wind turbine parameters for fatigue analysis

A 5-MW NREL turbine blade is used for the example, with a 61.5-m-long blade with a rated rotation speed of 12.1 rpm (Jonkman, et. al, 2009). The blade is discretized into 23 elements using the Loose code with a nonlinear beam blade solver. The stiffness-damping coefficient is set to 0.003, and the time step is set to 0.005 (Tang and Sweetman, 2019).

4.3.2 Results

Short-term numerical simulations with different wind conditions are conducted by Loose with a nonlinear beam blade solver. The damage matrices, D_i, of each DLC based on the numerical

simulation results are normalized by the maximum fatigue damage within each DLC in order to identify the shift of the fatigue damage hot-spot.

$$[\boldsymbol{D_i}]_N = \frac{[\boldsymbol{D_i}]}{max([\boldsymbol{D_i}])} \tag{4.20}$$

The normalized fatigue damage diagram of Gaussian wind model DLCs is shown in Figure 4.6. The normalized fatigue damage diagram of non-Gaussian wind model DLCs is similar to that of Gaussian DLCs.

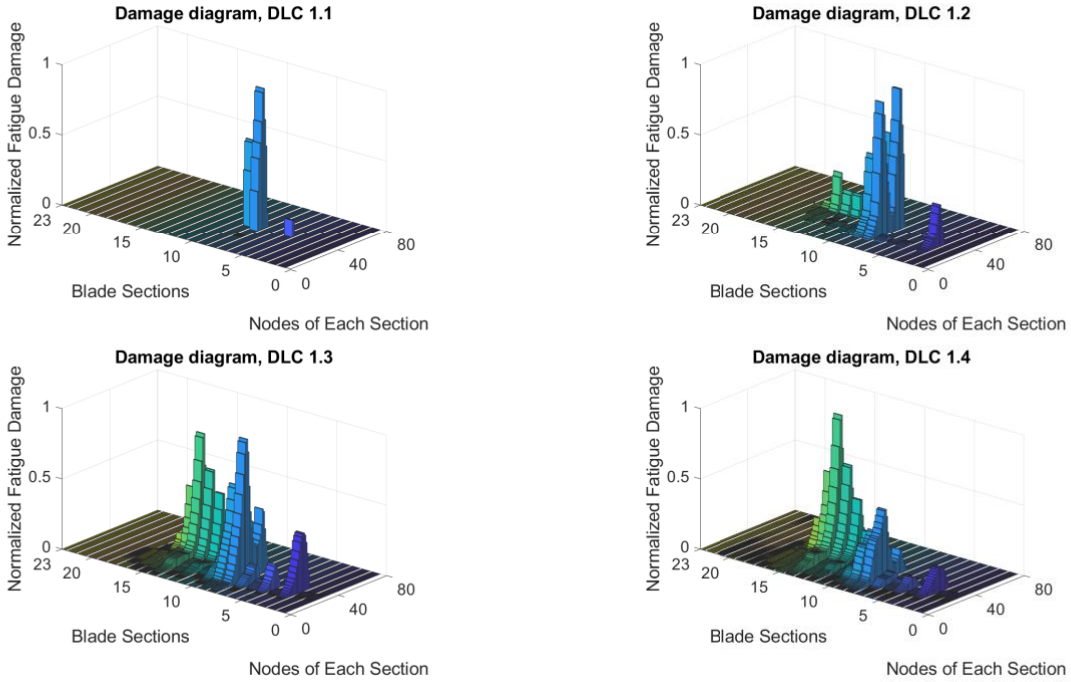

(a) Damage diagram of Gaussian wind model DLC 1.1 to 1.4

Figure 4.6: Damage diagram of Gaussian wind model DLCs

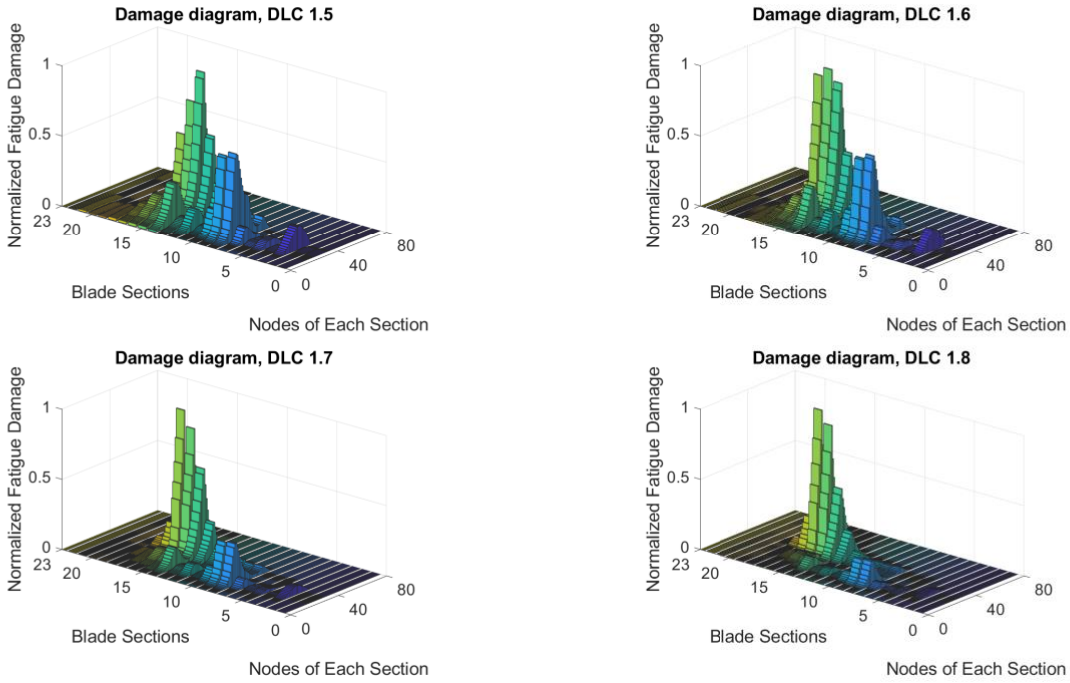

(b) Damage diagram of Gaussian wind model DLC 1.5 to 1.8

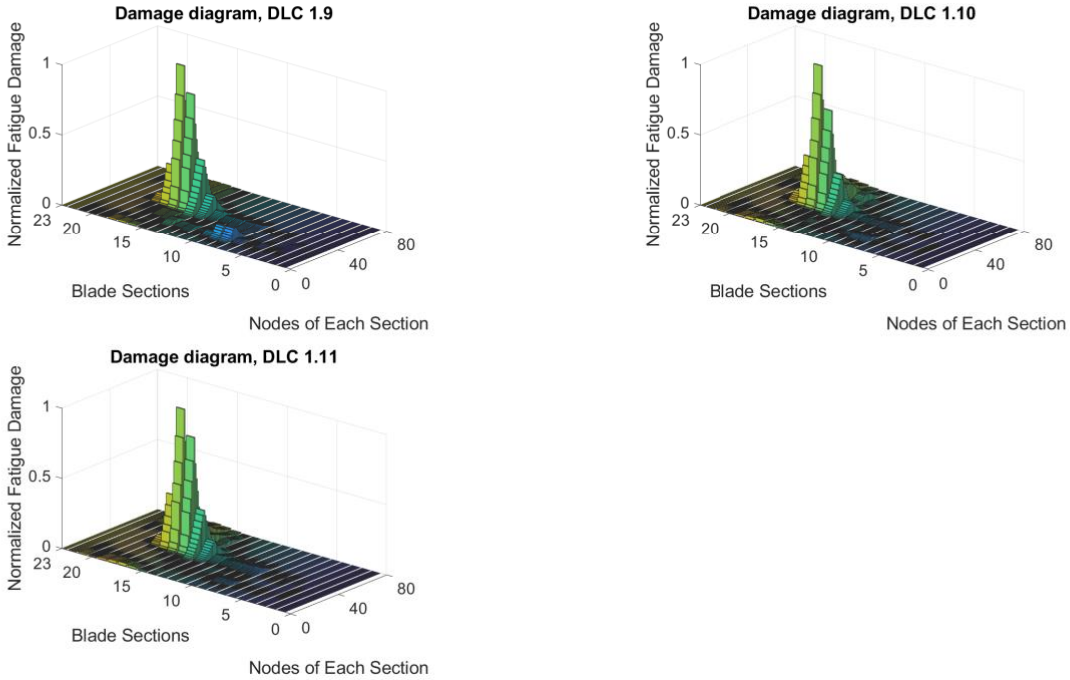

(c) Damage diagram of Gaussian wind model DLC 1.9 to 1.11

Figure 4.6 continued.

This damage diagram indicates that the initial hot spot occur at the section close to the root of the blade in the first several DLCs when then mean wind speeds are lower than rated. The hot spot then shift to the tip of the blade, and the fatigue damage increased as well. The movement of the hot spot ended when the wind speed went beyond the rated speed. The damage diagrams remain the same for the last several DLCs.

The fatigue damage expectations of wind-speed bars in the Gaussian wind model are listed in Table 4.7.

Wind speed (m/s)		**4-5**	**6-7**	**8-9**	**10-11**	**12-13**	**14-15**
Damage $\boldsymbol{D_i}$	Case1	0	7	51	250	364	494
(10^{-4})	Case2	0	7	54	290	456	656
Fatigue Life $\boldsymbol{T_Y}$	Case1	N/A	N/A	1961	400	275	202
(year)	Case2	N/A	N/A	1852	345	219	152
Wind speed (m/s)		**16-17**	**18-19**	**20-21**	**22-23**	**24-25**	**Total**
Damage $\boldsymbol{D_i}$	Case1	339	371	335	220	270	2703
(10^{-4})	Case2	444	479	419	308	270	3384
Fatigue Life $\boldsymbol{T_Y}$	Case1	29	27	30	45	37	3.7
(year)	Case2	23	21	24	32	37	3.0

Table 4.7: Adjusted hot-spot fatigue damage of Gaussian wind model

The contribution of fatigue damage changed rapidly among different wind-speed bars. Wind speed below the rated wind speed (11.4 m/s) caused almost zero fatigue damage to the turbine blades. Fatigue damage increased dramatically once wind speed went beyond the rated speed. Although

the fatigue damage continued increasing with wind speed, the long-term wind-speed distribution indicates that the probability of duration continued decreasing for high wind speed. Combing these two consequences together, the fatigue analysis shows the majority of the total fatigue damage to have been contributed by wind-speed bars from 12 to 20 m/s, where both the fatigue damage and probability of duration were relatively large.

The total fatigue damage of the Gaussian wind model is the summation of expectations— 0.270 for Case 1 and 0.338 for Case 2, as shown in Figure 4.7.

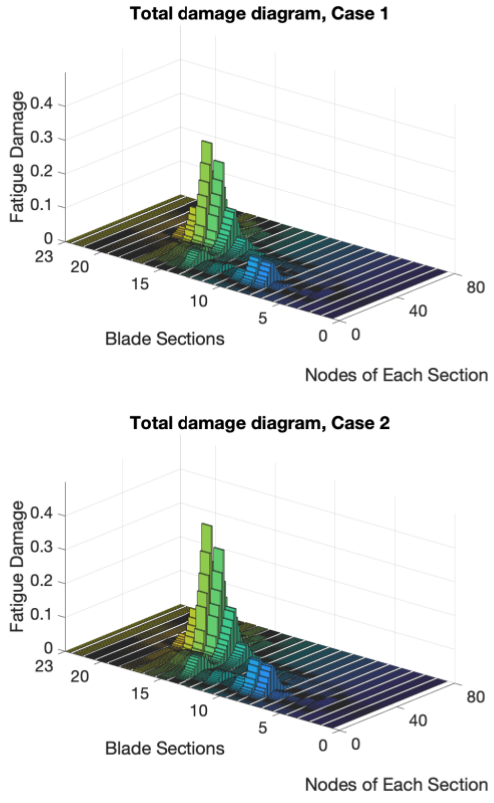

Figure 4.7: Total fatigue damage diagram of Gaussian wind model

The fatigue damage expectations of wind-speed bars in the non-Gaussian wind model are listed in Table 4.8.

Wind speed (m/s)		**4-5**	**6-7**	**8-9**	**10-11**	**12-13**	**14-15**
Damage $\boldsymbol{D_i}$	Case1	0	15	90	735	709	1466
(10^{-4})	Case2	0	14	95	852	889	1947
Fatigue Life $\boldsymbol{T_Y}$	Case1	N/A	667	111	14	14	7
(year)	Case2	N/A	714	105	12	11	5
Wind speed (m/s)		**16-17**	**18-19**	**20-21**	**22-23**	**24-25**	**Total**
Damage $\boldsymbol{D_i}$	Case1	857	1199	802	588	843	7304
(10^{-4})	Case2	1122	1549	1002	823	843	9135
Fatigue Life $\boldsymbol{T_Y}$	Case1	12	8	13	17	12	1.4
(year)	Case2	9	6	10	12	12	1.1

Table 4.8: Adjusted hot-spot fatigue damage of non-Gaussian wind model

The total fatigue damage of the non-Gaussian wind model is the summation of expectations—0.730 for Case 1 and 0.913 for Case 2, as shown in Figure 4.8.

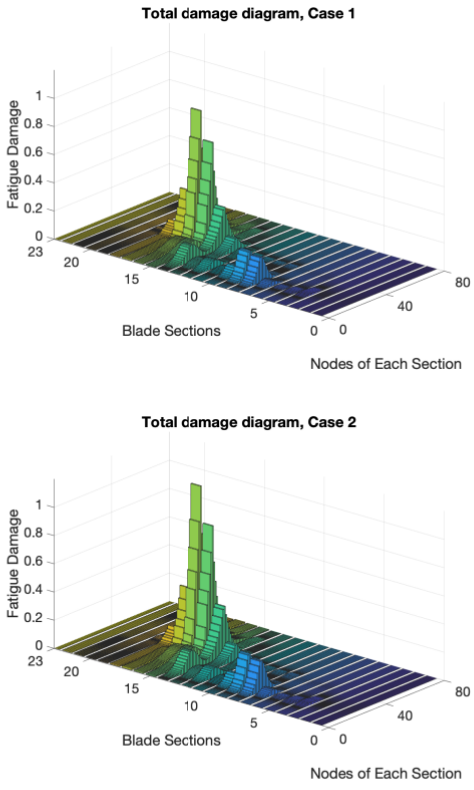

Figure 4.8: Total fatigue damage diagram of non-Gaussian wind model

The summary of blade fatigue life prediction for the two cases of Gaussian wind model and non-Gaussian wind model are listed in Table 4.9.

	Case 1	Case 2	Difference	Percentage difference
Gaussian model	3.7	3.0	0.7	18.9%
Non-Gaussian model	1.4	1.1	0.3	21.4%
Difference	2.3	1.9		
Percentage difference	62.2%	63.3%		

Table 4.9: Summary of estimations of blade fatigue life (yr)

The results indicate that long-term wind distribution at different locations averaged 0.5 yr, which is an approximate 20% difference from predicted fatigue life. The Gaussian wind model consistently overpredicted for around 1.1 yr, which is a 62% difference from predicted fatigue life. This result demonstrates that both factors are important to blade fatigue life and that cracks occur much earlier for wind turbines under non-Gaussian wind conditions.

4.4 Conclusion

This chapter proposes a new blade fatigue life estimation method that combines long-term wind-speed distribution and short-term wind-field simulation. The analysis of long-term wind-speed distribution helps to identify the various contributions of fatigue damage from different wind speeds. A numerical transformation method is proposed, including both a Gaussian wind model and non-Gaussian wind model in short-term wind simulation.

A 5-MW NERL wind turbine and its blade were used for the case study, with both wind models at two offshore locations. Blade fatigue damage and fatigue life were calculated and analyzed. The results demonstrate that most fatigue damage was caused by wind speed above the rated speed (11 to 20 m/s). Low wind speeds (4 to 11 m/s) caused almost zero fatigue damage, and high wind speeds (20+ m/s) caused less fatigue because of the small percentage of duration.

Fatigue damage caused by non-Gaussian wind proved more significant than Gaussian wind, which aligns with other research results (e.g., Gong & Chen, 2014). Both kurtosis and skewness values are important to fatigue and vary among different wind-speed bars. This phenomenon demonstrates that the current mainstream method of fatigue prediction systematically underpredict the annual fatigue damage of FOWT blades.

5. SUMMARY

5.1 Conclusion

In this dissertation, a new approach on the statistical characteristics of natural wind is presented the improvements of power forecasting and blade fatigue estimation for FOWTs. The research hypothesis is well proven through this dissertation. The new methodology is developed with random process theory to predict wind-power output with much less computation time and the same accuracy as mainstream numerical simulations. A non-Gaussian process is applied in numerical analysis of a nonlinear dynamic system of structures to correctly represent its influence on wind power and fatigue damage. The overall methodology demonstrates that the natural wind is non-Gaussian and that this factor is not included in current FOWTs design considerations. In fact, the traditional Gaussian assumption of wind process underestimates blade damage, which cannot be neglected in wind-turbine design.

In Chapter 2, the EOM of a cup rotor is investigated by relating the rotational motion of the cup rotor to aerodynamic force. Wind-speed measurements from indoor and outdoor experiments are used to determine the dynamic coefficients of the EOM. Further recalibration for the mean wind is proposed based on random process theory. Data from two 2-month field measurement programs on the Texas coast are used to assess the higher statistical moments of the wind process. The overall methodology is then applied to recover the time history and mean of the true wind speed from field-measured cup data. Different wind processes, such as sea breeze, land breeze, and bay breeze, are identified during statistical analysis of the field data. Measured coastal sea breezes in this area

are found to be non-Gaussian, as shown in Chapter 2. Other measured wind processes are shown in Appendix A.

In Chapter 3, a new methodology of analytical expressions for expected power and standard deviation of power is derived based on random process theory. The resulting expressions explicitly include the effects of varying turbulence intensity and higher statistical moments, and they enable the performance of an operating wind turbine to be parameterized using a limited number of coefficients. Benchmarking direct simulation in irregular winds, including winds with various turbulence intensities and non-Gaussian wind, is applied to demonstrate the accuracy of the expected power and standard deviation of power predicted by this new method.

In Chapter 4, a new methodology for estimating blade fatigue life is proposed, including long-term wind-speed distribution and short-term Gaussian and non-Gaussian wind simulations. Weibull distribution is applied for long-term distribution at two selected buoys to calculate the probabilities of wind DLCs. Gaussian and non-Gaussian distributions are applied for short-term winds to form each wind DLC. Numerical simulations based on the OC3-Hywind model with local winds PDF are used to identify fatigue hot spots on the blades. The impact of non-Gaussian wind on blade fatigue is analyzed by comparing the fatigue damage of Gaussian and non-Gaussian winds at hot spots.

5.2 Future Recommendations

This dissertation presents a new non-Gaussian statistical wind model and its application to power forecasting and fatigue life estimation of compliant floating wind turbines. There are several possible developments for future work, as outlined below.

1. Field wind–measurement campaigns should be extended for longer periods to collect more wind-speed segments for statistical analysis. The current non-Gaussian wind model of high wind speed is not very accurate because of a limited amount of data. The statistical parameters of high-wind-speed cases could be more accurate using additional raw data.

2. The EOM of rotors could be improved to better describe their aerodynamic response. A well-designed experiment with high-tech equipment could obtain more accurate coefficients for the EOM.

3. The proposed a method could be used to develop a real-time offshore wind-power forecast system. This wind-power forecast system could be used to predict real-time wind-electricity price and may further be used as a financial tool for clean energy investment in the stock market.

4. Instruments installed on NOAA buoys could be improved to enable long-term, high-frequency onsite measurements. Future analysis on NOAA buoy data could help to obtain location-based non-Gaussian wind models.

5. The power forecast method including the factors of wind and wave direction could better evaluate their influence on the power performance of FOWTs. The influence of wind direction has not been important to the OC3-Hywind model in previous work, but it may have significant influence for other FOWT models.

6. Another interesting topic around FOWTs is nacelle yaw control. Blade pitch control has proven to be significant for both power output and blade fatigue damage. The nacelle yaw control strategy which decide the response speed of a nacelle according to wind direction changes. An advanced yaw control strategy could improve the power performance of FOWTs.

REFERENCES

[1] Agrawal, R., Faloutsos, C., & Swami, A. (1993, October). Efficient similarity search in sequence databases. *International Conference on Foundations of Data Organization and Algorithms* (pp. 69-84). Springer, Berlin, Heidelberg.

[2] AWEA. (2018). American's new ocean energy resource. www.awea.org/policy-and-issues/u-s-offshore-wind.

[3] Berg, J., Natarajan, A., Mann, J., & Patton, E. G. (2016). Gaussian vs non - Gaussian turbulence: impact on wind turbine loads. *Wind Energy*, 19(11), 1975-1989.

[4] Böttcher, F., Peinke, J., Kleinhans, D., & Friedrich, R. (2007). Handling systems driven by different noise sources: implications for power curve estimations. In *Wind Energy* (pp. 179-182). Springer, Berlin, Heidelberg.

[5] Brevoort, M. J., & Joyner, U. T. (1934). *Aerodynamic characteristics of anemometer cups*. U.S. National Aeronautics and Space Administration.

[6] Brown, C. (2012). *Fast verification of wind turbine power curves: summary of project results* (Doctoral dissertation, Master Thesis, Technical University of Denmark, DTU Informatics (IMM-M. Sc.-2012-72)).

[7] Burton, T., Sharpe, D., Jenkins, N., & Bossanyi, E. (2001). *Wind energy handbook*. John Wiley & Sons.

[8] Busch, N. E., & Kristensen, L. (1976). Cup anemometer over speeding. *Journal of Applied Meteorology*, 15(12), 1328-1332.

[9] Carrillo, C., Montaño, A. O., Cidrás, J., & Díaz-Dorado, E. (2013). Review of power curve modelling for wind turbines. *Renewable and Sustainable Energy Reviews*, 21, 572-581.

[10] Chen, J., (2011), Development of offshore wind power in China, *Renewable and Sustainable Energy Reviews*, Volume 15, Issue 9, Pages 5013–5020

[11] Chien, W. T. K., & Yang, S. F. (2008). Using reverse arrangement test to detect non-monotonic trends for semiconductor manufacturing and reliability tests. *International Journal of Reliability, Quality and Safety Engineering*, 15(06), 497-514.

[12] Choi, M., & Sweetman, B. (2010). The Hermite moment model for highly skewed response with application to tension leg platforms. *Journal of Offshore Mechanics and Arctic Engineering*, 132(2), 021602.

[13] Corcoran, J. W., and D. L. Esau, 1964: Comparison of a theoretical model for anemometer cups with experimental data. *Meteor. Rept. No. 9*, San Carlos, Calif., Beckman and Whitney, Inc., 21 pp.

[14] Coquilla, R. V., Obermeier, J., & White, B. R. (2007). Calibration procedures and uncertainty in wind power anemometers. *Wind Engineering*, 31(5), 303-316.

[15] Dai, S., & Sweetman, B. (2015). Statistical condensation of meteorological ocean data for wind turbine design. *The 20th Offshore Symposium*, Society of Naval Architects and Marine Engineers

[16] Dai, S., & Sweetman, B. (2016). Rational selection of floater designs for offshore wind farms using power transfer functions. *The 26th International Ocean and Polar Engineering Conference.* International Society of Offshore and Polar Engineers.

[17] Dai, S., & Sweetman, B. (2020). A methodology to recalibrate cup anemometers with application to statistical analysis of sea breezes. *Under review.*

[18] Dai, S., & Sweetman, B. (2020). Field measurement campaigns and identification of sea breeze and land Breeze. *In progress*.

[19] Dai, S., & Sweetman, B. (2020). Impact of non-Gaussian winds on blade fatigue life of floating offshore wind turbines. *In progress*.

[20] Dai, S., & Sweetman, B. (2020). Transformation of wind turbine power curves using the statistics of the wind process. *Under review*.

[21] Fortin, G., Perron, J., & Ilinca, A. (2005). Behavior and modeling of cup anemometers under Icing conditions. *IWAIS XI*, Montreal, June 2005

[22] Gong, K., & Chen, X. (2014). Influence of non-Gaussian wind characteristics on wind turbine extreme response. *Engineering Structures*, 59, 727-744.

[23] Gontier, H., Schaffarczyk, A. P., Kleinhans, D., & Friedrich, R. (2007). A comparison of fatigue loads of wind turbine resulting from a non-Gaussian turbulence model vs. standard ones. *Journal of Physics: Conference Series*. Vol. 75, No. 1, p. 012070.

[24] Gao, J., & Sweetman, B. (2018). Design optimization of hull size for spar-based floating offshore wind turbines. *Journal of Ocean Engineering and Marine Energy*, 4(3), 217-229.

[25] Greene, W. H. (2003). *Econometric analysis*. Pearson Education India, 759

[26] Hasselmann, K., Barnett, T. P., Bouws, E., Carlson, H., Cartwright, D. E., Enke, K…, & Meerburg, A. (1973). Measurements of wind-wave growth and swell decay during the Joint North Sea Wave Project (JONSWAP). *Ergänzungsheft* 8-12

[27] Headrick, T. C. (2009). Statistical simulation: *Power method polynomials and other transformations*. Chapman and Hall/CRC.

[28] Hölling, M., Schulte, B., Barth, S., & Peinke, J. (2007, July). Sphere anemometer-a faster alternative solution to cup anemometry. In *Journal of Physics: Conference Series* (Vol. 75, No. 1, pp. 1-6).

[29] Holthuijsen, L. H. (2010). *Waves in oceanic and coastal waters*. Cambridge University Press.

[30] Hrafnkelsson, B., Oddsson, G., & Unnthorsson, R. (2016). A method for estimating annual energy production using Monte Carlo wind speed simulation. *Energies*, 9(4), 286.

[31] Hsu, S. A., Meindl, E. A., & Gilhousen, D. B. (1994). Determining the power-law wind-profile exponent under near-neutral stability conditions at sea. *Journal of Applied Meteorology*, 33(6), 757-765.

[32] Hu, J., & Wang, J. (2015). Short-term wind speed prediction using empirical wavelet transform and Gaussian process regression. *Energy*, 93, 1456-1466.

[33] Huang, H., Zhang, J., & Zhu, L. (2013). Numerical model of a tensioner system and riser guide. *Ocean Systems Engineering*, 3(4), 257-273.

[34] International Electrotechnical Commission. (2005). *Power performance measurements of electricity producing wind turbines*. Geneva, Switzerland, IEC, 61400-12.

[35] International Electrotechnical Commission. (2006). Wind turbines-part 1: design requirements. *IEC 614001 Ed. 3.*

[36] Ishihara, T., Yamaguchi, A., & Sarwar, M. W. (2012). A study of the normal turbulence model in IEC 61400-1. *Wind Engineering*, 36(6), 759-765.

[37] Jefferys, E. R. (1987). Directional seas should be ergodic. *Applied Ocean Research*, 9(4), 186-191.

[38] Jonkman, B. J. (2009). *TurbSim user's guide: Version 1.50* (No. NREL/TP-500-46198). National Renewable Energy Lab. (NREL), Golden, CO (United States).

[39] Jonkman, J., Butterfield, S., Musial, W., & Scott, G. (2009). *Definition of a 5-MW reference wind turbine for offshore system development* (No. NREL/TP-500-38060). National Renewable Energy Lab. (NREL), Golden, CO (United States).

[40] Kareem, A. A., Tognarelli, M. A., & Gurley, K. R. (1998). Modeling and analysis of

quadratic term in the wind effects on structures. *Journal of Wind Engineering and Industrial Aerodynamics*, 74, 1101-1110.

[41] Kendall, M. G. (1938). A new measure of rank correlation. *Biometrika*, 30(1/2), 81-93.

[42] Knauer, A., Hanson, T. D., & Skaare, B. (2006). Offshore wind turbine loads in deep-water environment. *EWEC 2006*.

[43] Kondo, J., Naito, G. I., & Fujinawa, Y. (1971). Response of cup anemometer in turbulence. *Journal of the Meteorological Society of Japan. Ser. II*, 49(2), 63-74.

[44] Kong, C., Bang, J., & Sugiyama, Y. (2005), Structural investigation of composite wind turbine blade considering various load cases and fatigue life, *Energy*, 2101-2114

[45] Kong, C., Kim, T., Han, D., & Sugiyama, Y. (2006). Investigation of fatigue life for a medium scale composite wind turbine blade. *International Journal of Fatigue*, 28(10), 1382-1388

[46] Kotz, S., Balakrishnan, N., & Johnson, N. L. (2004). *Continuous multivariate distributions, Volume 1: Models and applications* (Vol. 1). John Wiley & Sons.

[47] Kristensen, L. (2002). Can a cup anemometer ‘underspeed'?. *Boundary-Layer Meteorology*, 103(1), 163-172.

[48] Kusiak, A., Zheng, H., & Song, Z. (2009). Short-term prediction of wind farm power: A data mining approach. *IEEE Transactions on Energy Conversion*, 24(1), 125-136.

[49] Lei, M., Shiyan, L., Chuanwen, J., Hongling, L., & Yan, Z. (2009). A review on the forecasting of wind speed and generated power. *Renewable and Sustainable Energy Reviews*, 13(4), 915-920.

[50] Li, S., Wunsch, D. C., O'Hair, E. A., & Giesselmann, M. G. (2001). Using neural networks to estimate wind turbine power generation. *IEEE Transactions on Energy Conversion*, 16(3), 276-282.

[51] Liu, H., Tian, H. Q., Chen, C., & Li, Y. F. (2010). A hybrid statistical method to predict wind speed and wind power. *Renewable Energy*, 35(8), 1857-1861.

[52] Lydia, M., Kumar, S. S., Selvakumar, A. I., & Kumar, G. E. P. (2014). A comprehensive review on wind turbine power curve modeling techniques. *Renewable and Sustainable Energy Reviews*, 30, 452-460.

[53] Mabel, M. C., & Fernandez, E. (2008). Analysis of wind power generation and prediction using ANN: A case study. *Renewable Energy*, 33(5), 986-992.

[54] MacCready Jr, P. B. (1966). Mean wind speed measurements in turbulence. *Journal of Applied Meteorology*, 5(2), 219-225.

[55] Mann, H. B. (1945). Nonparametric tests against trend. *Econometrica: Journal of the Econometric Society*, 245-259.

[56] Moriarty, P. J., & Hansen, A. C. (2005). *AeroDyn theory manual* (No. NREL/TP-500-36881). National Renewable Energy Lab., Golden, CO (US).

[57] Mücke, T., Kleinhans, D., & Peinke, J. (2011). Atmospheric turbulence and its influence on the alternating loads on wind turbines. *Wind Energy*, 14(2), 301-316.

[58] Navidi, W., *Statistics for Engineers and Scientists*, 2nd, (2008). McGraw-Hill

[59] Nijssen, R. P. L. (2006). Fatigue life prediction and strength degradation of wind turbine rotor blade composites. Contractor Report SAND2006-7810P, Sandia National Laboratories, Albuquerque, NM

[60] Pan, Y., & Patton, E. G. (2017). On Determining Stationary Periods within Time Series.

Journal of Atmospheric and Oceanic Technology, 34(10), 2213-2232.

[61] Pardalos, P. M., Rebennack, S., Pereira, M. V., Iliadis, N. A., & Pappu, V. (2013). *Handbook of wind power systems*. Springer Berlin Heidelberg.

[62] Pedersen, T. F. (2004). On wind turbine power performance measurements at inclined airflow. *Wind Energy: An International Journal for Progress and Applications in Wind Power Conversion Technology*, 7(3), 163-176.

[63] Poulsen, T., & Hasager, C. B. (2016). How expensive is expensive enough? Opportunities for cost reductions in offshore wind energy logistics. *Energies*, 9(6), 437.

[64] Ramsey, F. L., Schafer, Daniel W., (1996). *The Statistical Sleuth: A Course in Methods of Data Analysis*, Duxbury Press

[65] Ramachandran, S. (1966). *Transient response of anemometers*, Doctoral dissertation, Poona University, India.

[66] Ramachandran, S. (1969). A theoretical study of cup and vane anemometers. *Quarterly Journal of the Royal Meteorological Society*, 95(403), 163-180.

[67] Ronold, K. O., & Christensen, C. J. (2001). Optimization of a design code for wind-turbine rotor blades in fatigue. *Engineering Structures*, 23(8), 993-1004

[68] Schottler, J., Reinke, N., Hölling, A., Whale, J., Peinke, J., & Hölling, M. (2017). On the impact of non-Gaussian wind statistics on wind turbines–an experimental approach. *Wind Energy Science*, 2(1), 1-13.

[69] Sea breeze. (2019). Retrieved from https://en.wikipedia.org/wiki/Sea_breeze

[70] Snyder, B., Kaiser, M. J., (2009). A comparison of offshore wind power development in Europe and the U.S.: Patterns and drivers of development, *Applied Energy*, Volume 86, Issue 10, Pages 1845–1856

[71] Shokrzadeh, S., Jozani, M. J., & Bibeau, E. (2014). Wind turbine power curve modeling using advanced parametric and nonparametric methods. *IEEE Transactions on Sustainable Energy*, 5(4), 1262-1269.

[72] Shu, Z. R., Li, Q. S., & Chan, P. W. (2015). Statistical analysis of wind characteristics and wind energy potential in Hong Kong. *Energy Conversion and Management*, 101, 644-657

[73] Shuang, M., & Song, B. (2018). Reliability analysis of wind turbines under non-Gaussian wind load. *The Structural Design of Tall and Special Buildings*, 27(3), e1443

[74] Sohoni, V., Gupta, S., & Nema, R. (2016). A comparative analysis of wind speed probability distributions for wind power assessment of four sites. *Turkish Journal of Electrical Engineering & Computer Sciences*, 24(6), 4724-4735.

[75] Skaare, B. (2017, June). Development of the hywind concept. In *ASME 2017 36th International Conference on Ocean, Offshore and Arctic Engineering* (pp. V009T12A050-V009T12A050). American Society of Mechanical Engineers.

[76] Sweetman, B., & Wang, L. (2012). Floating offshore wind turbine dynamics: large-angle motions in Euler-space. *Journal of Offshore Mechanics and Arctic Engineering*, 134(3), 031903.

[77] Sweetman, B., & Wang, L. (2014). Momentum cloud method for dynamic simulation of rigid body systems. *Journal of Engineering Mechanics*, 140(2), 257-267.

[78] Sweetman, B., & Wilder, B. (2014, May). Numerical simulation of floating offshore wind turbines including aero-elasticity and active blade pitch control. In *Offshore Technology Conference*. Offshore Technology Conference.

[79] Tang, S., & Sweetman, B. (2019). A geometrically-exact momentum-based non-linear theory applicable to beams in non-inertial frames. *International Journal of Non-Linear Mechanics*.

[80] Thresher, R., Robinsion, M., & Veers, P. (2008). *Wind energy technology: current status and R&D future* (No. NREL/CP-500-43374). National Renewable Energy Lab. (NREL), Golden, CO (United States).

[81] Tong, W. (2010). *Wind power generation and wind turbine design*. WIT press.

[82] U. S. Army Engineer District, Galveston Crops of Engineer. (1983). *Galveston Creek Shore Erosion Study: Environmental Impact Statement*, Volume 1, 35

[83] Van Bussel, G. J. W., & Zaaijer, M. B. (2001, March). Reliability, availability and maintenance aspects of large-scale offshore wind farms, a concepts study. *In Proceedings of MAREC* (Vol. 2001).

[84] Veritas, N. (2000). *Environmental conditions and environmental loads*. Det Norske Veritas.

[85] Wieringa, J. (1980). A revaluation of the Kansas mast influence on measurements of stress and cup anemometer over speeding. *Boundary-Layer Meteorology*, 18(4), 411-430.

[86] Wang, L., & Sweetman, B. (2011). Conceptual design of floating wind turbines with large-amplitude motion. *Proceedings of Society of Naval Architects and Marine Engineers*, 58-67.

[87] Wang, L., & Sweetman, B. (2012). Simulation of large-amplitude motion of floating wind turbines using conservation of momentum. *Ocean Engineering*, 42, 155-164.

[88] Wang, L. (2012). *Multibody dynamics using conservation of momentum with application to compliant offshore floating wind turbines*. Doctoral dissertation, Texas A&M University.

[89] Wang, L., & Sweetman, B. (2013). Multibody dynamics of floating wind turbines with large-amplitude motion. *Applied Ocean Research*, 43, 1-10.

[90] Watson, G., Hill, B., Courtney, F., Goldman, P., Calvert, S., Thresher, R., ... & Bell, B. (2005). A framework for offshore wind energy development in the United States. *Massachusetts Technology Collaborative (MTC).*

[91] Winterstein, S. R. (1988). Nonlinear vibration models for extremes and fatigue. *Journal of Engineering Mechanics*, 114(10), 1772-1790.

[92] Zhou, Z. (2007). *Characteristics Analysis and Experimental Research on the Three-Cup Anemometer*. Master. Thesis, Harbin Institute of Technology.

[93] Ziter, B., & Lubitz, W. D. (2010). Predicting hub-height wind speed for small wind turbine performance evaluation using tower-mounted cup anemometers. *Wind Engineering*, 34(6), 673-699.

[94] Z.R. Shu, Q.S.Li, P.W.Chan. (2014). Statistical analysis of wind characteristics and wind energy potential in Hong Kong, *Energy conversion and Management*, 644-657

APPENDIX A

FIELD MEASUREMENT CAMPAIGNS AND

IDENTIFICATION OF SEA BREEZE AND LAND BREEZE

A.1 Introduction

Two field measurement campaigns were completed as part of this work to quantify the higher statistical moments of the natural wind because of unavailability of short-term measured wind time histories with high sampling rates. These two measurement campaigns represent relatively long deployments of a cup anemometer, taking place in March 2017 and February 2018. Two cup anemometer–based campaigns recorded wind speeds and directions for 3 months at a sampling rate of 1 Hz. These wind speeds were measured at two coastal locations in Galveston, Texas, USA, as shown in Figure A.1.

Figure A.1: Field campaign locations

The first campaign quantified short-term wind conditions with a primary interest in the statistics of winds blowing directly ashore from the Gulf of Mexico. The spring wind data were captured near Seawall Boulevard on Galveston Island (29°16'38.0"N, 94°48'40.4"W), approximately 250 m from the Gulf of Mexico. The wind speed anemometer was deployed 10 m above the ground in conformance with the industry standard.

The second campaign quantified wind conditions with a primary interest in winds blowing initially over land and then ashore directly from Galveston Bay. The wind data were collected on the campus of Texas A&M University at Galveston on Pelican Island (29°19'10.5"N, 94°49'02.2"W), approximately 4 km from a southern boundary of Galveston Bay and 5 km from the Gulf of Mexico. The fetch over Galveston Bay at this location is as much as 10 NM when wind is blowing from the north and 5 NM when wind is blowing from the northeast. The wind speed anemometer was installed on a mobile weather station in the middle of a roof 25 m above ground. The weather station was deployed more than 10 m away from the edge of the building to avoid turbulence flow at the edge area. Photos of the two field measurement campaigns are shown in Figure A.2.

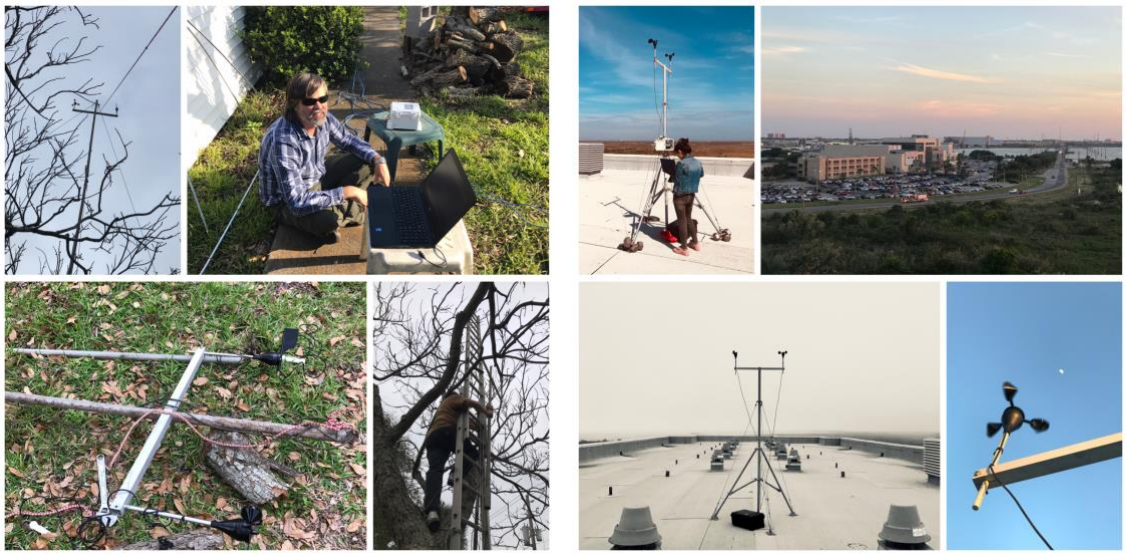

Figure A.2: First (left) and second (right) field measurement campaigns

A.2 Preliminary Analysis

The long field-measured wind speed time histories are extensively processed after the field collection. The raw data are divided into segments of 10-min and then plotted in a three-dimensional (3D) space formed by mean wind speed, standard deviation, and mean wind direction. The results of two campaigns are presented in Figure A.3. The plot of the first measurement campaign showed winds from the north (Land breeze) to have a significantly higher standard deviation than those from the south (Sea breeze). The plot of the second measurement campaign showed winds from the south (Sea breeze, overland) to have a significantly higher standard deviation than those from the north (Bay breeze).

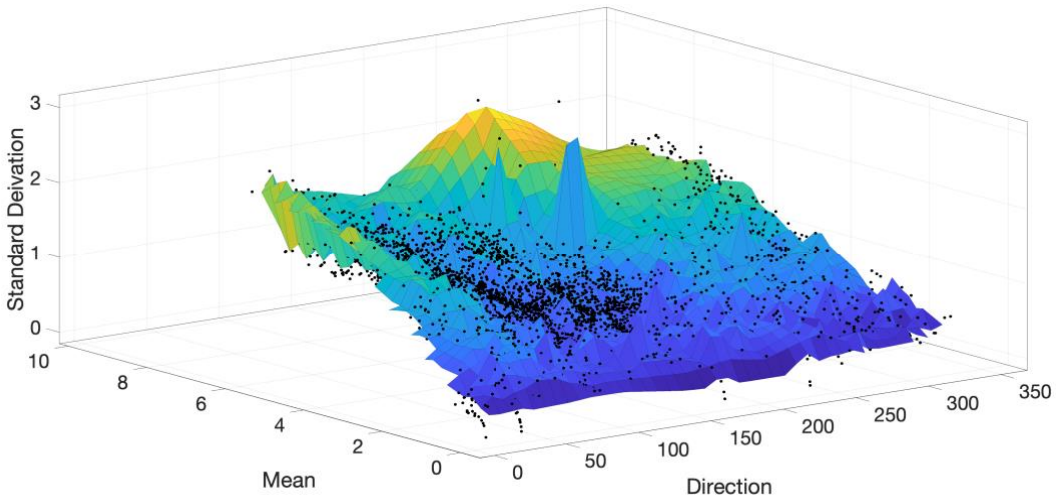

(a) Data from campaign 1

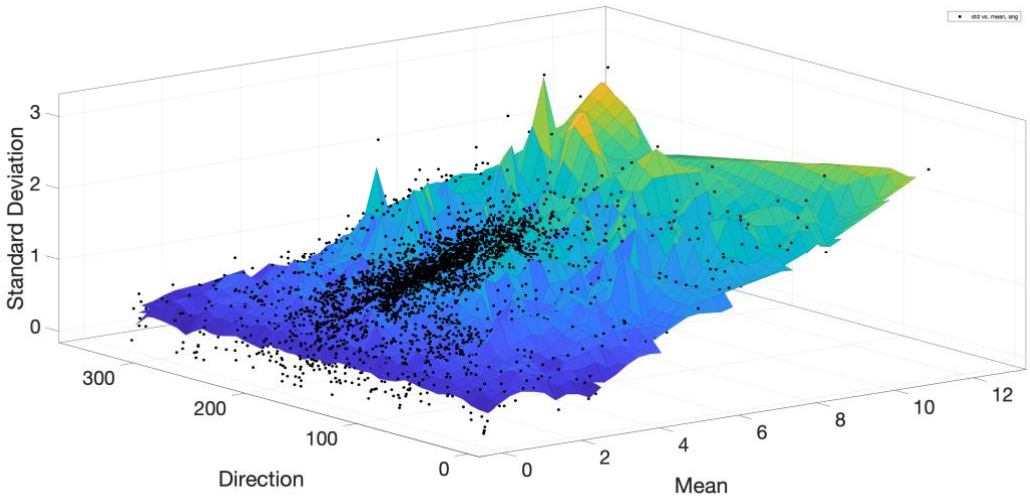

(b) Data from campaign 2

Figure A.3: Standard deviation plotted as a function of mean and direction

Wind speed data from the first and second campaigns are presented as monthly wind rose figures (Figure A.4). Atmospheric wind circulation was blown from two major directions: from water

surface and from land. Monthly wind roses of March 2017 and April 2017 indicated dominate wind blowing from the southeast (120° to 150°), with mean wind speeds of 5.14 m/s and 5.67 m/s. Monthly wind roses of February 2018, March 2018, and April 2018 indicated dominate wind blowing from the south (160° to 190°), with mean wind speeds of 4.13 m/s, 4.63 m/s, and 4.85 m/s.

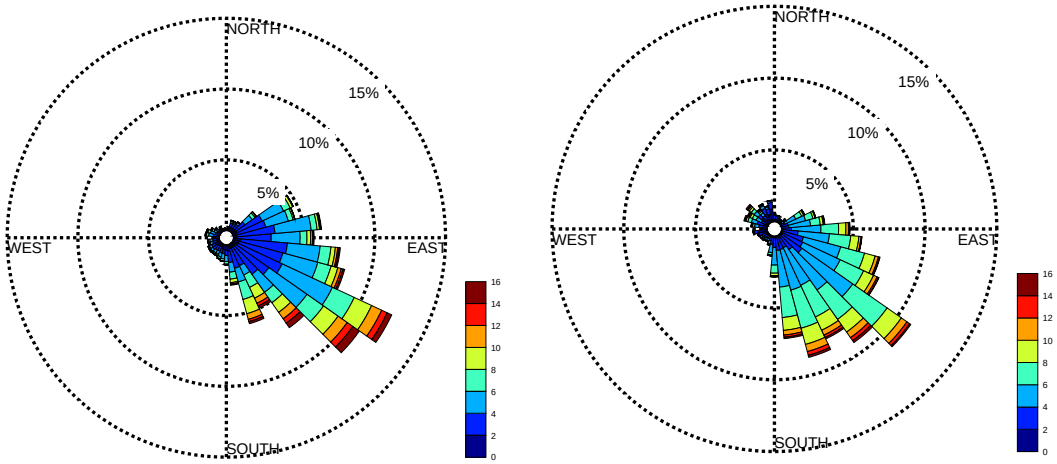

(a) March 2017 (b) April 2017

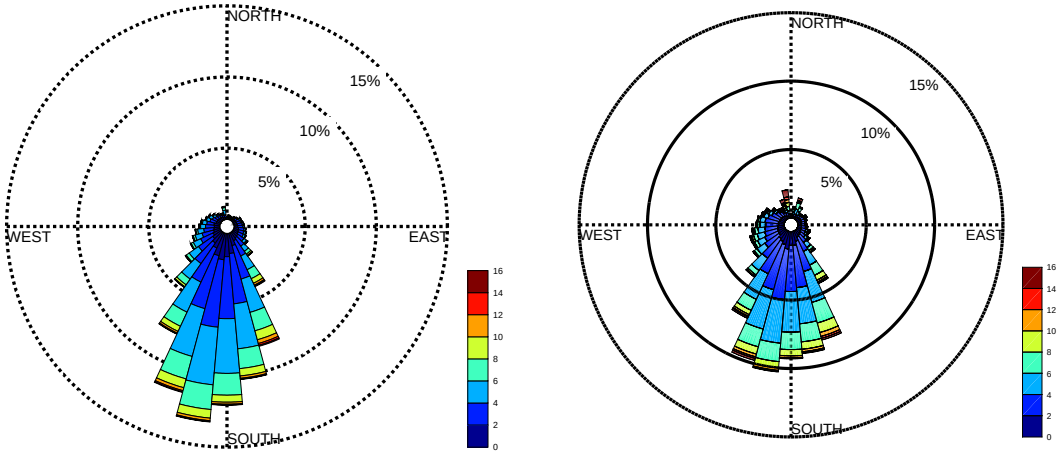

(c) February 2018 (d) March 2018

Figure A.4: Monthly wind roses of raw data as measured at two locations

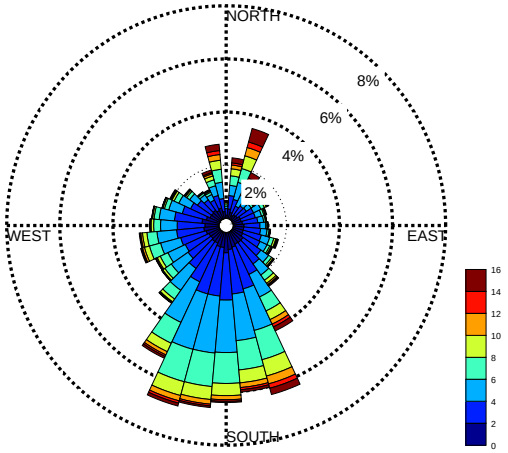

(e) April 2018

Figure A.4 continued.

A.3 Statistical Analysis

The raw data from the field measurement campaigns of each year are processed using the numerical calibration method introduced previously. The post-processed data are then reorganized into sequences with 600 data points (10 min) each. Each sequence is checked by reverse arrangement test to identify stationarity. The z-value distribution of wind speed segments of the second campaign are shown in Figure A.5.

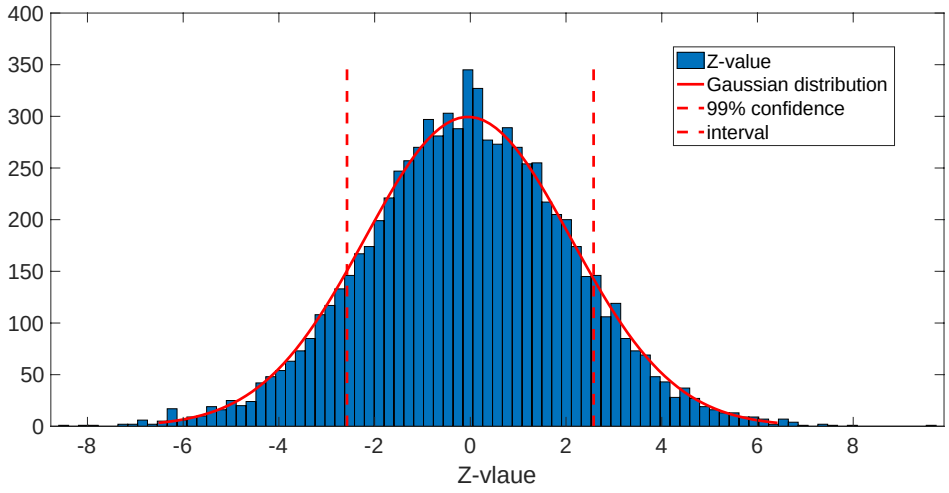

Figure A.5: Histogram of z-values based on data from campaign 2

Considering the experiment location of field measurement campaign 1, the highest peak of the wind direction histogram at the southeast (145°) and the opposite lower peak at the northwest (340°) were chosen to identify the statistical characteristics of sea breeze and land breeze. Wind speed data located within the range of these peaks were counted, as shown in Figure A.6.

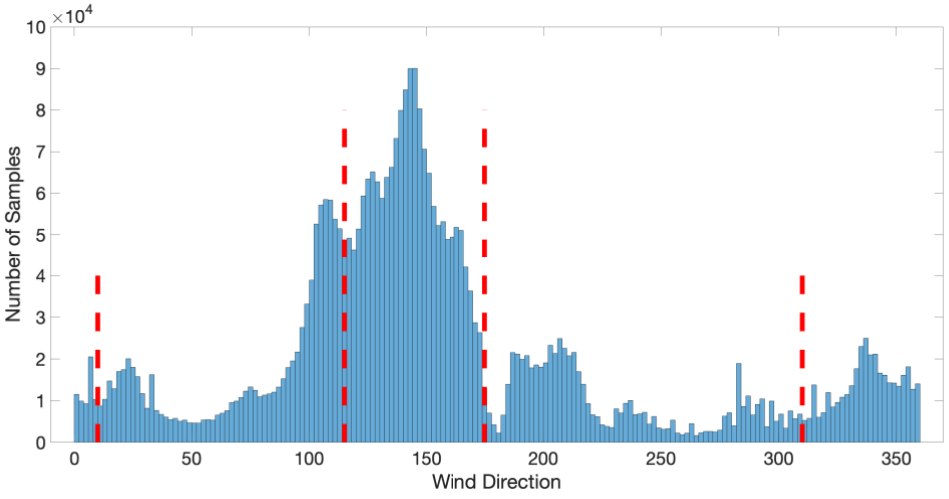

Figure A.6: Histogram of wind direction data from campaign 1

Field measurement campaign 2 was carried on the Galveston campus of Texas A&M University, which is on the north side of Galveston Island. The highest peak of wind direction histogram at the south (170°) and the opposite two smaller peaks at the north (0°) were identified as Sea breeze (overland) and Bay breeze (Figure A.7). The Sea breeze (overland) is the reformed Sea breeze which originally blow from the Gulf of Mexico, but interrupted by the ground structures of Galveston Island. The Bay breeze is the transformed Land breeze which become smooth passing though the Trinity Bay and Galveston Bay.

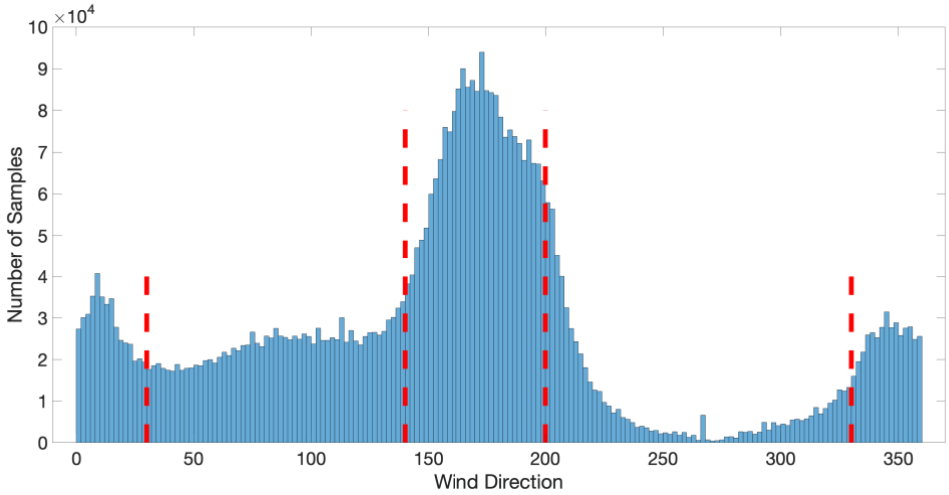

Figure A.7: Histogram of wind direction data from campaign 2

The standard deviation of campaign 1 and 2 are represented in Figure A.8. Figures A.8 (a) show the wind speed standard deviation of Land breeze and Sea breeze. Figures A.8 (b) show the wind speed standard deviation of Sea breeze (overland) and Bay breeze.

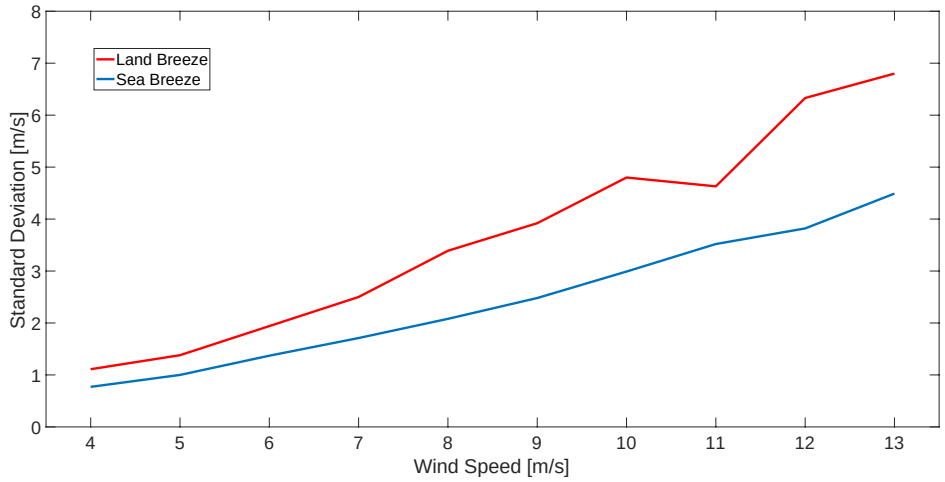

(a) Campaign 1

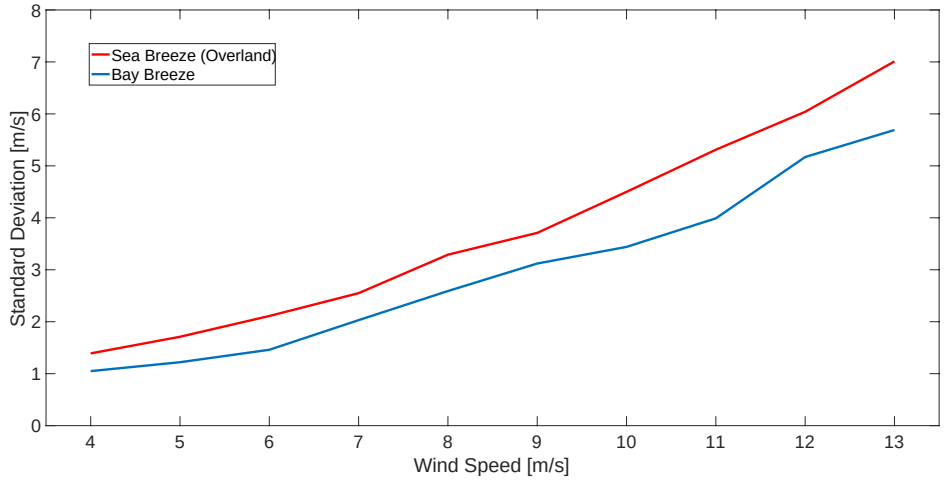

(b) Campaign 2

Figure A.8: Standard deviation of field measurement campaigns

The skewness of campaign 1 and 2 are represented in Figure A.9. Figures A.9 (a) show the wind speed skewness of Land breeze and Sea breeze. Figures A.9 (b) show the wind speed skewness of Sea breeze (overland) and Bay breeze.

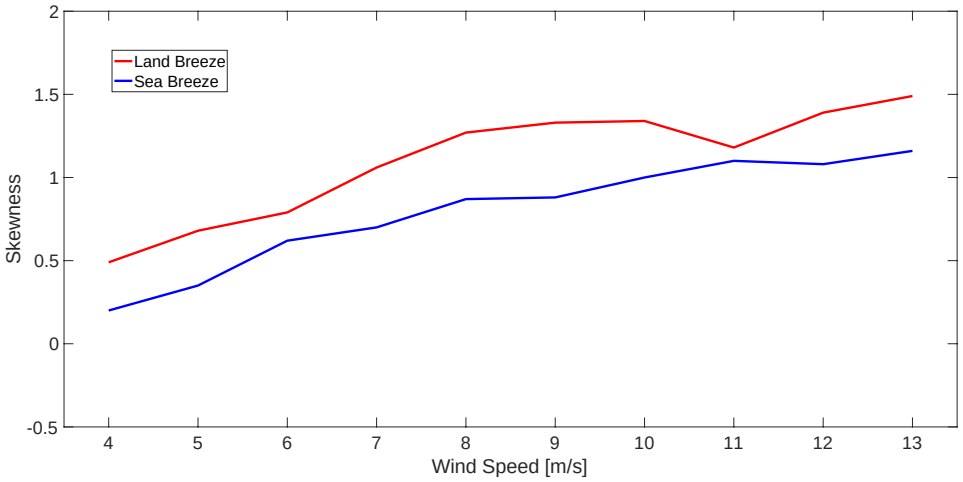

(a) Campaign 1

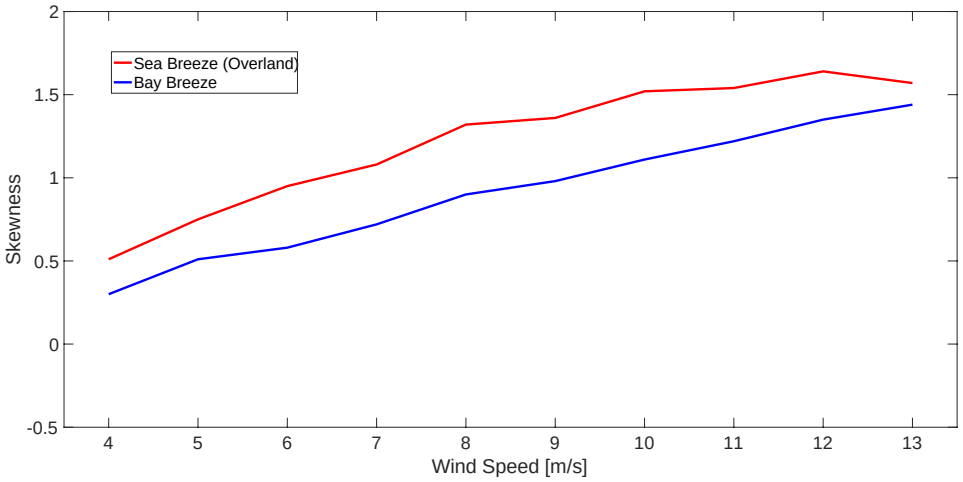

(b) Campaign 2

Figure A.9: Skewness of field measurement campaigns

The kurtosis of campaign 1 and 2 are represented in Figure A.10. Figures A.10 (a) show the wind speed kurtosis of Land breeze and Sea breeze. Figures A.10 (b) show the wind speed kurtosis of Sea breeze (overland) and Bay breeze.

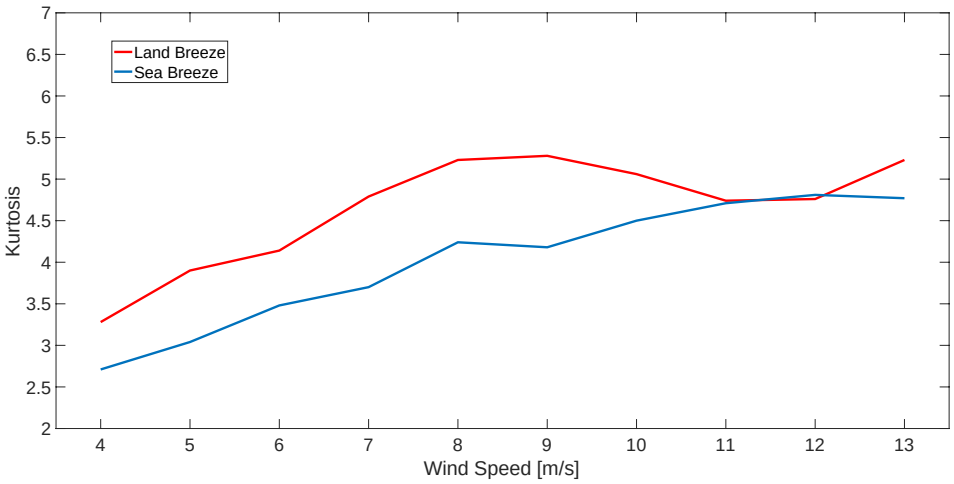

(a) Campaign 1

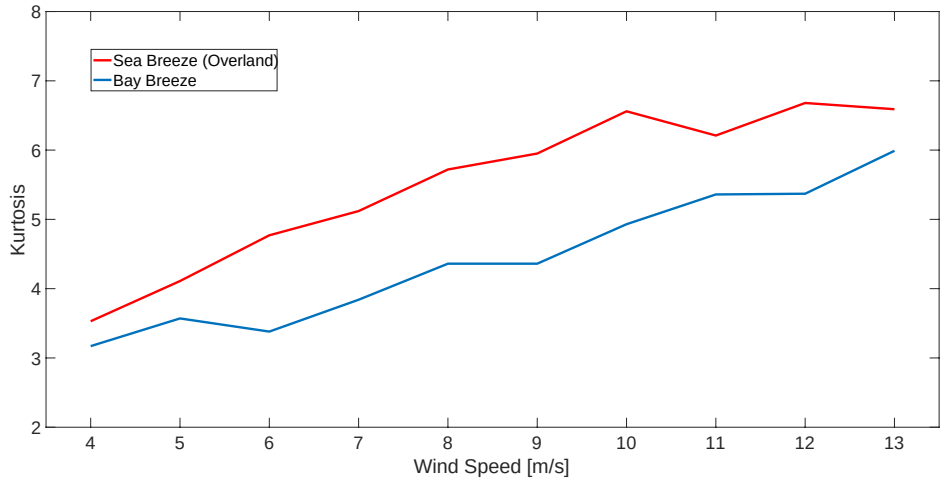

(b) Campaign 2

Figure A.10: Kurtosis of field measurement campaigns

Figures A.8 (a) indicate that the Land breeze is more irregular than Sea breeze because its standard deviation results are higher than sea breeze through all the wind speed bars. This phenomenon can be found at Figure A.3 according to the different slopes of standard deviation verse mean wind

speed. Figures A.9 (a) and A.10(a) shows that the skewness and kurtosis of Land breeze are also higher than Sea breeze.

Figures A.8 (b) indicate that the Sea breeze (overland) is more irregular than Bay breeze because its standard deviation results are higher than sea breeze through all the wind speed bars. Figures A.9 (b) and A.10 (b) shows that the skewness and kurtosis of Sea breeze (overland) are also higher than Bay breeze.

Statistical results of sea breeze and land breeze of campaign 1 are represented in Table A.1 and A.2.

Wind speed	Standard deviation	Skewness	Kurtosis
4	0.77	0.20	2.71
5	1.00	0.35	3.04
6	1.37	0.62	3.48
7	1.71	0.70	3.70
8	2.08	0.87	4.24
9	2.48	0.88	4.18
10	2.99	1.00	4.50
11	3.52	1.10	4.71
12	3.82	1.08	4.81
13	4.49	1.16	4.77

Table A.1: Statistical parameters of sea breeze of campaign 1 (145°± 30°)

Wind speed	Standard deviation	Skewness	Kurtosis
4	1.11	0.49	3.28
5	1.38	0.68	3.90
6	1.94	0.79	4.14
7	2.50	1.06	4.79
8	3.39	1.27	5.23
9	3.92	1.33	5.28
10	4.80	1.34	5.06
11	4.63	1.18	4.74
12	6.33	1.39	4.76
13	6.80	1.49	5.23

Table A.2: Statistical parameters of land breeze of campaign 1 (340°± 30°)

Statistical results of Bay breeze and Sea breeze (overland) of campaign 2 are represented in Table A.3 and A.4.

Wind speed	Standard deviation	Skewness	Kurtosis
4	1.05	0.30	3.17
5	1.22	0.51	3.57
6	1.46	0.58	3.38
7	2.03	0.72	3.84
8	2.59	0.90	4.36
9	3.12	0.98	4.36
10	3.44	1.11	4.93
11	3.99	1.22	5.36
12	5.17	1.35	5.37
13	5.69	1.44	5.99

Table A.3: Statistical parameters of bay breeze of campaign 1 (0°± 30°)

Wind speed	Standard deviation	Skewness	Kurtosis
4	1.39	0.51	3.53
5	1.71	0.75	4.11
6	2.11	0.95	4.77
7	2.55	1.08	5.12
8	3.29	1.32	5.72
9	3.71	1.36	5.95
10	4.50	1.52	6.56
11	5.31	1.54	6.21
12	6.04	1.64	6.68
13	7.01	1.57	6.59

Table A.4: Statistical parameters of sea breeze (overland) of campaign 1 (170°± 30°)

A.4 Summary

Two field measurement campaigns include many components of near-shore wind process, in which Land breeze and Sea breeze are the two major components. These two components can be identified according to the distribution of wind directions. The analysis based on first campaign indicates that Land breeze is more irregular comparing with Sea breeze (higher standard deviation, skewness, and kurtosis, as shown in Figure A.7), as we expected. The analysis based on second campaign indicates that Sea breeze (overland) is more irregular comparing with Bay breeze (Figure A.9). This result shows the influence of ground structures to wind process. The winds approaching the measurement site pass over the urban area of Galveston Island, which has nearly flat topography and is predominantly residential. The typical building heights of this area is around 5 meters, which is not original thought to be relevant to wind process above 10 m high.